Linköping Studies in Science and Technology
Thesis No. 936

Constitutive equations for concrete materials subjected to high rate of loading

Mattias Unosson

INSTITUTE OF TECHNOLOGY
LINKÖPINGS UNIVERSITET

LIU-TEK-LIC-2002:09
Division of Solid Mechanics
Department of Mechanical Engineering
Linköpings universitet
SE-581 83 Linköping, Sweden

Linköping 2002

ISBN 91-7373-301-6
ISSN 0280-7971
Printed in Sweden by UniTryck, Linköping 2002

Abstract

Continuum mechanics is used to model the mechanical behaviour of concrete structures subjected to high rates of loading in defence applications. Large deformation theory is used and an isotropic elastic-plastic constitutive equation with isotropic hardening, damage and strain rate dependent loading surface. The hydrostatic pressure is governed by an equation of state. Numerical analysis is performed using the finite element method and the central difference method for the time integration.

Projectile penetration is studied and it is concluded that it is not suitable to use material description of the motion of both the target and the projectile together with an erosion criterion. Instead, the material description should be used only for the projectile and the spatial description for the target. In this way the need for an erosion criterion is eliminated. Also, in the constitutive model used it is necessary to introduce a scaling of the softening phase in relation to the finite element size, in order to avoid strain localization.

Drop weight testing of reinforced concrete beams are analysed, where a regularisation is introduced that renders mesh objectivity regarding fracture energy release. The resulting model can accurately reproduce results from material testing but the regularisation is not sufficient to avoid strain localization when applied to an impact loaded structure. It is finally proposed that a non-local measure of deformation could be a solution to attain convergence.

The third study presents the behaviour of a concrete constitutive model in a splitting test and a simplified non-local theory applied in a tensile test. The splitting test model exhibits mesh dependency due to a singularity. In the tensile test the non-local theory is shown to give a convergent solution. The report is concluded with a discussion on how to better model concrete materials.

Acknowledgement

Gratitude is expressed to the financing organisations the Swedish Defence Research Agency (FOI), the Swedish Armed Forces (FM) and the Fortification Corps Research Fund.

The supervisor Prof. Larsgunnar Nilsson, the assistant supervisor Dr. Lars Olovsson, the project manager Mr. Håkan Hansson, M.Sc. and Dr. Eric Buzaud at the Centre d'Etudes de Gramat (CEG), France, have provided the scientific support necessary to this study.

Also, thanks to Karagozian & Case Structural Engineers (K&C) in Glendale, California for giving the author access to the material routine source code.

Finally I thank my family, Emma and Gustav, for putting work related problems into a wider perspective.

Mattias Unosson

Grindsjön Research Centre

January 2002

Thesis

This thesis for the licentiate degree in engineering at the Division of Solid Mechanics, Linköping University, consists of an introductory part and the following publications.

Unosson, M. (2000). "Numerical simulations of penetration and perforation of high performance concrete with 75mm steel projectile." *FOA-R--00-01634-311--SE*, Defence Research Establishment (FOA), Tumba.

Unosson, M. "Numerical simulations of the response of reinforced concrete beams subjected to heavy drop tests." *4th International Symposium on Impact Engineering (ISIE/4)*, Kumamoto, Japan, 613-618.

Unosson, M., and Olovsson, L. (2002). "Finite element analysis of the splitting test." *FOI-R--0262--SE*, Swedish Defence Research Agency (FOI), Tumba.

Contents

1 Introduction

The use of conventional weapons against fortifications gives rise to fast and large loadings, cf. [1]. In order to assess or optimize the protection level of a structure there are two possible methods; tests and mathematical modelling. Each one of them has its advantages and disadvantages but if used together they can render a powerful tool. The Swedish defence research agency, FOI, has been involved in experimental work for decades and there exist a great knowledge in this field. Different types of mathematical models have been used but it is only since 1994 that continuum mechanics together with numerical analysis have been employed more regularly. Today there exist several numerical tools with the techniques needed to solve the problems at hand. The part still not mastered in a satisfying manner is the constitutive modelling at high rates of loading. This work has been focused on the mechanical constitutive modelling of concrete material at high loading rates, in particular impact loading.

Research in the field of mechanical constitutive equations for concrete subjected to high loading rates started with the experimental investigation presented in Abrams [2]. Since then many studies have been devoted to this area. Most of the found knowledge on three-dimensional stressing of concrete is compiled in the European construction code, cf. [3]. This code is however only valid for constant strain rates in the range from 0 to $10^2 s^{-1}$ in compression and $3 \cdot 10^2 s^{-1}$ in tension. In penetration problems strain rate values of order $10^4 s^{-1}$ occur. Important contributors to the content in this code are Kupfer [4], William and Warnke [5] and Ottosen [6] on the shape of the loading surface, Hillerborg [7] on the softening behaviour and Reinhardt [8] on the effects of loading rates. Fundamental work on the constitutive modelling of concrete subjected to high rate of loading can be found in Nilsson [9] and Nilsson and Oldenburg [10]. A comprehensive textbook on the modelling of concrete is Chen [11].

The mechanical behaviour of concrete materials is complex. The inelastic behaviour is not related to the motion of dislocations as for metallic materials. Instead, the fracture, buckling and crushing of the cement paste and aggregate microstructure are the main mechanism of inelasticity. In a uniaxial deformation the response is approximately linearly elastic in a regime, during which micro cracks are developed. As the deformation increases the amount of cracks increases and they propagate through the material. In extensional deformation the crack planes are orthogonal to the load direction and in compression they are parallel to the load direction. During these two phases the material exhibits stable cracking or hardening. A peak stress is reached at a point where one goes into unstable cracking or softening. If hydrostatic pressure is present the material shows a residual strength. Concrete also displays dilation, i.e. volume change, in the inelastic range. For a triaxial test the development of cracks is restrained and the equation of state displays tree different phases: elastic, compaction and solidification. During the compaction phase the water and air filled pores in the material collapses and in the final solidification phase the material is approximately homogenous and the volumetric response is once again linearly elastic. Also, the strain rate influences the material response. Two mechanisms have been identified to explain this. In the lower range ($<1\text{-}10\ s^{-1}$) it is the water filled pores that increase the strength through viscous effects. In the higher range the development of micro cracks is restrained due to inertia effects, i.e. the cracks do not have time to develop. Practical limitations make it difficult to model these two mechanisms explicitly and they are hence considered as discrete phenomena. Incorporation of these two discrete phenomena must then be done in the mathematical model through the constitutive equation.

2 Continuum mechanics

In physics there are two viewpoints in modelling the nature of matter, discrete and field theories. In field theories, or phenomenological theories, continuous fields represent matter, motion energy etc. Continuum mechanics is defined as the mechanics of deformable media without consideration of the internal material structure, c.f. Truesdell and Noll [12]. Continuum mechanics can be further subdivided into fluid mechanics and solid mechanics.

2.1 Kinematics

Kinematics is the study of motion and deformation of a body within a mathematical framework.

2.1.1 Motion

The motion of a body is described by a smooth mapping of the material, or reference, configuration onto the spatial, or current, configuration.

$$\mathbf{x} = \mathbf{x}(\mathbf{X}, t) \tag{1}$$

A general motion consists of translation, rotation and deformation. The material particles X constituting the body are here identified with their position vector $\mathbf{X}$ in the material configuration schematically shown in Figure 1.

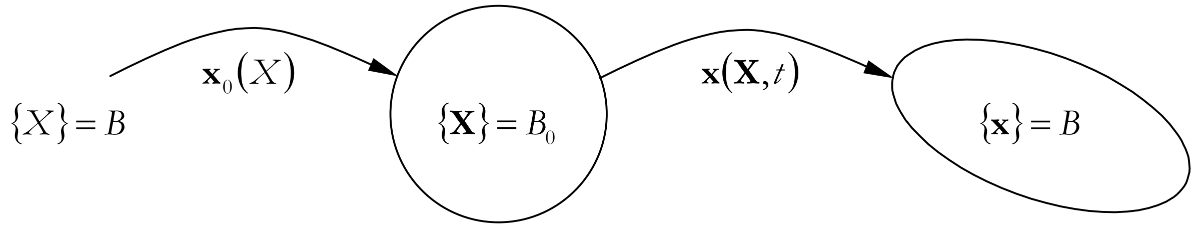

*Figure 1 The smooth mapping **x(X**,t) of the material (or reference) configuration B_0 onto the spatial (or current) configuration B.*

The displacement of a material point is given by

$$\mathbf{u}(\mathbf{X},t) = \mathbf{x}(\mathbf{X},t) - \mathbf{X} \tag{2}$$

and the velocity and acceleration of a material point respectively by

$$\mathbf{v}(\mathbf{X},t) = \frac{\partial}{\partial t}\mathbf{x}(\mathbf{X},t) = \frac{\partial}{\partial t}\mathbf{u}(\mathbf{X},t) \tag{3}$$

$$\mathbf{a}(\mathbf{X},t) = \frac{\partial}{\partial t}\mathbf{v}(\mathbf{X},t) = \frac{\partial^2}{\partial t^2}\mathbf{u}(\mathbf{X},t) \tag{4}$$

The material time derivative for spatial quantities is

$$\frac{\mathrm{D}}{\mathrm{D}t}\cdot = \frac{\partial}{\partial t}\cdot + \mathbf{v}(\mathbf{X},t)\nabla\cdot \tag{5}$$

where the last term on the right hand side is called the convective or transport term.

2.1.2 Deformation

The deformation of a body is characterized by the deformation gradient defined as

$$\mathbf{F} = \nabla_{\mathbf{X}}\mathbf{x}(\mathbf{X},t) \tag{6}$$

where$\nabla_{\mathbf{X}}$ is the gradient with respect to the material configuration

$$\nabla_{\mathbf{X}}\cdot = \frac{\partial}{\partial \mathbf{X}}\cdot \tag{7}$$

When the motion of a body gets larger, i.e. when the deformation gradient differs much from the identity tensor, we cannot use the linear measure of strain defined as

$$\boldsymbol{\varepsilon} = \frac{1}{2}\left[\nabla_{\mathbf{X}}\mathbf{u} + (\nabla_{\mathbf{X}}\mathbf{u})^{\mathrm{T}}\right] \tag{8}$$

The inadequacy of this strain is that it is non-zero for an arbitrary rigid body rotation. The rate of deformation tensor **D** is a spatial tensor that measures the rates of change in length of a spatial line segment and of their relative orientations. **D** is defined as

$$\mathbf{D} = \frac{1}{2}\left(\mathbf{L} + \mathbf{L}^{\mathrm{T}}\right) \tag{9}$$

where

$$\mathbf{L} = \frac{\mathrm{D}\mathbf{F}}{\mathrm{D}t}\mathbf{F}^{-1} = (\nabla_{\mathbf{X}}\mathbf{v})^{\mathrm{T}} \tag{10}$$

The rate of deformation vanishes for any rigid body motion but it has another drawback, it is path dependent. If it is integrated in a closed deformation cycle it does not necessarily vanish when returning to the initial configuration violating the field equation for energy balance, see Section 2.2.1. However, if the elastic strain is small compared to the total strain and the dissipation is small, the error in elastic strain energy is negligible, cf. Belytschko et al. [13]. Also, for the applications at hand the loadings are mainly monotonic. The rate of deformation is the most commonly used measure of deformation in finite element codes, and it is also the basis for the constitutive model used in this study, see Section 2.2.2. The rate of deformation tensor is integrated in time to give the strain

$$\mathbf{E} = \int_0^t \mathbf{D}\,dt \tag{11}$$

For uniaxial deformation this strain is equal to the logarithmic strain

$$E_{xx} = \int_0^t D_{xx}\,dt = \log_e\left(\frac{L}{L_0}\right) \tag{12}$$

where L and L_0 are the reference and current length, respectively. This holds true for the multiaxial case only if the principal axes of deformation are fixed, cf. Belytschko et al. [13].

2.2 Dynamics

Dynamics is the study of the mathematical relations between loading of a body and the resulting deformations. The coupled system of partial differential equations to be solved is referred to as a boundary-initial value problem.

2.2.1 Field equations

The field equations of solid mechanics are here given in their local spatial form.

• Mass

$$\frac{\mathrm{D}}{\mathrm{D}t}\varrho + \varrho \nabla \cdot \mathbf{v} = 0 \tag{13}$$

where ϱ is the density.

• Linear momentum

$$\nabla \cdot \boldsymbol{\sigma} + \varrho \mathbf{b} - \varrho \mathbf{a} = \mathbf{0} \tag{14}$$

where $\boldsymbol{\sigma}$ is the true, or Cauchy, stress tensor and $\mathbf{b}$ is the volume force per unit mass.

• Angular momentum

$$\boldsymbol{\sigma}^{\mathrm{T}} = \boldsymbol{\sigma} \tag{15}$$

• Energy

$$\varrho \frac{\mathrm{D}}{\mathrm{D}t} e = \boldsymbol{\sigma} : \mathbf{D} \tag{16}$$

where e is the specific internal energy per unit mass.

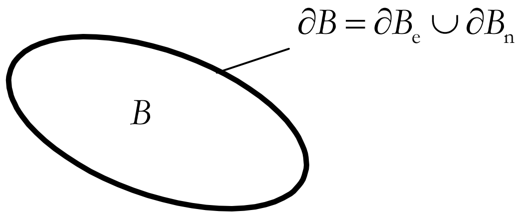

Figure 2 A deformable body B with boundary ∂B.

To arrive at a well-posed problem, initial- and boundary conditions have to be stated.

$$\left.\begin{array}{ll} \mathbf{v}(\mathbf{X},t) = \mathbf{v}_{\mathrm{e}}(\mathbf{X}) & \mathbf{X} \in \partial B_{\mathrm{e}} \\ \boldsymbol{\sigma}(\mathbf{X},t)\mathbf{n} = \mathbf{t}_{\mathrm{n}}(\mathbf{X}) & \mathbf{X} \in \partial B_{\mathrm{n}} \end{array}\right\} \quad \text{Boundary conditions} \tag{17}$$

$$\left.\begin{aligned}\varrho(\mathbf{X},0)&=\varrho_0(\mathbf{X})\\ \mathbf{u}(\mathbf{X},0)&=\mathbf{u}_0(\mathbf{X})\\ \mathbf{v}(\mathbf{X},0)&=\mathbf{v}_0(\mathbf{X})\\ e(\mathbf{X},0)&=e_0(\mathbf{X})\end{aligned}\right\}\mathbf{X}\in B \quad \text{Initial conditions} \tag{18}$$

The field equations do not allow for singular surfaces or jumps in a quantity, such as fracture and chock waves. However, chock waves are handled in numerical continuum mechanics using an artificial bulk viscosity, cf. Neumann and Richtmyer [14].

2.2.2 Constitutive equation

The rate of deformation tensor can be split additively into an elastic and an inelastic part as

$$\mathbf{D}=\mathbf{D}^{\mathrm{e}}+\mathbf{D}^{\mathrm{ie}} \tag{19}$$

The model used in this study is based on hypoelasticity, cf. Truesdell and Noll [12], where the stress rate is a linear function of the rate of deformation. The material time derivative of the true stress tensor is a non-objective tensor, i.e. it is not invariant under an arbitrary change of frame of reference, cf. Ogden [15], and cannot be used directly as a measure of the stress rate. This problem is circumvented by the use of an objective rate. In this study the Jaumann rate, $\overset{\circ}{\boldsymbol{\sigma}}$, cf. Lubliner [16], has been used.

$$\frac{\mathrm{D}}{\mathrm{D}t}\boldsymbol{\sigma}=\overset{\circ}{\boldsymbol{\sigma}}+\mathbf{W}\boldsymbol{\sigma}+\boldsymbol{\sigma}\mathbf{W}^{\mathrm{T}}=\mathbf{C}:\mathbf{D}^{\mathrm{e}}+\mathbf{W}\boldsymbol{\sigma}+\boldsymbol{\sigma}\mathbf{W}^{\mathrm{T}} \tag{20}$$

where

$$\mathbf{W}=\frac{1}{2}\left(\mathbf{L}-\mathbf{L}^{\mathrm{T}}\right) \tag{21}$$

and **C** is the tensor of elasticity. The Jaumann rate has been shown to provide incorrect results for simple elastic shearing, cf. Belytschko et al. [13]. In Figure 3 to Figure 5 the resulting stresses for the isotropic linear elastic case are shown from three different objective stress rates with equivalent elastic material parameters. For the material and applications in this study the elastic deformations are negligible compared to the total deformation. Thus the Jaumann rate can be used.

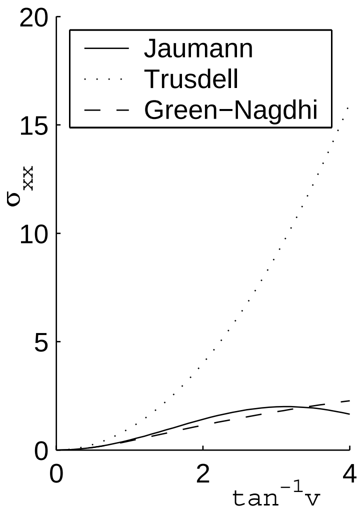

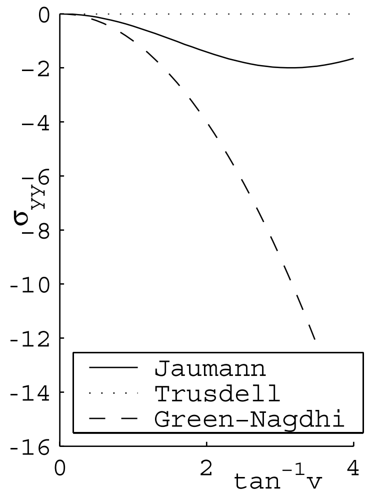

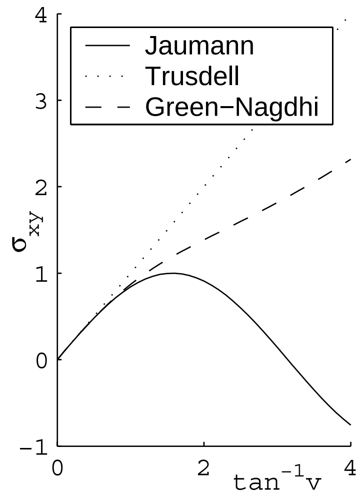

Figure 3 Normal stress parallel to the shear direction.

Figure 4 Normal stress orthogonal to the shear direction.

Figure 5 Shear stress.

The first mathematical models of the mechanical behaviour of concrete were based on isotropic, linear hyperelasticity combined with a failure criterion in tension, cf. Chen [11]. These models were restricted to problems where brittle failure in tension is prevailing and they soon showed to be inadequate for many problems.

Mechanical testing of concrete revealed that the strength of concrete depended on all three invariants of the stress tensor. To model this behaviour attention was turned towards the theory of plasticity, cf. Hill [17], from which the idea of an elastic domain in stress space bounded by a failure surface was adopted. One or combinations of new and existing functions, for example von Mises, Rankine, Mohr-Coulomb and Drucker-Prager, were used to describe the failure surface. Two of the most widely used functions are due to Ottosen [6] and William and Warnke [5], used for example in the CEB-FIP model code [3].

Refinement of the models, still within the ideas of plasticity theory, included the addition of an initial elastic domain bounded by a yield surface and a corresponding hardening rule. All of the functions mentioned so far are open surfaces in stress space, but from tests it was observed that the elastic domain should be closed. This has been modelled using either a separate function for the volumetric behaviour or closed functions. Examples of closed functions are the critical state function, the two surface cap, the generalized ellipsoidal, cf. Nilsson [9], and the Hoffman failure criterion used for example in Winnicki et al. [18].

Further testing of concrete, now under displacement control, showed the existence of a descending branch after the peak stress, a phenomenon commonly called softening. To model this the brittle failure models were abandoned and softening rules were introduced, cf. Hillerborg [19], still within the framework of plasticity theory.

The introduction of inelastic deformations in the constitutive relations made it necessary to separate the elastic and the inelastic strains. For small, or infinite, deformations there exists an intersubjective theory on the mathematical treatment, but not for large, or finite, deformations, cf. Ristinmaa and Ottosen [20]. But, the rate of deformation can always be additively partitioned and this is the basis for hypoelasticity that has been more used than hyperelasticity. The incremental deformation theory of plasticity has been used more extensively than the total deformation theory, cf. Nilsson [9].

Strength enhancement due to dynamic loading has been included in the models mainly through enhancement of the failure surface based on strain rate. Strictly, this is a contradiction since the theory of plasticity is the theory for time independent inelastic deformations. Viscoplasticity, the theory for time dependent inelastic deformations, cf. Perzyna [21], was used in Nilsson [9] but has since then not been used extensively. One of the more recent works is Winnicki et al. [18].

Among the state of the art models available in commercial finite element codes for different situations of dynamic loading of concrete structures are the RHT model from Riedel [22], the Winfrith model [23], the cap model by Schwer and Murray [24] and the JHC model, cf. Holmquist et al. [25].

The K&C concrete model, cf. Malvar et al. [26], is an enhanced version of the Pseudo tensor model available in LS-DYNA [27] and developed at the Lawrence Livermore National Laboratories, USA. It was developed and modified mainly to analyse concrete structures subjected to blast loading. It is a linear isotropic hypoelastic-plastic model with strain rate scaled elastic domain, a non-associated flow rule and non-linear anisotropic strain hardening and softening representing stable and unstable cracking. The deviatoric and isotropic parts of the response are uncoupled and the isotropic behaviour is governed by a compaction curve or equation of state.

Elastic domain

The deviatoric elastic domain is defined as

$$E_{\mathbf{T}} = \left\{ \left(\boldsymbol{\sigma}, E^{\mathrm{p}} \right) \in S \times R_{+} \mid f\left(\boldsymbol{\sigma}, E^{\mathrm{p}} \right) < 0 \right\} \tag{22}$$

where S is the six dimensional stress space with linear, symmetric and positive definite second order tensors. R_+ is the space of positive real values and E^{p} is an internal history variable representing plastic straining. The isotropic criterion f is stated as

$$f\left(\boldsymbol{\sigma}, E^{\mathrm{p}} \right) = J_2 - f_1 \tag{23}$$

where

$$J_2 = J_2(\boldsymbol{\sigma}) \tag{24}$$

$$f_1 = f_1\left(p, v, E^{\mathrm{p}}\right) \tag{25}$$

and

$$p = -\frac{1}{3} I_1(\boldsymbol{\sigma}) \tag{26}$$

$$\cos(3v) = \frac{1}{27}\left(\frac{J_3(\boldsymbol{\sigma})}{J_2(\boldsymbol{\sigma})}\right)^3 \tag{27}$$

$$\left.\begin{aligned} I_1(\boldsymbol{\sigma}) &= \mathrm{tr}(\boldsymbol{\sigma}) \\ J_2(\boldsymbol{\sigma}) &= \left[\frac{3}{2}\mathrm{dev}(\boldsymbol{\sigma}) : \mathrm{dev}(\boldsymbol{\sigma})\right]^{\frac{1}{2}} \\ J_3(\boldsymbol{\sigma}) &= \left[\frac{9}{2}\mathrm{tr}\left(\boldsymbol{\sigma}^3\right)\right]^{\frac{1}{3}} \end{aligned}\right\} \tag{28}$$

$$\mathrm{dev}(\boldsymbol{\sigma}) = \boldsymbol{\sigma} - \frac{1}{3} I_1(\boldsymbol{\sigma}) \tag{29}$$

These forms on the invariants of the stress tensor are taken from Lemaitre and Chaboche [28]. The calculation of the modified effective plastic strain E^{p} is given in the section Inelastic domain. In the principal stress space this corresponds to a loading surface constructed as described in the following. The compressive and tensile meridians are defined as lines in the Rendulic stress space for which the angle v equals $\pi/3$ and 0, respectively, see Figure 6 and Figure 7. For hydrostatic pressures below one third of the compressive strength the meridians are piecewise linear functions connecting the points corresponding to triaxial extension, biaxial extension, uniaxial extension and uniaxial compression. For hydrostatic pressure exceeding one third of the compressive strength, the initial, quasi-static compressive meridians are given by the general relation

$$f_1^{\mathrm{c}} = f_1\left(p, v = \pi/3, E^{\mathrm{p}} = 0\right) = a_0 + \frac{p}{a_1 + a_2 p} \tag{30}$$

where a_n are scalar valued parameters that are chosen to fit data from material characterization tests. Three compression meridians are defined, one representing the initial elastic domain, one for the failure strength and one for the residual strength according to

$$f_{\mathrm{i}}^{\mathrm{c}} = f_1\left(p, v = \tfrac{\pi}{3}, E^{\mathrm{p}} = 0\right) = a_0^{\mathrm{i}} + \frac{p}{a_1^{\mathrm{i}} + a_2^{\mathrm{i}} p} \tag{31}$$

$$f_{\mathrm{f}}^{\mathrm{c}} = f_1\left(p, v = \tfrac{\pi}{3}, E^{\mathrm{p}} = E_{\mathrm{f}}^{\mathrm{p}}\right) = a_0^{\mathrm{f}} + \frac{p}{a_1^{\mathrm{f}} + a_2^{\mathrm{f}} p} \tag{32}$$

$$f_{\mathrm{r}}^{\mathrm{c}} = f_1\left(p, v = \tfrac{\pi}{3}, E^{\mathrm{p}} \geq E_{\mathrm{r}}^{\mathrm{p}}\right) = \frac{p}{a_1^{\mathrm{r}} + a_2^{\mathrm{r}} p} \tag{33}$$

from which the current compressive load meridian is interpolated as

$$f_1^{\mathrm{c}} = \begin{cases} f_{\mathrm{i}}^{\mathrm{c}} & , E^{\mathrm{p}} \leq 0 \\ d\left(f_{\mathrm{f}}^{\mathrm{c}} - f_{\mathrm{i}}^{\mathrm{c}}\right) + f_{\mathrm{i}}^{\mathrm{c}} & , 0 \leq E^{\mathrm{p}} \leq E_{\mathrm{f}}^{\mathrm{p}} \\ d\left(f_{\mathrm{f}}^{\mathrm{c}} - f_{\mathrm{r}}^{\mathrm{c}}\right) + f_{\mathrm{r}}^{\mathrm{c}} & , E_{\mathrm{f}}^{\mathrm{p}} \leq E^{\mathrm{p}} \leq E_{\mathrm{r}}^{\mathrm{p}} \\ f_{\mathrm{r}}^{\mathrm{c}} & , E_{\mathrm{r}}^{\mathrm{p}} \leq E^{\mathrm{p}} \end{cases} \tag{34}$$

where

$$d = d\left(E^{\mathrm{p}}\right) \mid d \in \left]0,1\right[\tag{35}$$

The minimum, i.e. tensile, pressure is interpolated as

$$p_{\min} = \begin{cases} -f_{\mathrm{t}} & , 0 \leq E^{\mathrm{p}} \leq E_{\mathrm{f}}^{\mathrm{p}} \\ -f_{\mathrm{t}} d & , E_{\mathrm{f}}^{\mathrm{p}} \leq E^{\mathrm{p}} \end{cases} \tag{36}$$

where f_t is the failure strength in tension. The tensile meridian is given as a fraction $k(p)$ of the compressive meridian according to

$$k(p) = \frac{r_{\mathrm{t}}(p)}{r_{\mathrm{c}}(p)} \tag{37}$$

and the values on $k(p)$ are set according to Table 1, where f_c and f_t is the compressive and tensile failure strength, respectively.

Table 1 Values on the piecewise linear function k(p)

p	≤ 0	$\frac{1}{3} f_c$	$\frac{2 \cdot 1.15}{3} f_c$	$3 f_c$	$\geq 8.45 f_c$
$k(p)$	$\frac{1}{2}$	$\frac{1}{2} + \frac{3 f_t}{2 f_c}$	$\dfrac{1.15 f_c}{a_0^{\mathrm{f}} + \dfrac{2 \cdot 1.15 f_c/3}{a_1^{\mathrm{f}} + 2 a_2^{\mathrm{f}} 1.15 f_c/3}}$	0.753	1

In Figure 6 and Figure 7 graphical representations are given of the meridians corresponding to a concrete material with compressive and tensile strength of 100 and 5.3 MPa, respectively.

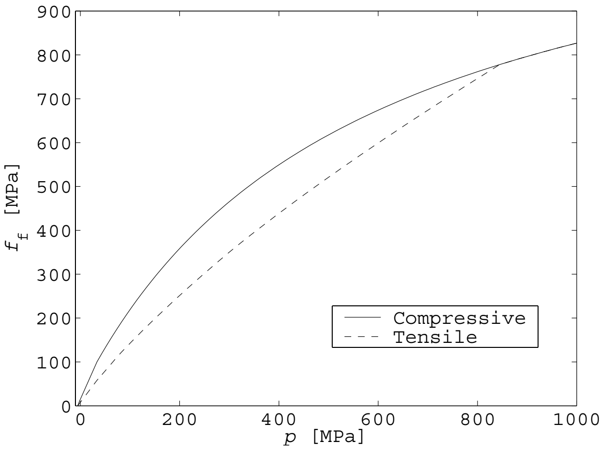

Figure 6 Compressive ($v=\pi/3$) and tensile ($v=0$) meridians.

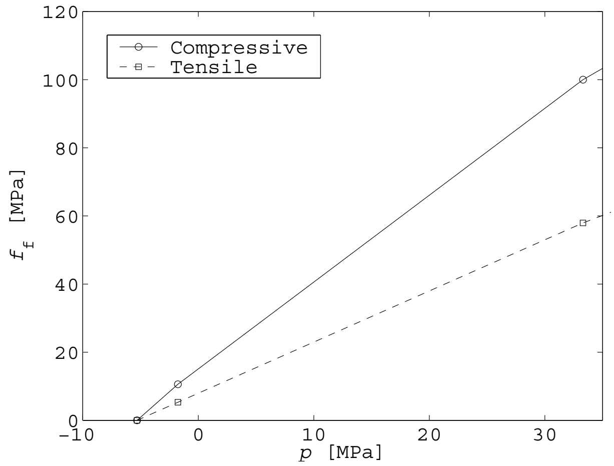

Figure 7 Compressive ($v=\pi/3$) and tensile ($v=0$) meridians in the lower pressure range.

The generalisation to a three-dimensional stress space, i.e. to include the third invariant of the deviatoric stress tensor, is done using the function proposed in William and Warnke [5] through the following expression

$$r_v(p,v) = r_{\mathrm{c}} \frac{2(1-k^2)\cos v + (2k-1)\left[4(1-k^2)\cos^2 v + 5k^2 - 4k\right]^{\frac{1}{2}}}{4(1-k^2)\cos^2 v + (1-2k)^2} \tag{38}$$

where r_v is the distance from the hydrostatic axis to an arbitrary meridian. In Figure 8 a graphical representation of the ratio r_v/r_{c} is given.

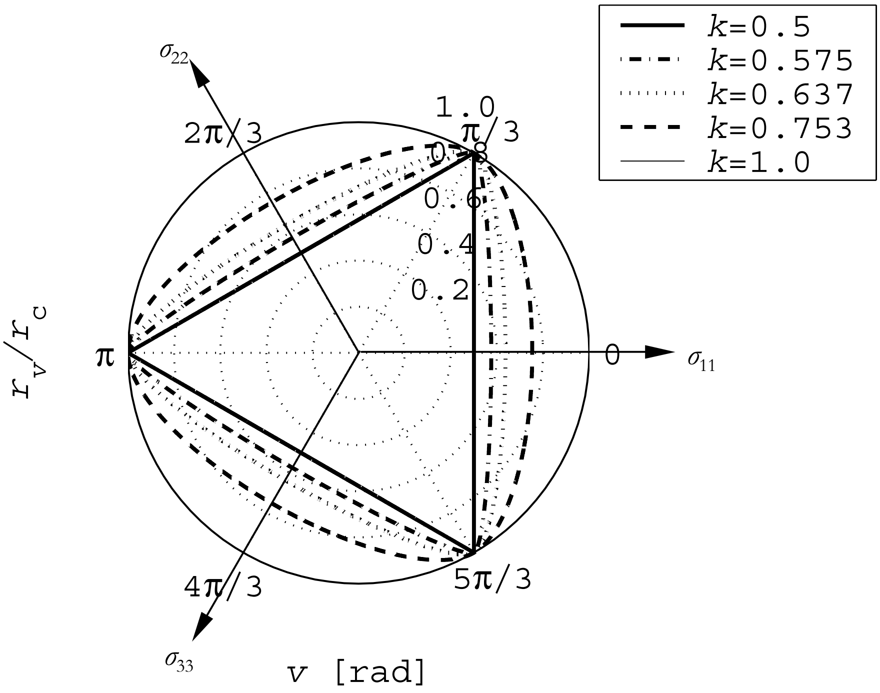

Figure 8 Ratio between the distances from the hydrostatic axis to an arbitrary and the compressive meridian, respectively.

Strength enhancement due to high rate of loading, see Section 1, is included through the factor

$$a = a(D) \tag{39}$$

where

$$D = \left(\frac{2}{3} \mathbf{D} : \mathbf{D} \right)^{\frac{1}{2}} \tag{40}$$

and carried out radially from the origin in the principal stress space. An example of such a relation is given in Figure 9.

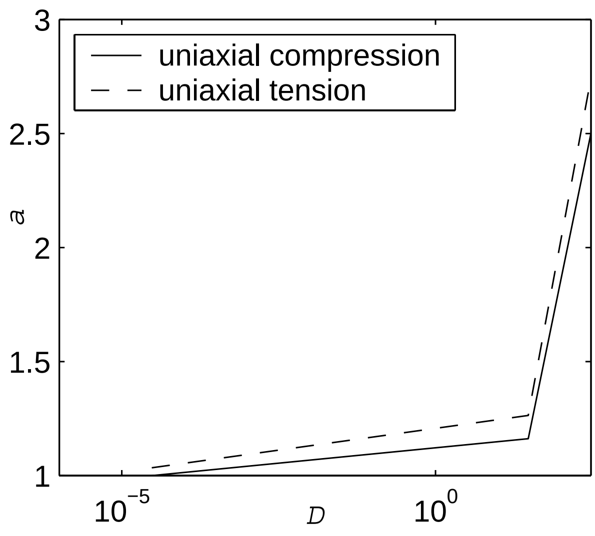

Figure 9 Strength enhancement due to high strain rates. From the CEB-FIP model code 90 [3].

The complete expression for the load function then becomes

$$f_1 = ar_v f_1^{\mathrm{c}} \tag{41}$$

Inelastic domain

In the deviatoric inelastic domain defined as

$$\partial E_{\mathbf{T}} = \left\{ \left(\boldsymbol{\sigma}, E^{\mathrm{p}} \right) \in S \times R_+ \mid f\left(\boldsymbol{\sigma}, E^{\mathrm{p}} \right) = 0 \right\} \tag{42}$$

the evolution of the inelastic deformation is governed by an non-associated flow rule with non-linear anisotropic strain hardening and softening. The derivation starts with the standard relations for plasticity theory

$$\mathbf{D}^{\mathrm{p}} = \dot{\lambda}\mathbf{r} \tag{43}$$

$$\dot{f} = 0 \tag{44}$$

and a for this model, a modified effective plastic strain measure defined as

$$\dot{E}^{\mathrm{p}} = hD^{\mathrm{p}} \tag{45}$$

where

$$D^{\mathrm{p}} = \left(\frac{2}{3} \mathbf{D}^{\mathrm{p}} : \mathbf{D}^{\mathrm{p}} \right)^{\frac{1}{2}} \tag{46}$$

$$h(p,a)=\begin{cases}\dfrac{1}{a\left(1+\dfrac{p}{af_t}\right)^{b_1}} & ,p\geq 0\\[2ex] \dfrac{1}{a\left(1+\dfrac{p}{af_t}\right)^{b_2}} & ,p<0\end{cases} \tag{47}$$

Here b_i is test data fitting parameters, f_t is the uniaxial tensile strength and a is a factor to include rate effects. An associated flow rule would have direction according to

$$\mathbf{r}=\mathbf{r}_{\mathrm{a}}=\frac{\partial f}{\partial \boldsymbol{\sigma}}=\frac{\partial J_2}{\partial \boldsymbol{\sigma}}-\frac{\partial f_1}{\partial p}\frac{\partial p}{\partial \boldsymbol{\sigma}}-\frac{\partial f_1}{\partial v}\frac{\partial v}{\partial \boldsymbol{\sigma}} \tag{48}$$

and the relation stating that that a stress point in plastic loading must remain on the loading surface is

$$\dot{f}=\dot{J}_2-\frac{\partial f_1}{\partial p}\dot{p}-\frac{\partial f_1}{\partial v}\dot{v}-\frac{\partial f_1}{\partial E^{\mathrm{p}}}\dot{E}^{\mathrm{p}}=0 \tag{49}$$

or as

$$\dot{E}^{\mathrm{p}}=\frac{\dot{J}_2-\dfrac{\partial f_1}{\partial p}\dot{p}-\dfrac{\partial f_1}{\partial v}v}{\dfrac{\partial f_1}{\partial E^{\mathrm{p}}}} \tag{50}$$

Using equations 43, 45, 46 and 50 the plastic multiplier for the associated case is evaluated as

$$\dot{m}_{\mathrm{a}}=\frac{\dot{J}_2-\dfrac{\partial f_1}{\partial p}\dot{p}-\dfrac{\partial f_1}{\partial v}\dot{v}}{h\dfrac{\partial f_1}{\partial E^{\mathrm{p}}}\left(\dfrac{2}{3}\mathbf{r}_a:\mathbf{r}_a\right)^{\frac{1}{2}}} \tag{51}$$

In our application of this model the direction of the plastic deformation is assumed to be independent of p and v, i.e. the non-associated direction

$$\mathbf{r}=\frac{\partial J_2}{\partial \boldsymbol{\sigma}}=\frac{3}{2J_2}\operatorname{dev}(\boldsymbol{\sigma}) \tag{52}$$

is used. Thus, the plastic multiplier

$$\dot{m} = \frac{\dot{J}_2 - \frac{\partial f_1}{\partial p}\dot{p} - \frac{\partial f_1}{\partial v}\dot{v}}{h\frac{\partial f_1}{\partial E^{\mathrm{p}}}\left(\frac{2}{3}\mathbf{r}:\mathbf{r}\right)^{\frac{1}{2}}} \tag{53}$$

forms the final form of the flow rule expressed as

$$\mathbf{D}^{\mathrm{p}} = \frac{3\left(\dot{J}_2 - \frac{\partial f_1}{\partial p}\dot{p} - \frac{\partial f_1}{\partial v}\dot{v}\right)}{2J_2 h\frac{\partial f_1}{\partial E^{\mathrm{p}}}}\operatorname{dev}(\boldsymbol{\sigma}) \tag{54}$$

To include damage due to isotropic tensile stressing, a volumetric part is added to the damage

$$\dot{E}^{\mathrm{p}}_{\mathrm{v}} = b_3 f_d k_d \left(D^{\mathrm{v}} - D^{\mathrm{v}}_1\right) \tag{55}$$

where

$$f_d = \begin{cases} 1 - \left|\frac{J_2}{0.1p}\right|, & 0 \le \left|\frac{J_2}{p}\right| \le 0.1 \\ 0 \quad , & \left|\frac{J_2}{p}\right| \ge 0.1 \end{cases} \tag{56}$$

Here b_3 and k_d are scalar valued parameters and D^{v} and D_1^{v} are the current volumetric strain and the volumetric strain at the load surface, respectively. An example of a function for the scalar valued internal variable $d(E^{\mathrm{p}})$ is given in Figure 10. This damage curve is optimized for one finite element size and to make it independent of the spatial discretization. Thus, in order to get the correct fracture energy release for all element sizes in a model, it has to be scaled relative the current element size using

$$s = \frac{V^{\frac{1}{3}}}{L_{\mathrm{c}}} \tag{57}$$

and

$$\dot{E}_{\mathrm{s}}^{\mathrm{p}} = \begin{cases} \dot{E}^{\mathrm{p}} + \dot{E}_{\mathrm{v}}^{\mathrm{p}} & ,0 < E^{\mathrm{p}} < E_{\mathrm{f}}^{\mathrm{p}} \\ \dot{E}^{\mathrm{p}} s + \left(\dot{E}_{\mathrm{v}}^{\mathrm{p}}\right)^{s} & ,E_{\mathrm{f}}^{\mathrm{p}} < E^{\mathrm{p}} \end{cases} \tag{58}$$

where V is the current element volume and L_{c} is a reference length.

The volumetric material behaviour is governed by an equation of state that incorporates three phases: Elastic, compaction and solidification. In the compaction phase the air filled pores collapse and in the solidification phase all pores have collapsed and the material is solidified. An example of such a relation is given in Figure 11 where V_0 and V denote the initial volume and current volume, respectively.

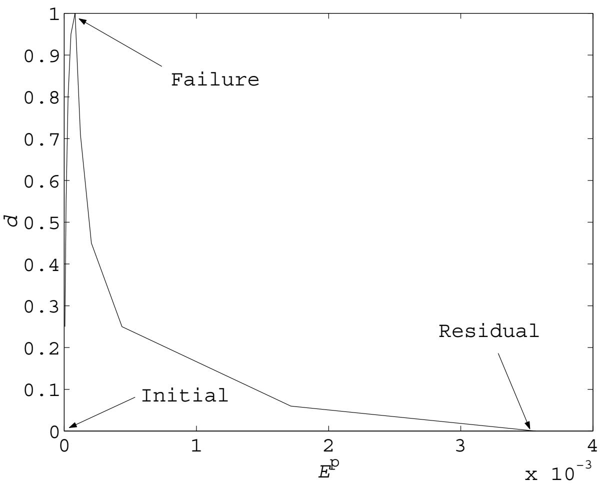

Figure 10 Example of the function d(E^p).

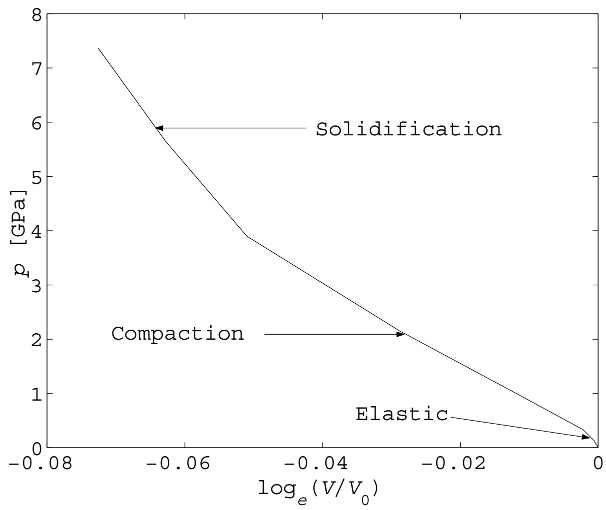

Figure 11 Equation of state for concrete material with an uniaxial compressive strength of 100 MPa.

3 Numerical analysis

An analytical solution to the field equations of continuum mechanics can be derived only in special cases. To solve the general form one must rely on numerical analysis. The idea of numerical analyses is to efficiently calculate accurate approximations to the solution. For the applications at hand the Finite Element Method (FEM) is the chosen numerical tool.

A kinematically admissible velocity field **v** is defined as

$$\left.\begin{aligned} &\mathbf{v}(\mathbf{X},t)\in S \\ &S=\{\mathbf{v}\mid\mathbf{v}\in C^0(\mathbf{X}),\mathbf{v}(\partial B_e)=\mathbf{v}_e\}\end{aligned}\right\} \tag{59}$$

The C^0-condition assures that the functions are square integrable. This gives a residual equation for the linear momentum

$$\nabla\cdot\boldsymbol{\sigma}+\varrho\mathbf{b}-\varrho\mathbf{a}=\mathbf{d} \tag{60}$$

where **d** is the residual vector. The idea here is to minimize a weighted residual over the spatial domain

$$\int_B \mathbf{d}\mathbf{w}dB=\int_B(\nabla\cdot\boldsymbol{\sigma}+\varrho\mathbf{b}-\varrho\mathbf{a})\mathbf{w}dB=0 \tag{61}$$

using a weight function **w**, or variation, defined as

$$\left.\begin{aligned} &\mathbf{w}(\mathbf{X})\in V \\ &V=\{\mathbf{w}\mid\mathbf{w}\in C^0(\mathbf{X}),\mathbf{w}(\partial B_e)=0\}\end{aligned}\right\} \tag{62}$$

If the weight functions are taken the same as the trial functions the formulation is referred to as the Bubnov-Galerkin method and if they differ, the Petrov-Galerkin method. Applying integration by parts and using the natural boundary conditions results in the variation form of the linear momentum equation

$$\int_B \boldsymbol{\sigma} : (\nabla \mathbf{w}) dB - \int_B \varrho \mathbf{b}\mathbf{w} dB - \int_{\partial B_\mathrm{n}} \mathbf{t}_\mathrm{n} \mathbf{w} dB + \int_B \varrho \mathbf{a}\mathbf{w} dB = 0 \tag{63}$$

This expression quantifies the principle of virtual power and it constitutes the basis for the Finite Element Method in solid mechanics.

3.1 Spatial discretization

The body considered is discretized into *ne* subdomains, or finite elements, B_e defined by their nodes *i*.

$$\sum_{e=1}^{ne} \left(\int_{B^e} \boldsymbol{\sigma} : (\nabla \mathbf{w}) dB - \int_{B^e} \varrho \mathbf{b}\mathbf{w} dB - \int_{\partial B_n^e} \mathbf{t}_\mathrm{n} \mathbf{w} dB + \int_B \varrho \mathbf{a}\mathbf{w} dB \right) = 0 \tag{64}$$

The motion and weight function in each finite element are approximated as

$$\mathbf{x}(\mathbf{X}, t) = \mathbf{N}^\mathrm{T}(\mathbf{X})\mathbf{x}^\mathrm{e}(t) \tag{65}$$

$$\mathbf{w}(\mathbf{X}, t) = \mathbf{N}^\mathrm{T}(\mathbf{X})\mathbf{w}^\mathrm{e}(t) \tag{66}$$

where $\mathbf{N}$ is a matrix containing the element shape functions, $\mathbf{x}^\mathrm{e}$ is the element nodal co-ordinate vector and $\mathbf{w}^\mathrm{e}$ is the element weight function. These approximations and that the principle of virtual power should hold for any $\mathbf{w}$, result in

$$\sum_{e=1}^{ne} \left(\mathbf{M}^e \mathbf{a}^e - \mathbf{f}_\mathrm{ext}^e + \mathbf{f}_\mathrm{int}^e \right) = \mathbf{0} \tag{67}$$

where

$$\mathbf{M}^e = \int_{B^e} \varrho \mathbf{N}\mathbf{N}^\mathrm{T} dB \tag{68}$$

$$\mathbf{f}_\mathrm{ext}^e = \int_B \varrho \mathbf{b}\mathbf{N}^\mathrm{T} dB + \int_{\partial B_\mathrm{n}} \mathbf{t}_\mathrm{n} \mathbf{N}^\mathrm{T} dB \tag{69}$$

$$\mathbf{f}_\mathrm{int}^e = \int_B \boldsymbol{\sigma} : \nabla \left(\mathbf{N}^\mathrm{T} \right) dB \tag{70}$$

To reduce CPU-costs and use an explicit time integration a lumped, or diagonalized, mass matrix is computed through row summation as

$$\mathbf{M}_{\mathrm{d}}^{e}=\begin{bmatrix} \int_B \varrho N_1 dB & 0 & . \; . \; . & 0 \\ 0 & \int_B \varrho N_2 dB & . \; . \; . & 0 \\ . & . & . & \\ . & . & . & 0 \\ . & . & . & \\ 0 & 0 & 0 & \int_B \varrho N_n dB \end{bmatrix}$$

An assembly procedure, where the element tensors are scattered on global tensors, is then performed which yields the semi-discrete linear momentum equation for the system

$$\mathbf{M}_{\mathrm{d}}\mathbf{a}+\mathbf{f}_{\mathrm{int}}=\mathbf{f}_{\mathrm{ext}} \tag{71}$$

To avoid volumetric locking and to further reduce the CPU-costs, the volume integration is performed using single point Gaussian quadrature. This introduces rank deficiency, manifested as hourglass modes, which has to be controlled, cf. Belytschko et al. [13]. This control is done through the addition of a stabilisation vector $\mathbf{f}_{\mathrm{stab}}$

$$\mathbf{M}_{\mathrm{d}}\mathbf{a}+\mathbf{f}_{\mathrm{int}}=\mathbf{f}_{\mathrm{ext}}+\mathbf{f}_{\mathrm{stab}} \tag{72}$$

3.2 Temporal discretization

For the time integration of the semi-discrete linear momentum equation the central difference method is used, which is an explicit step-by-step method. The integration starts with the initial conditions and the force vectors at time t_0. Nodal accelerations are calculated at the current time step t_n

$$\mathbf{a}(t_{\mathrm{n}})=\mathbf{M}_{\mathrm{d}}^{-1}\left[\mathbf{f}_{\mathrm{ext}}(t_{\mathrm{n}})-\mathbf{f}_{\mathrm{int}}(t_{\mathrm{n}})+\mathbf{f}_{\mathrm{stab}}(t_{\mathrm{n}})\right] \tag{73}$$

Then the central, or mid, velocities at time $t_{n+1/2}$ are calculated as

$$\mathbf{v}\left(t_{\mathrm{n}+\frac{1}{2}}\right)=\mathbf{v}(t_{\mathrm{n}})+\mathbf{a}(t_{\mathrm{n}})\left(t_{\mathrm{n}+\frac{1}{2}}-t_{\mathrm{n}}\right) \tag{74}$$

where

$$t_{\mathrm{n}+\frac{1}{2}}=\frac{1}{2}\left(t_{\mathrm{n}}+t_{\mathrm{n}+1}\right) \tag{75}$$

After this step the velocity boundary conditions are enforced and the displacement is updated as

$$\mathbf{u}(t_{n+1}) = \mathbf{u}(t_n) + \mathbf{v}\left(t_{n+\frac{1}{2}}\right)\Delta t \tag{76}$$

where

$$\Delta t = t_{n+1} - t_n \tag{77}$$

The external force vector is assembled from prescribed loading and contact forces. To calculate the internal force vector one needs the Cauchy stress tensor at t_{n+1}. First the stress tensor at t_n is rotated into the configuration at t_{n+1} and the hydrostatic pressure is subtracted

$$\mathrm{dev}\left[\boldsymbol{\sigma}^{\mathrm{r}}(t_n)\right] = \boldsymbol{\sigma}(t_n) + \left[\boldsymbol{\sigma}(t_n)\mathbf{W}\left(t_{n+\frac{1}{2}}\right) + \boldsymbol{\sigma}_n \mathbf{W}\left(t_{n+\frac{1}{2}}\right)^{\mathrm{T}}\right]\Delta t + p(t_n)\mathbf{I} \tag{78}$$

secondly, the deviatoric increment from the constitutive routine is added

$$\mathrm{dev}\left[\boldsymbol{\sigma}^{\mathrm{r}}\left(t_{n+\frac{1}{2}}\right)\right] = \mathrm{dev}\left[\boldsymbol{\sigma}^{\mathrm{r}}(t_n)\right] + \mathrm{dev}\left[\overset{\circ}{\boldsymbol{\sigma}}\left(t_{n+\frac{1}{2}}\right)\right]\Delta t \tag{79}$$

The hydrostatic pressure at t_{n+1} is obtained from the equation of state

$$p = p(V, E) \tag{80}$$

where V is the relative volume and E is the internal energy. The internal energy is updated as

$$E(t_{n+1}) = E(t_n) + \Delta E \tag{81}$$

where

$$\Delta E = m\frac{\mathrm{D}e}{\mathrm{D}t}\Delta t = m\varrho^{-1}\boldsymbol{\sigma} : \mathbf{D}\Delta t = v\,\mathrm{dev}(\boldsymbol{\sigma}) : \mathbf{D}\Delta t - vp\dot{V}\Delta t \tag{82}$$

Here m and v are the current element volume and mass, respectively, and V is the relative volume. The temporal discretization of this equation is

$$\Delta E = \frac{1}{2}\left[v(t_n) + v(t_{n+1})\right]\frac{1}{2}\left\{\mathrm{dev}\left[\boldsymbol{\sigma}(t_n)\right] + \mathrm{dev}\left[\boldsymbol{\sigma}(t_{n+1})\right]\right\} : \mathbf{D}\left(t_{n+\frac{1}{2}}\right)\Delta t - \frac{1}{2}\Delta vp \tag{83}$$

and an iterative procedure is performed according to

$$p_n \overset{\text{Eq.83,81}}{\rightarrow} E^*_{n+1} \overset{\text{Eq.80}}{\rightarrow} p^*_{n+1} \overset{\text{Eq.83,81}}{\rightarrow} E_{n+1} \overset{\text{Eq.80}}{\rightarrow} p_{n+1} \tag{84}$$

Finally the new pressure $p(t_{n+1})$ is added to the stress tensor

$$\boldsymbol{\sigma}^{\mathrm{r}}(t_{\mathrm{n+1}}) = \mathrm{dev}\left[\boldsymbol{\sigma}^{\mathrm{r}}(t_{\mathrm{n+1}})\right] + p(t_{\mathrm{n+1}})\mathbf{I} \tag{85}$$

After computing the internal force vector the acceleration at time $t_{\mathrm{n+1}}$ is given by

$$\mathbf{a}(t_{\mathrm{n+1}}) = \mathbf{M}_{\mathrm{d}}^{-1}\left[\mathbf{f}_{\mathrm{ext}}(t_{\mathrm{n+1}}) - \mathbf{f}_{\mathrm{int}}(t_{\mathrm{n+1}}) + \mathbf{f}_{\mathrm{stab}}(t_{\mathrm{n+1}})\right] \tag{86}$$

and the mid velocities are updated to time $t_{\mathrm{n+1}}$ as

$$\mathbf{v}(t_{\mathrm{n+1}}) = \mathbf{v}\left(t_{\mathrm{n+\frac{1}{2}}}\right) + \mathbf{a}(t_{\mathrm{n+1}})\left(t_{\mathrm{n+1}} - t_{\mathrm{n+\frac{1}{2}}}\right) \tag{87}$$

Finally the energy balance is controlled and, unless the computation is terminated, the current time is updated and the procedure is repeated.

3.3 Shock waves

The presence of singular surfaces, cf. Truesdell and Toupin [29], results in multiple solutions to the field equations. Shock waves, defined as singular surfaces of first order with discontinuous deformation gradient and longitudinal velocity, can occur in materials where the sound velocity increases with increasing pressure. Shock waves are treated with bulk, or pseudo, viscosity that prohibits a shock wave to fully develop into a singular surface, cf. Neumann and Richtmyer [14]. The method consists in adding a hydrostatic pressure term,

$$q = \begin{cases} \varrho v^{\frac{1}{3}}\left[A v^{\frac{1}{3}}\mathrm{tr}(\mathbf{D})^2 - Bc\,\mathrm{tr}(\mathbf{D})\right], & \mathrm{tr}(\mathbf{D}) < 0 \\ 0 & , \mathrm{tr}(\mathbf{D}) \geq 0 \end{cases} \tag{88}$$

where A and B are constants and c is the material bulk sound speed, to the stress tensor in the field equations for linear momentum and energy.

4 Summary of appended publications

Numerical simulations of penetration and perforation of high performance concrete with 75mm steel projectile

The purpose of this study was to assess the ability to predict penetration depth or residual velocity with the chosen numerical methods and concrete constitutive model. The material description of the motion of both the targets and the projectiles was chosen together with a numerical erosion based on a shear strain criterion. The concrete material was modelled with the K&C concrete model and for the analysis LS-DYNA was used. For the perforation good agreement with test data was achieved but in the case of penetration, the results were not satisfying. The results were greatly influenced by the erosion criteria and the material model could not handle a discretized domain of finite element of different sizes. The conclusions were that the description of the softening behaviour had to be modified to render a fracture energy release that is independent of the spatial discretization. Also, it is not suitable to describe the target in a material reference frame, due to the need of an erosion criterion. Instead, the target should be described in a spatial reference frame, where the need for erosion is eliminated, while the material reference frame can be retained for the projectile.

Numerical simulations of the response of reinforced concrete beams subjected to heavy drop tests

The purpose of the work was to evaluate the ability of the chosen numerical method and material models to predict the material and structural response. The material model was modified to scale the softening behaviour relative the finite element sizes. The finite element analysis gave a different type of failure compared to the tests. In the test, the failure was mode I cracking combined with crushing in the impact zone. In the simulations, the failure was mainly due to mode II cracking. A material parameter analysis was performed but the results from the test could not be reproduced. The conclusion is that the modified material model does not seem to be capable of correctly describing the problem, given the material properties and the numerical method of analysis. To handle the strain localization, that occurred in the problem, it is suggested that non-local measures of deformation should be used to attain a convergent solution.

Finite element analysis of the splitting test

The purpose with this study was to evaluate the possibility to use non-local measures of deformation to attain convergence when strain localization is present.. A simplified non-local theory is used, where the local strain measure is weighted and integrated over an element neighbourhood and used to calculate the rate of evolution of the inelastic strain. The size of the neighbourhood in the non-local theory has to be determined through material characterization tests. The theory is applied to a splitting test and a tensile test for three different materials. The split test model shows mesh dependency due to a singularity. In the tensile test the non-local theory is shown to give a convergent solution. The conclusion is that it is possible to handle singularities with a non-local theory. The concrete material model will not be used in future work, due to the many problems encountered in this and previous studies. The report is concluded with a discussion on how to better model concrete material.

Bibliography

[1] *Fortifikationshandbok del 1*. Försvarsmedia, Stockholm 1991

[2] A. Abrams, Effect of rate application of load on the compressive strength of concrete. *Proc. Amer. Soc. Testing Materials* **17**, 1917, pp. 364-377

[3] *CEB-FIP model code 1990*. Thomas Telford, London 1993

[4] H.B. Kupfer, Behaviour of concrete under biaxial stress. *ACI Journal* **August**, 1969, pp. 656-666

[5] K.J. William and E.P. Warnke, Constitutive model for the triaxial beaviour of concrete, *Proceedings of the International Association for Bridge and Structural Engineering*. (1975)

[6] N.S. Ottosen *Failure and elasticity of concrete*. Danish atomic energy commision research establishment Risø, Risø-M-1801, Roskilde 1975

[7] A. Hillerborg, Analysis of crack formation and crack growth in concrete by means of fracture mechanics and finite elements. *Cement and concrete research* **6**, 1976, pp. 773-782

[8] H.W. Reinhardt, Strain rate effects on the tensile strength of concrete as predicted by thermodynamics and fracture mechanics models. *Cement based composites: Strain rate effects on fracture* 1985, pp. 1-13

[9] L. Nilsson *Impact loading on concrete structures: A constitutive modelling, finite element analysis, and experimental study of nonlinear wave propagation*, Chalmers University of Technology, Göteborg 1979

[10] L. Nilsson and M. Oldenburg, *Nonlinear Wave Propagation in Plastic Fracturing Materials - A Constitutive Modelling and Finite Element Analysis*, in *Nonlinear Deformation Waves*, U. Nigul and J. Engelbrecht, Editors, Springer Verlag, Berlin 1983.

[11] W.F. Chen *Plasticity in reinforced concrete*. McGraw-Hill, New York 1982

[12] C. Truesdell and W. Noll, *The non-linear field theories of mechanics*, in *Encyclopedia of physics*, S. Flügge, Editor Springer-Verlag, New York 1965, pp. 1-602

[13] T. Belytschko, W.K. Liu, and B. Moran *Nonlinear finite elements for continua and structures*. John Wiley, Chichester 2000

[14] J. von Neumann and R.D. Richtmyer, A method for the calculation of hydrodynamic shocks. *Journal of applied physics* **21**, 1950, pp. 232-237

[15] R.W. Ogden *Non-linear elastic deformations*. Dover publications, New York 1997

[16] J. Lubliner *Plasticity theory*. Macmillan, New York 1990

[17] R. Hill *The mathematical theory of plasticity*. Oxford university press, Oxford 1950

[18] A. Winnicki, C.J. Pearce, and N. Bicanic, Viscoplastic Hoffman consistency model for concrete. *Computers & Structures* **79**, 2001, pp. 7-19

[19] A. Hillerborg *Failure of materials (In swedish)*. Lund institute of technology, Department of building materials, TVBM-3004, Lund 1977

[20] M. Ristinmaa and N.S. Ottosen *Large strain plasticity and thermodynamics*. Dept. of Solid Mechanics, University of Lund, Lund 1996

[21] P. Perzyna, Fundamental problems in viscoplasticity. *Adv. Appl. Mech.* **9**, 1966, pp. 243-377

[22] W. Riedel *Beton unter dynamischen Lasten: Meso- und makromechanische Modelle und ihre Parameter*, Universität der Bundeswehr München, Freiburg 2000

[23] *LS-DYNA Theoretical manual*. Livermore Software Technology Corporation (LSTC), Livermore 1998

[24] L.E. Schwer and Y.D. Murray, A three-invariant smooth cap model with mixed hardening. *International journal for numerical and analytical methods in geomechanics* **18**, 1994, pp. 657-688

[25] T.J. Holmquist, G.R. Johnson, and W.H. Cook, A computational constitutive model for concrete subjected to large strains, high strain rates, and high pressures, *Proceedings of the 14th International Symposium on Ballistics*. (1993), pp. 591-600

[26] L.J. Malvar, et al., A plasticity concrete material model for dyna3d. *International Journal of Impact Engineering* **19**, 1997, pp. 847-873

[27] *LS-DYNA Keyword user's manual, version 950*. Livermore Software Technology Corporation (LSTC), Livermore 1999

[28] J. Lemaitre and J.-L. Chaboche *Mechanics of solid materials*. Cambridge university press, Cambridge 1990

[29] C. Truesdell and R. Toupin, *The classical field theories*, in *Encyclopedia of physics*, S. Flügge, Editor Springer-Verlag, Berlin-Göttingen-Heidelberg 1960, pp. 226-793

APPENDIX I

DEFENCE RESEARCH
ESTABLISHMENT

FOA-R--00-01634-311--SE
November 2000
ISSN 1104-9154

User report

Mattias Unosson

Numerical simulations of penetration and perforation of high performance concrete with 75mm steel projectile

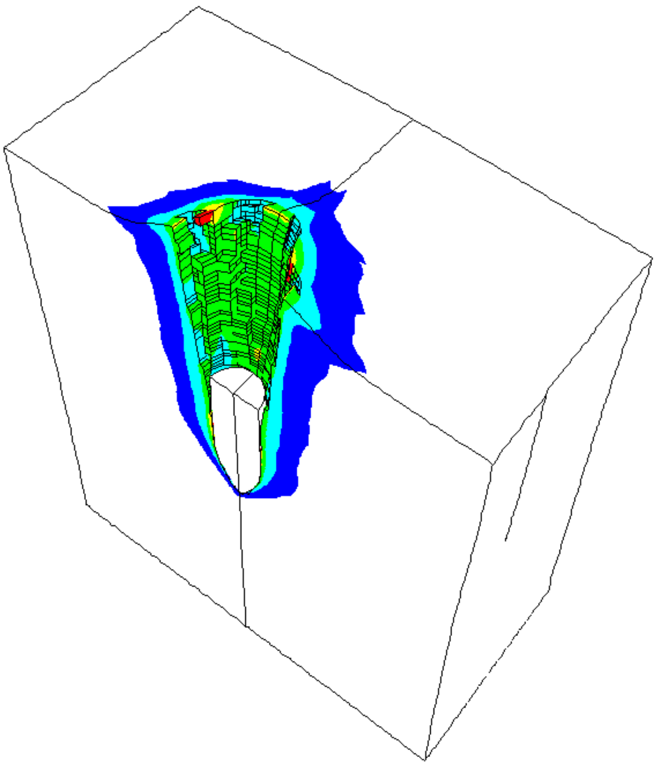

Weapons and Protection Division
SE-147 25 TUMBA

DEFENCE RESEARCH ESTABLISHMENT
Weapons and Protection Division
SE-147 25 TUMBA

FOA-R--00-01634-311--SE
November 2000
ISSN 1104-9154

Mattias Unosson

Numerical simulations of penetration and perforation of high performance concrete with 75mm steel projectile

Distribution: HKV/KRI/PLAN/Anlägning, FortV, FHS, FFI, Dynalis, Engineering Research AB, EMI Freiburg, Karagozian & Case

FOA: FOA Program, FOA 2

Issuing organization	Document ref. No., ISRN	
Defence Research Establishment Weapons and Protection Division SE-147 25 TUMBA SWEDEN	FOA-R--00-01634-311--SE	
	Date of issue November 2000	**Project No.** E2614
	Project name (abbrev. if necessary) HPC	
Author(s) Mattias Unosson	**Initiator or sponsoring organization** Swedish Defence Headquarter	
	Project manager Anders Carlberg	
	Scientifically and technically responsible	

Document title

Numerical simulations of penetration and perforation of high performance concrete with 75mm steel projec

Abstract

In the report, simulations of penetration and perforation of three types of high performance concrete (HPC) targets are presented and compared with experimental data. The objective of the simulations was to assess the chosen concrete material model's ability to predict depth of penetration or residual velocity. The tests were simulated numerically with the code LS-DYNA and the standard material type 72, "Concrete Damage". Lagrangian solution technique was used together with numerical erosion based on a shear strain criteria. For the perforation good agreement with test data was achieved but in the case of penetration, the results were not satisfying.

Keywords

Numerical simulation, LS-DYNA, high performance concrete, penetration, perforation, steel projectile

Further bibliographic information	Language English
ISSN 1104-9154	**ISBN**
	Pages 67 p.

Distributor (if not issuing organization)

Dokumentets utgivare Försvarets forskningsanstalt Avdelningen för Vapen och skydd SE-147 25 TUMBA	**Dokumentbeteckning, ISRN** FOA-R--00-01634-311--SE **Dokumentets datum** november 2000 **Uppdragsnummer** E2614 **Projektnamn (ev förkortat)** HPC
Upphovsman(män) Mattias Unosson	**Uppdragsgivare** HKV **Projektansvarig** Anders Carlberg **Fackansvarig**

Dokumentets titel

Numeriska simuleringar av penetration och perforation av högpresterande betong med 75mm stålprojektil

Sammanfattning

I rapporten presenteras simuleringar av perforation och penetration i tre typer av mål gjutna av höpresterande betong och resultaten jämföres med försöksdata. Syftet med simuleringarna var att utvärdera den valda materialmodellens förmåga att förutsäga penetrationsdjup eller projektilens residualhastighet. Försöken simuleras med koden LS-DYNA och materialtyp 72, ”Concrete damage”. Lagrangeteknik tillämpas på problemet tillsammans med numerisk erosion baserad på skjuvtöjning. För perforation är överensstämmelsen med försöksdata god men för penetration är överensstämmelsen ej tillfredsställande.

Nyckelord

Numerisk simulering, LS-DYNA, högpresterande betong, penetration, perforation, stålprojektil

Övriga bibliografiska uppgifter	**Språk** Engelska
ISSN 1104-9154	**ISBN**
	Omfång 67 s.

Distributör (om annan än ovan)

CONTENTS

1 INTRODUCTION

The simulations in this report were part of the HPC-project in which the following Swedish and Norwegian organisations co-operated during the years 1997 – 2000 to build up their competence in high strength concrete (HPC):

Sweden

- Armed Forces Headquarter (HKV), http://www.mil.se/
- Defence Research Establishment (FOA), http://www.foa.se/
- Fortification Administration (FortV), http://www.fortv.se/

Norway

- Headquarters Defence Command (FO), http://www.fo.mil.no/
- Defence Research Establishment (FFI), http://www.ffi.no/
- Defence Construction Service (FBT), http://www.mil.no/fbt

The penetration and perforation test, upon which the simulations presented in this report are based on, were performed in Karlskoga at the Bofors Testing Centre (http://www.bofors.se/testcenter) 1999-10-05—07 comprising nine tests at three types of cylindrical concrete targets.

2 TESTS

A 6.3kg armour piercing steel projectile with an ogival nose radius of 127mm, a length of 225mm and diameter of 75mm was fired at the targets, see Figure 1. The projectile impacted with approximately zero angle of attack and a velocity of about 620m/s (cf. Figure 2 and Figure 3). Targets 1-3 were penetration tests (projectile comes to rest in the target) and targets 4-9 were perforation tests (projectile passes through target). In Table 1 the target specifications and global test results are presented.

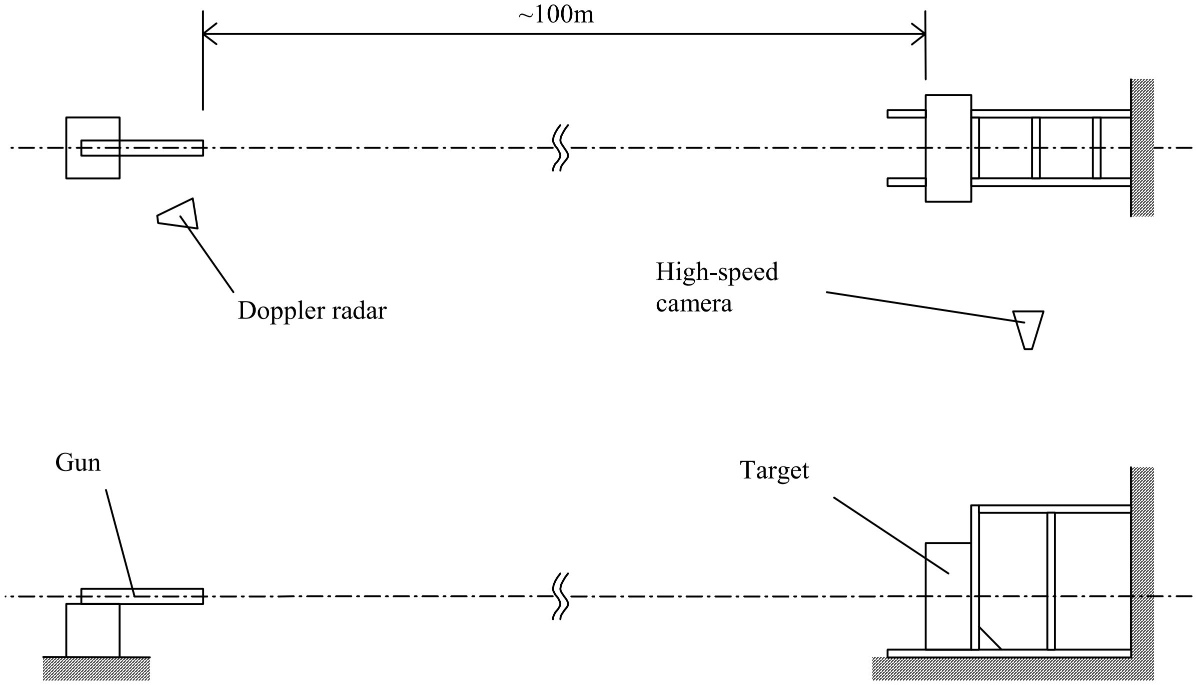

Figure 1. Experimental set up

Table 1. Target specifications and test results

Target number	Diameter [mm]	Length [mm]	Reinforcement mass ratio	Projectile impact velocity [m/s]	Depth of penetration [mm]	Projectile residual velocity [m/s]
1	1 400	800	0.00	617	450	-
2	1 400	800	0.00	612	540	-
3	1 400	800	0.00	619	510	-
4	1 400	400	0.00	616	-	276*
5	1 400	400	0.00	616	-	303*
6	1 400	400	0.00	618	-	293*
7	1 400	400	0.06	617	-	Not measured
8	1 400	400	0.06	616	-	Not measured
9	1 400	400	0.06	616	-	260

*: *Data from FFI*

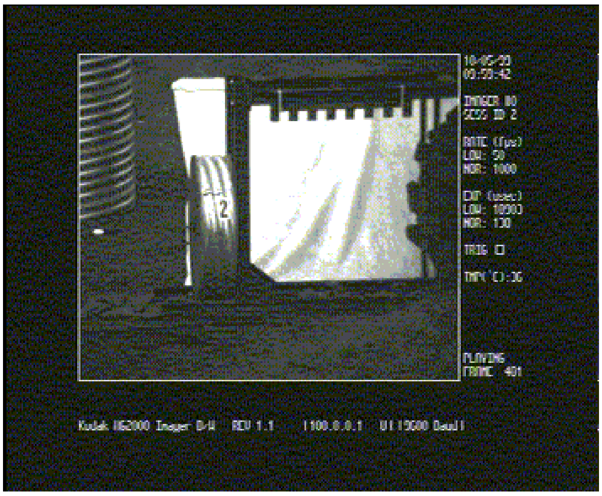

Figure 2. Photo from high-speed camera before impact (target 5 with projectile to the left)

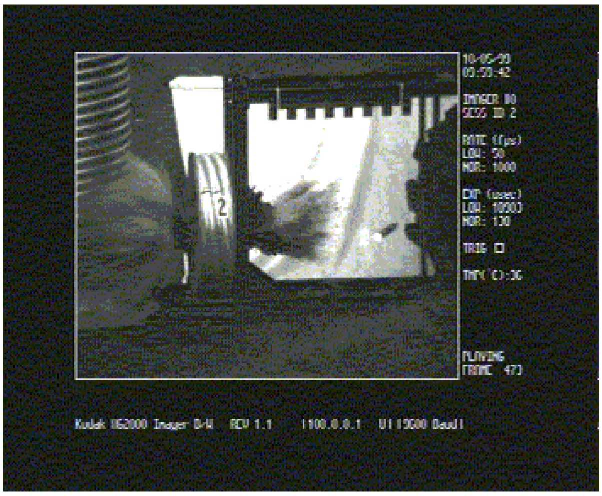

Figure 3. Photo from high-speed camera after perforation (target 5 with projectile to the right)

Figure 4. Post-test condition for projectile used for target number 8

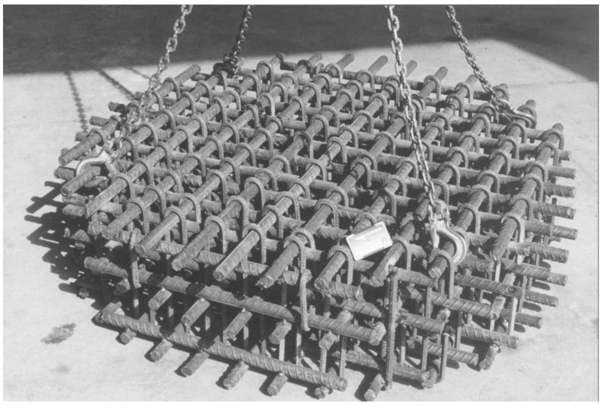

Figure 5. Reinforcement in targets 7-9

Inspection of the projectiles after the tests showed that no or negligible erosion and plastic deformation had occurred (cf. Figure 4) neither in the penetration nor in the perforation case.

Three different types of targets and three targets for each type were tested, i.e. nine targets in total. During and after the tests the following registrations were made:

- Doppler radar giving the time-velocity relation for the projectile.
- High-speed camera giving the projectile residual velocity for perforation tests.
- Depth of penetration.

Targets 7-9 were reinforced with cages as the one shown in Figure 5. These cages were constructed in a three dimensional grid with 100mm spacing between rebars (D=12mm) and stirrups (D=10mm). Both the rebars and the stirrups were of steel quality Ks 500 ST.

In Figure 6 to Figure 9 data from the Doppler radar is plotted for each type of target. When comparisons with results from simulations are made, these curves are integrated and combined with the residual velocities taken from the high-speed photos.

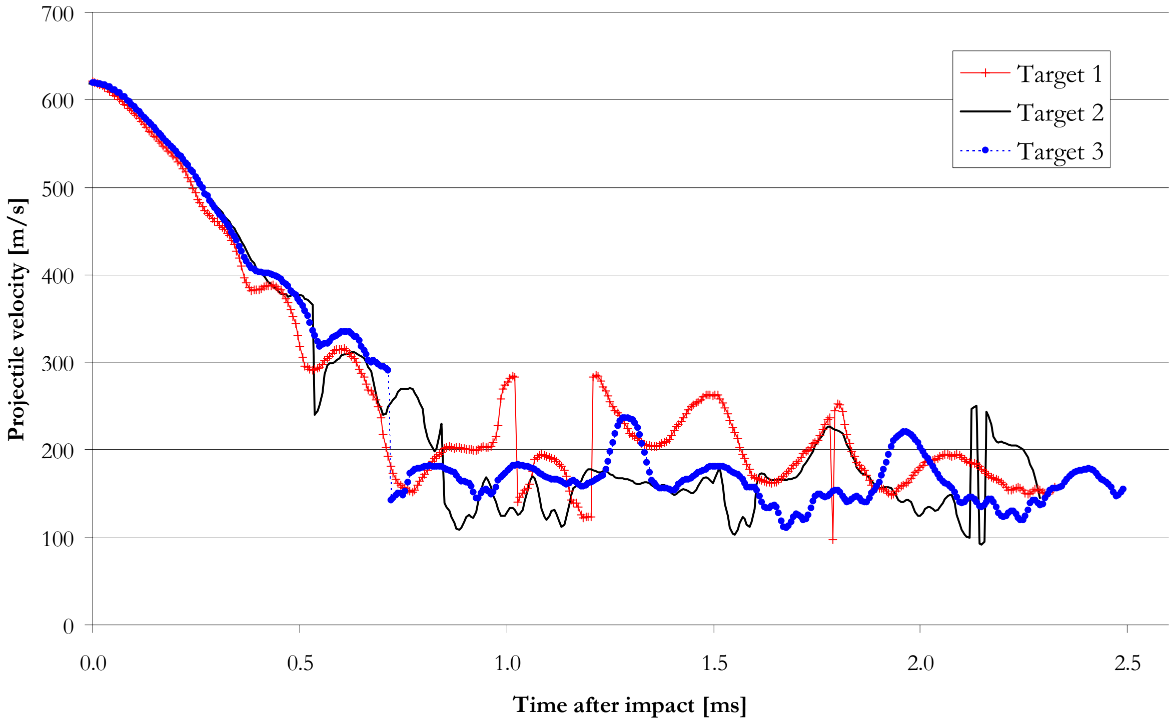

Figure 6. Projectile velocity versus time for targets 1-3.

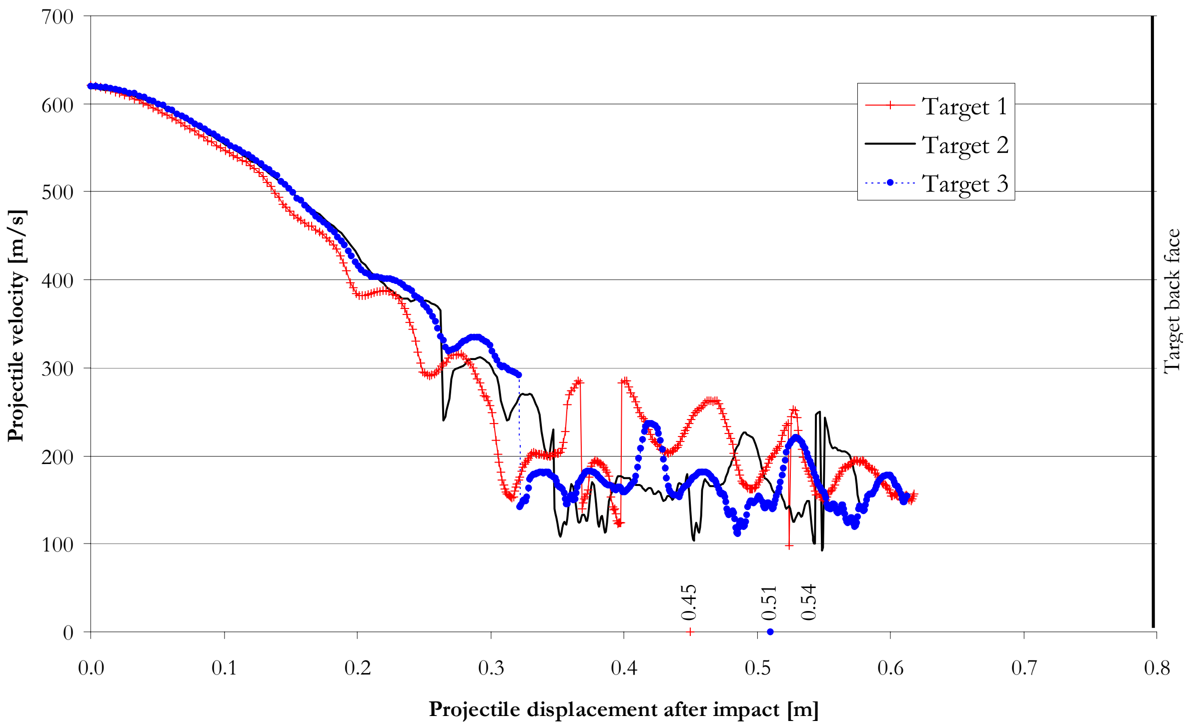

Figure 7. Projectile velocity versus displacement for targets 1-3 (including three points for the post-test measured depth of penetration).

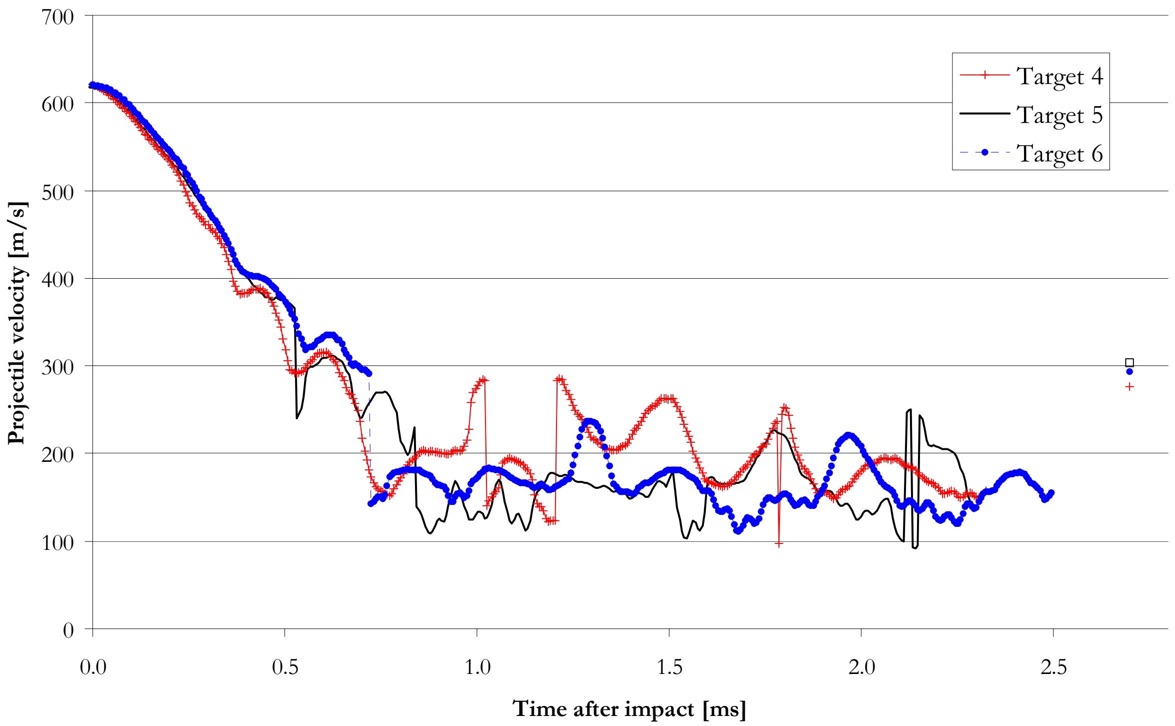

Figure 8. Projectile velocity versus time for targets 4-6 (including three data points from the high-speed camera).

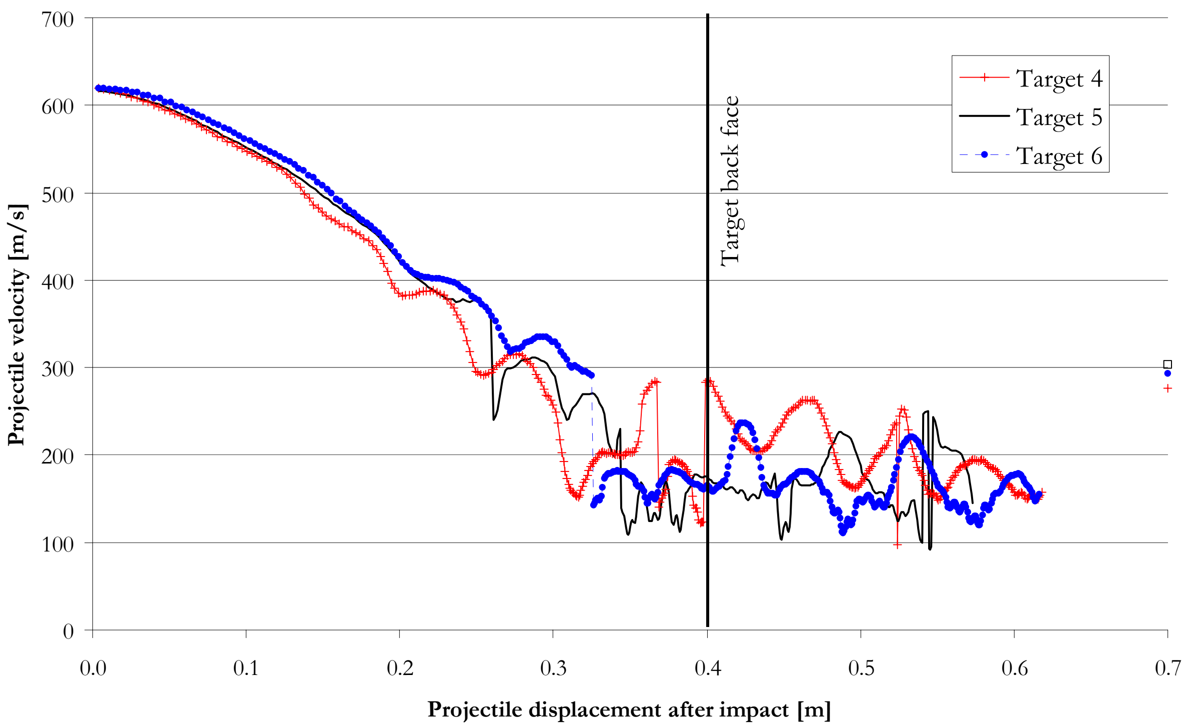

Figure 9. Projectile velocity versus displacement for targets 4-6 (including three data points from the high-speed camera).

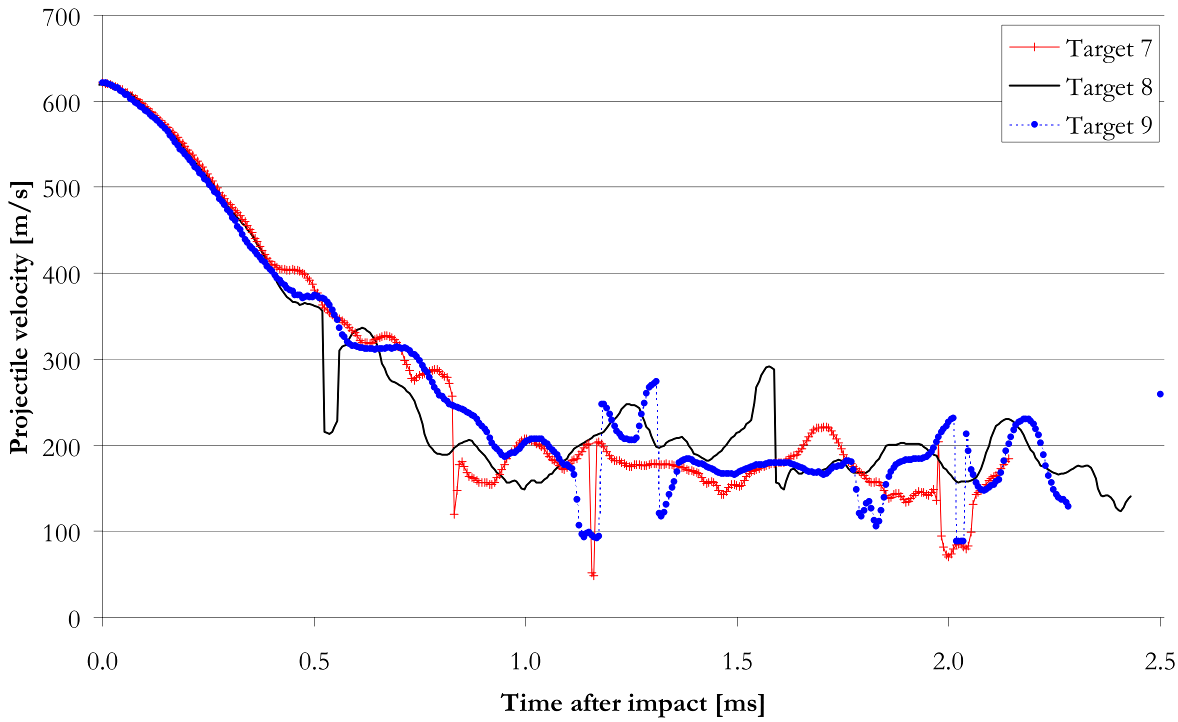

Figure 10. Projectile velocity versus time for targets 7-9 (including one data point from the high-speed camera).

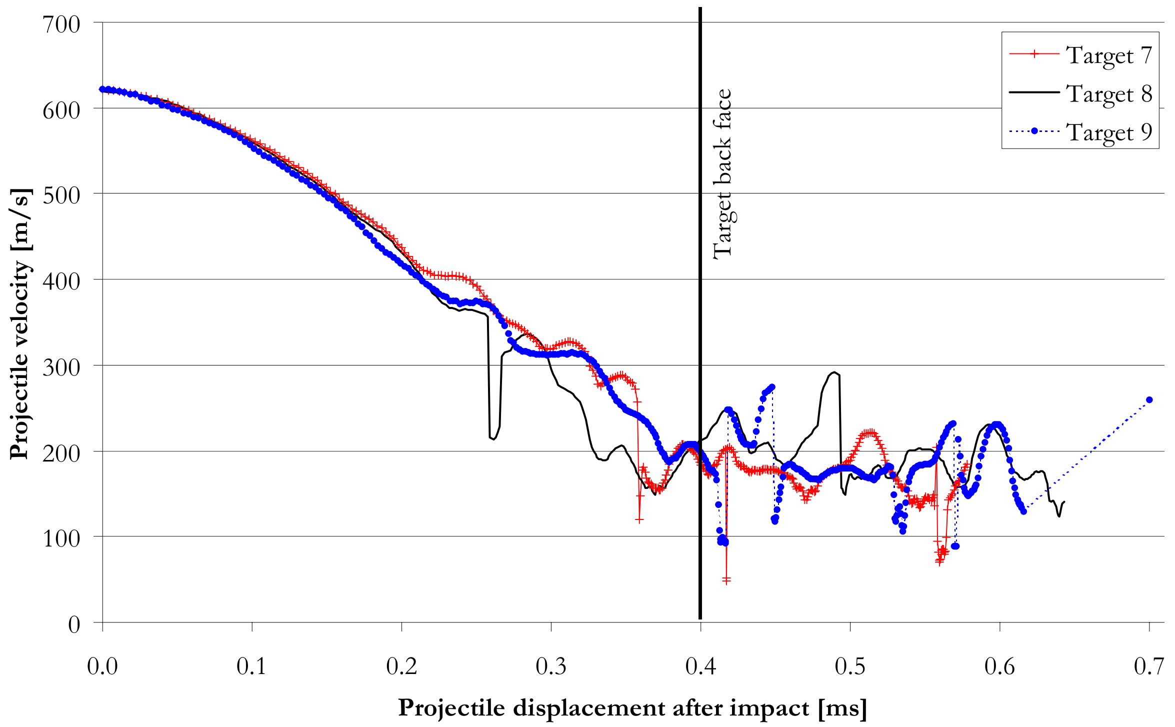

Figure 11. Projectile velocity versus displacement for targets 7-9 (including one data points from the high-speed camera).

When using only one Doppler radar it is not possible to distinguish signals from objects moving towards the radar from objects moving away from the radar. Therefor the data in the above figures should only be used as guidance.

3 MATERIAL CHARACTERISATION

3.1 Target

Standard material testing was performed on 150x150mm cubes for the unconfined uniaxial compressive strength, 100x200mm cylinders for the splitting tensile strength and the modulus of elasticity. Determination of the fracture energy was done according to RILEM "Determination of the fracture energy of mortar and concrete". The results are presented in Table 2.

Table 2. Concrete material test data

Mass density	Uniaxial compressive strength	Splitting tensile strength	Modulus of elasticity	Fracture energy
2 770kg/m^3	153MPa	9.1MPa	58GPa	162N/m

By default the Poisson's constant is taken as 0.16 and the uniaxial tensile strength is taken as 90% of the split strength according to The Swedish Concrete Handbook [4].

For the reinforcement the parameters in Table 3 were taken from earlier tests performed on the same type of reinforcement, 12mm rebars with quality KS500ST. The strain at maximum force (peak strain) was determined according to ISO 10606:1995(E).

Table 3. Reinforcement material test data.

Mass density	Yield stress	Poisson's ratio	Modulus of elasticity	Hardening modulus	Peak strain
7 800kgm^{-3}	586MPa	0.3	207GPa	1.1GPa	0.092

3.2 Projectile

The Vicker's test (HV10) was performed on one of the projectiles after the tests and the yield limit was calculated according to the following relationship.

$$f_{sy} \approx \frac{100 \cdot 10^6}{32} HV_{10}$$

The results from the Vicker's test together with the calculated yield limit is presented in Figure 12 and the parameters in Table 4 were chosen from standard steel data.

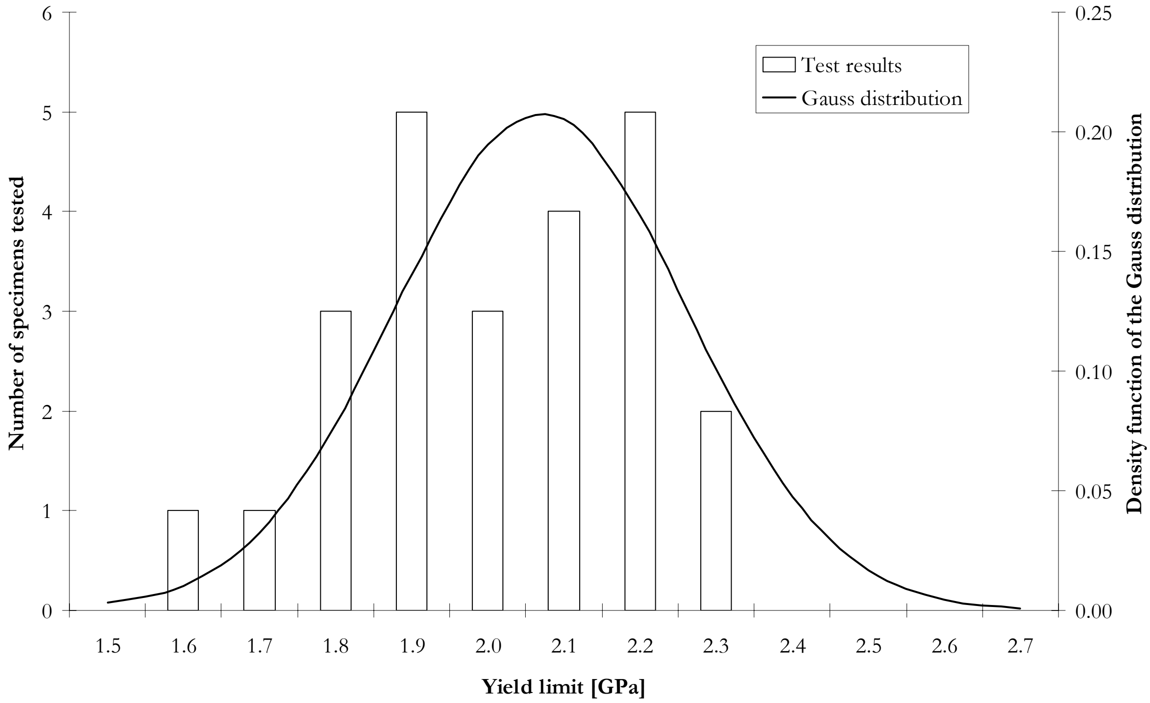

Figure 12. Results from the Vicker's test (HV10) performed on a projectile after tests.

Table 4. Projectile elastic material parameters.

Mass density	Modulus of elasticity	Poisson's ratio
7 800kg/m^3	200GPa	0.3

4 NUMERICAL SIMULATIONS

The tools used for the simulations are specified in Table 5.

The geometry was modelled with two symmetry planes and both the target and the projectile were described in Lagrangian co-ordinates. All nodes on the target's perimeter were constrained to no displacement in the direction of the projectiles path. For the contact between target and projectile, the standard LS-DYNA algorithm "eroding surface to surface" was used. This is the only available contact algorithm that can be used together with numerical erosion, i.e. that updates the contact surfaces after each computational time step to account for eroded elements.

The target was modelled using 8-node solid elements and an erosion criterion based on shear strain. The numerical erosion can only be used with solid elements and 1-point integration. The critical erosion value had to be determined through an iterative procedure, which is presented in Chapter 4.2. For the target elements, hourglass control of the type Flanagan-Belytschko stiffness form with exact volume integration were used. For the target the LS-DYNA material type 72 "Concrete Damage" was used, see Appendix B for a detailed presentation of the material model. Since neither the material type number 72 nor the numerical erosion option is available in the pre-processor LS-INGRID changes had to be done in the LS-DYNA input file.

The projectile was modelled using 8-node solid elements with 8-points integration and an elastic material model, LS-DYNA material type 2. The same mesh was used for all simulations and specifications are given in Table 6.

The reinforcement was modelled using 2-node truss elements and the LS-DYNA elastic-plastic material type 3 together with the material parameters given in Table 3.

Table 5. System specifications.

Compaq Workstation XP1000
667 MHz DEC/Alpha 21264A processor with 1024 MB main memory
Digital UNIX version 4.0d
LS-INGRID versions 3.5a and 3.5b [6]
LS-DYNA version 950c [1]
LS-TAURUS version 940.3 [3]

Table 6. Mesh data for projectile

Nodes	484
Solid elements	252
Characteristic element size	7.5 mm

Now follows a detailed explanation of the chosen input data for the target. The maximum compression meridian was fitted to the one given by the CEB-FIP Model Code 1990 [5] and the initial compression yield meridian and the residual compression meridian were constructed according to the instructions in [2]. In Figure 13 three different stress-paths are drawn together with the maximum compression meridian. In Figure 14 both the compression and tension meridians are shown for pressure up to 1.7GPa.

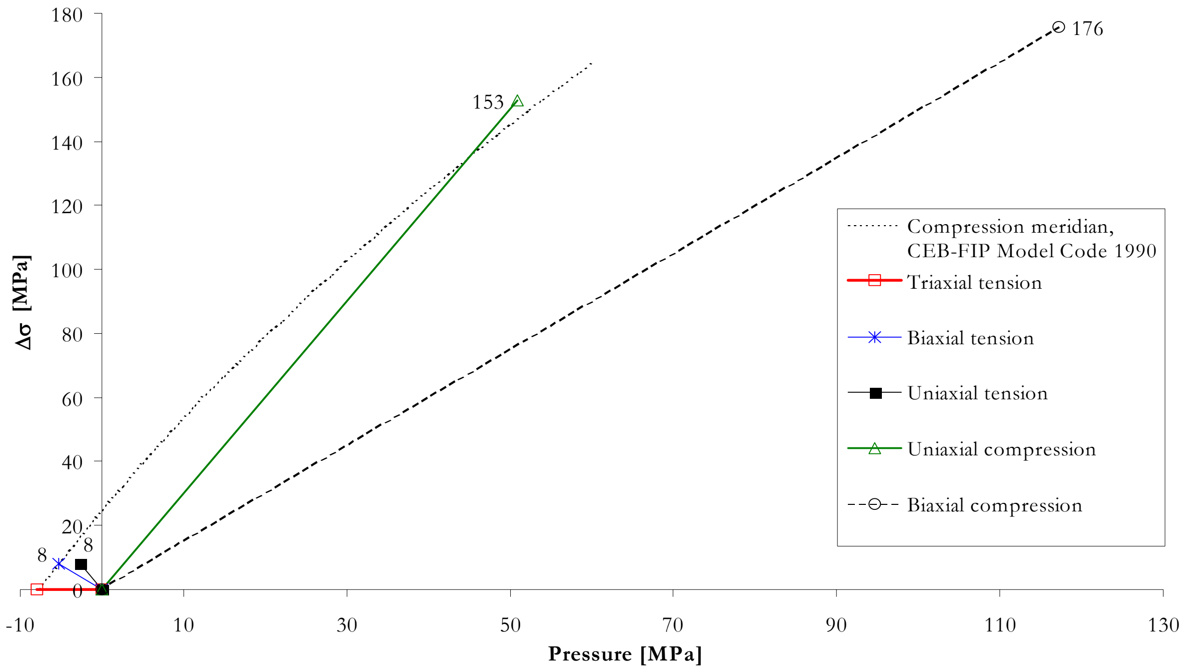

Figure 13. Compressive meridian and test stress paths.

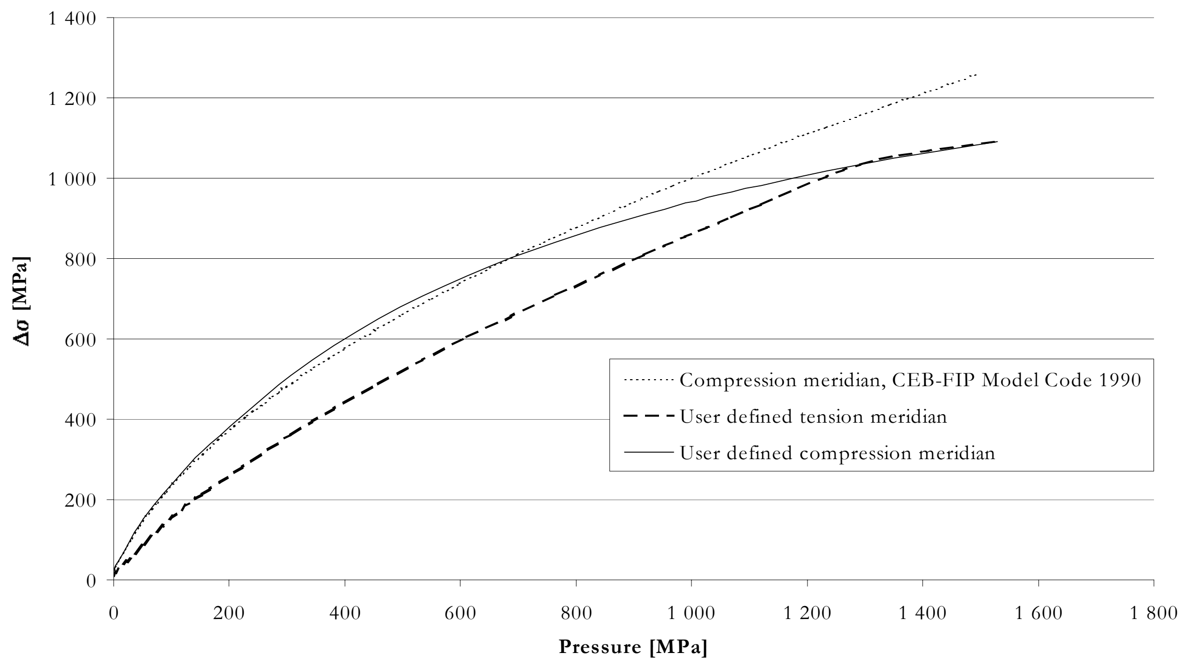

Figure 14. Compressive and tensile meridian used for the simulations.

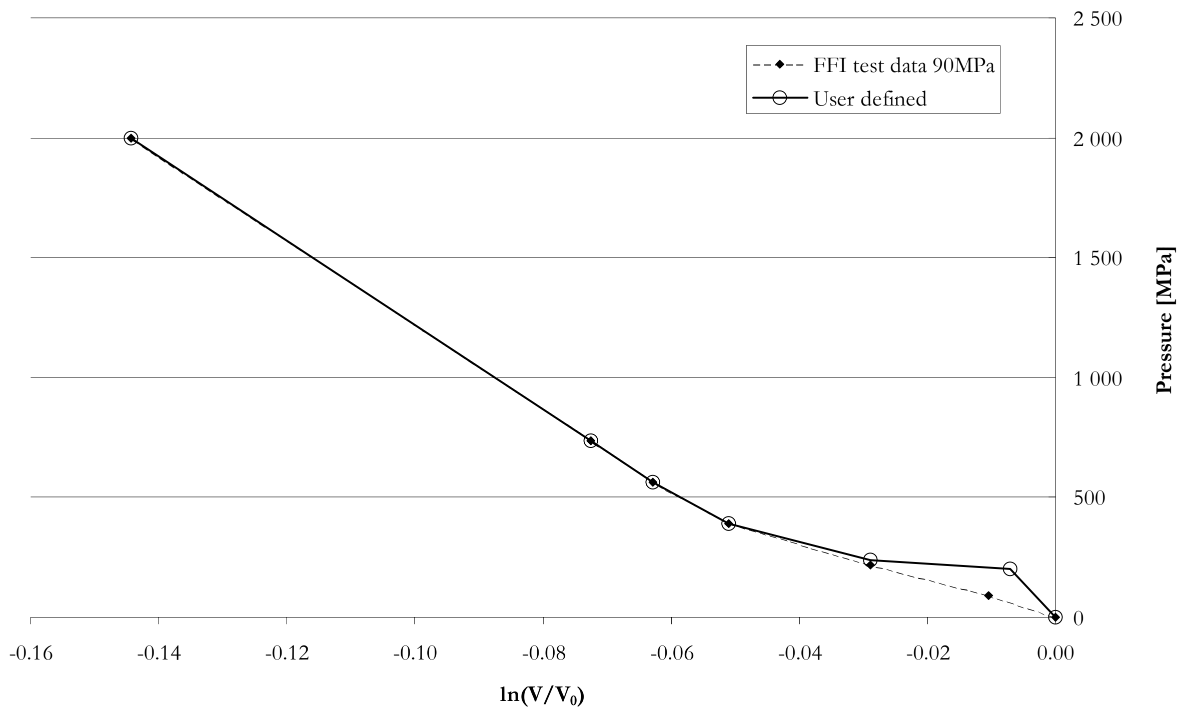

Figure 15. Equation of state used for the simulations.

For the equation of state, a combination of test data from FFI on concrete with cube strength of 90MPa and the data given in Table 1 on the modulus of elasticity was used. The slope of the elastic-porous part was calculated as:

$$K = \frac{E}{3(1-2\upsilon)} = \frac{58}{3(1-2\cdot 0.16)} = 28.43\,\text{GPa}$$

The curve was then connected to the FFI-curve. The difference in inclination for the elastic part is due to the GREAC-cell method used for the FFI-tests. It has been shown that this testing method gives a weaker response than that of a stabilised HOEK-cell [7]. The last point on the curve was extrapolated and the resulting equation of state is shown in Figure 15.

In the model, there are three parameters which controls the shape of the response curves, b1 for uniaxial compression, b2 for uniaxial tension and b3 for tri-axial tension. The value for b1 was taken according to the recommendations in [1]. To regularise the fracture energy release these parameters has to be determined for each element size to be used so that

$$G_f = h\int_{\varepsilon} \sigma(\varepsilon)d\varepsilon = 162Nm^{-1}$$

where

$$h = \sqrt[3]{V_0^{element}}$$

The damage parameters were determined by simulations of a direct tension test. The softening part of the response was fitted to the following analytical expression using a bilinear softening curve.

$$\sigma_{ct}(w) = f_{ct} e^{\left(-\frac{f_{ct} w}{G_f}\right)}$$

The input damage curve is shown in Figure 16.

For the two element sizes that were to be used in the simulations, 5 and 7.5mm, the damage parameters were tuned to get the right fracture energy. The resulting response curves for uniaxial compression, uniaxial tension and triaxial tension are shown in Figure 17 to Figure 19. The LS-Ingrid input file, valid for uniaxial and triaxial tension tests and uniaxial compression test depending on which command lines that are commented out, is found in Appendix B. According to [2] this tuning of damage parameters is enough to avoid mesh dependency.

To assure that the input curve for strain rate dependency covers the whole range of strain rates occurring in the simulations, registrations of the effective strain rates (upon which the strength enhancement in the model is based) were made for three elements in the impact area, see (Figure 20). At time 0.022ms the first element, element 1 is eroded.

The suggested bilinear relationship for the dynamic increase factor (DIF) in [5] is valid for strain rates up to 300/s. In Figure 21 this relationship is plotted up to the observed strain-rate values.

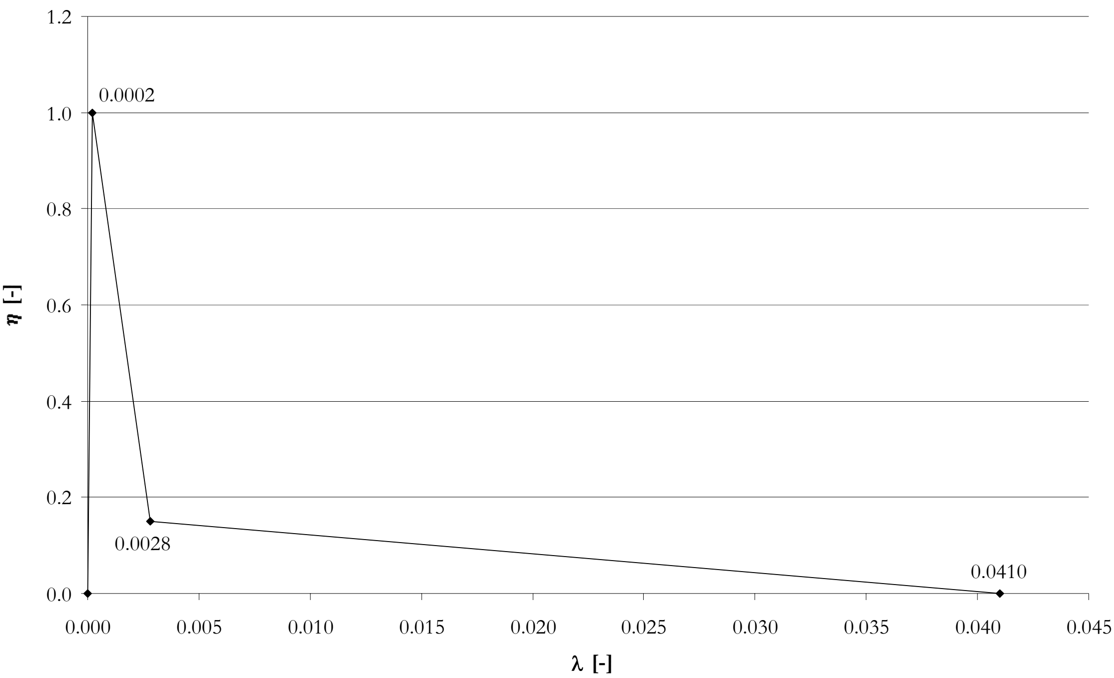

Figure 16. Damage curve used in the simulations.

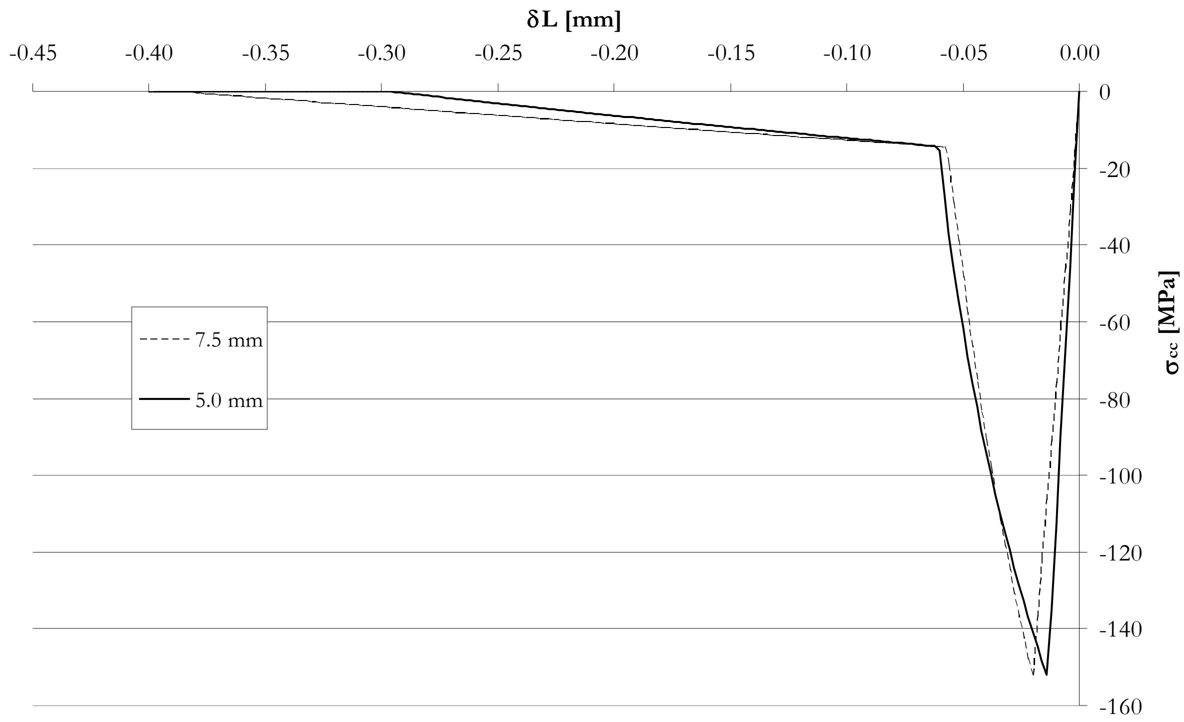

Figure 17. Response curves for element sizes 5 and 7.5 mm in uniaxial compression.

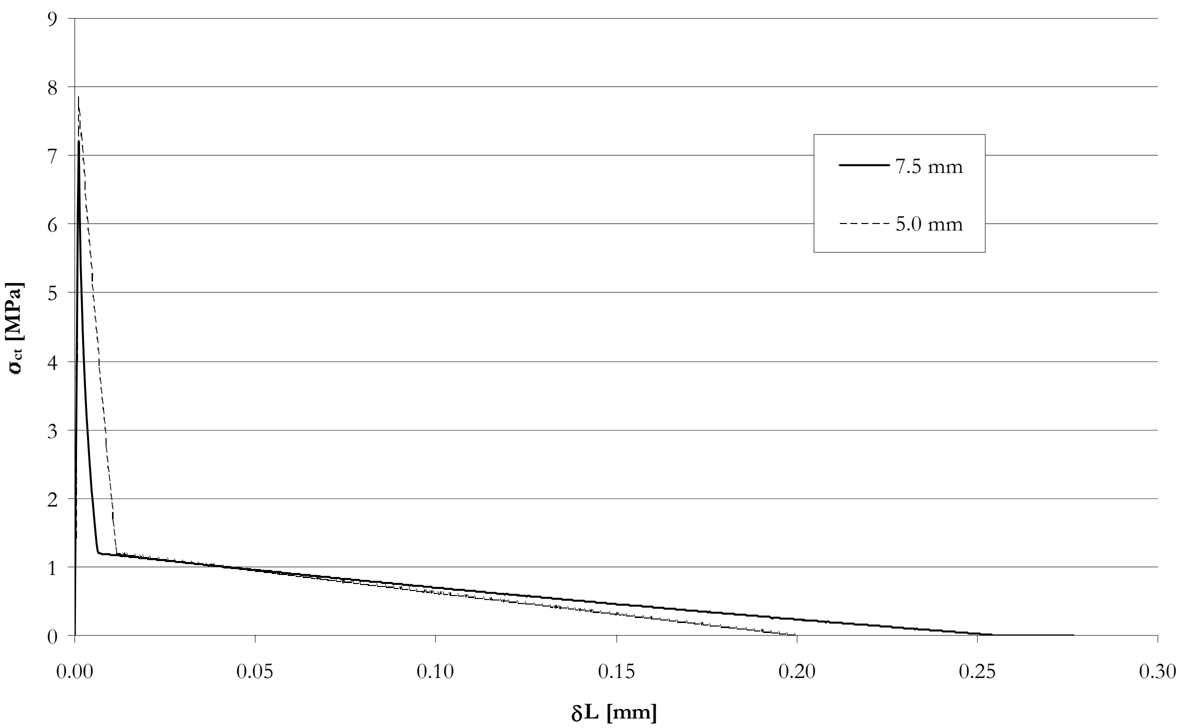

Figure 18. Response curves for element sizes 5 and 7.5 mm in uniaxial tension.

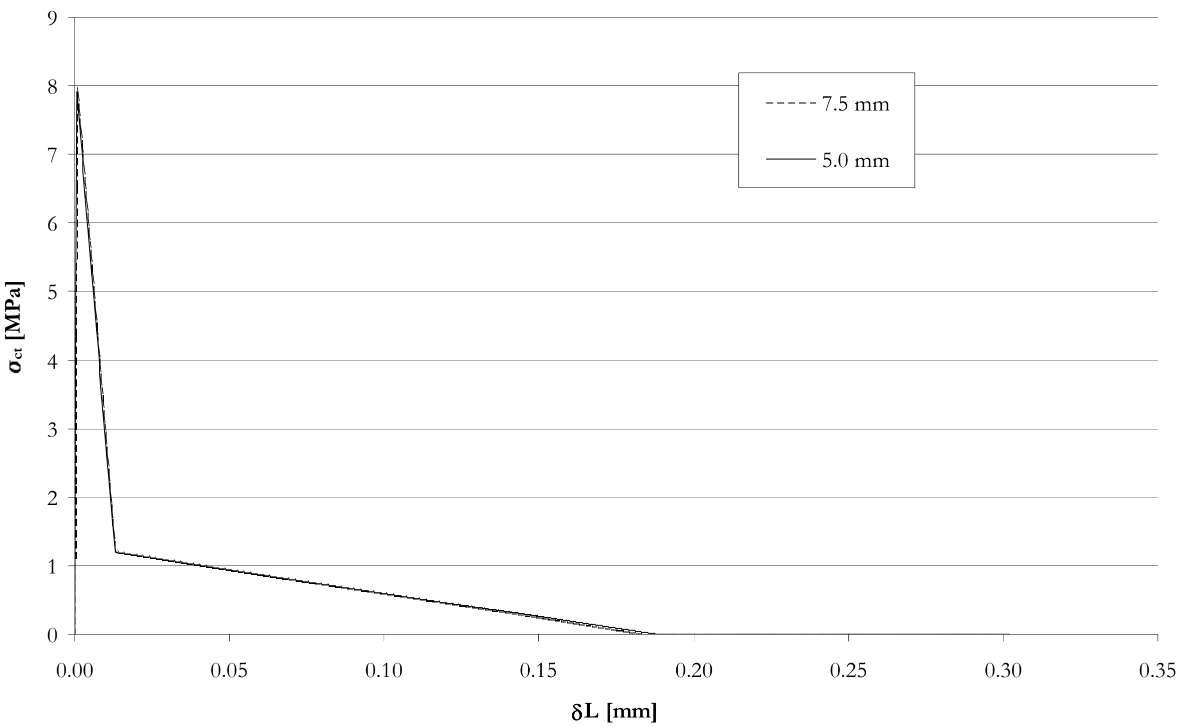

Figure 19. Response curves for element sizes 5 and 7.5 mm in triaxial tension.

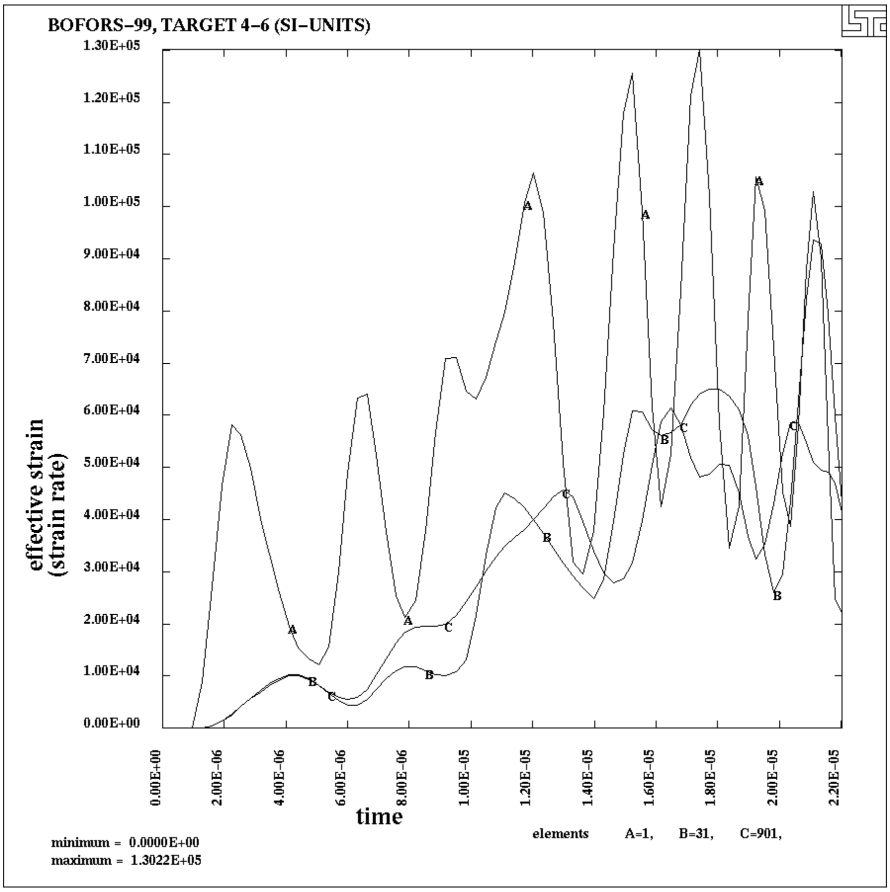

Figure 20. Strain rates in the targets impact area.

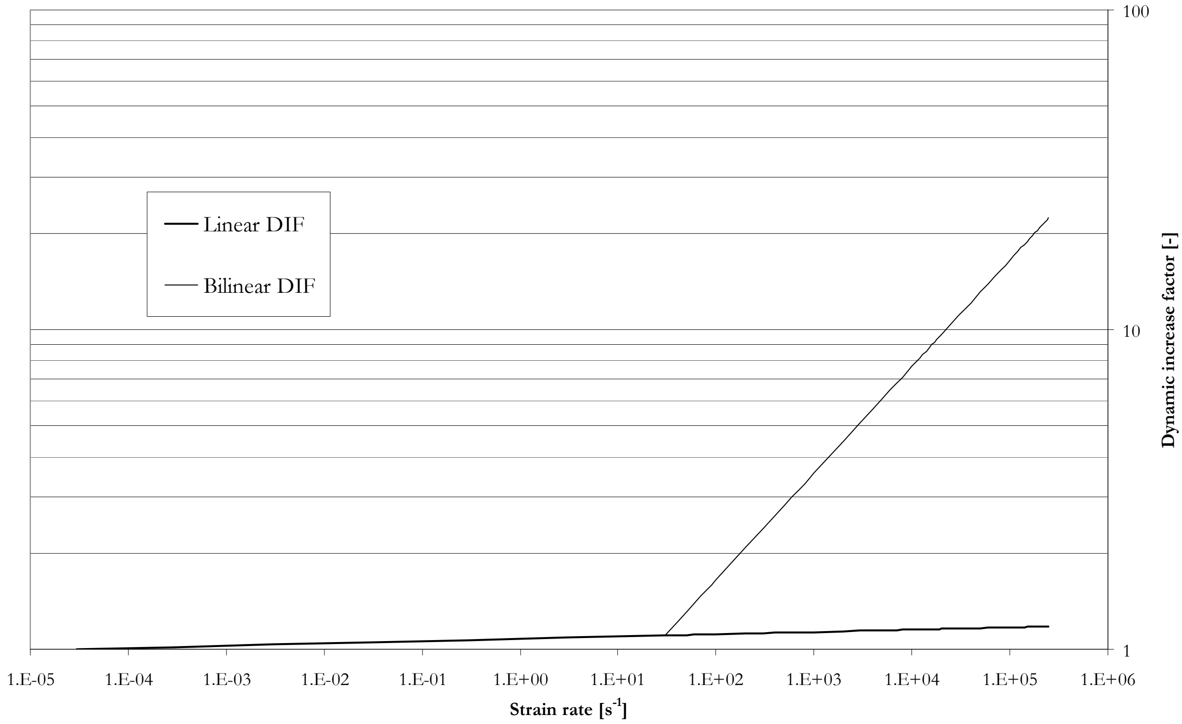

Figure 21. Dynamic increase factor (DIF) according to [5] for uniaxial compression strength (recommended up to 300/s).

4.1 Target 1-3

The LS-INGRID input file and changes made to the created LS-DYNA keyword format input file is found in Appendix D. The mesh used for this target type is shown in Figure 22 and Figure 23. A mesh specification is given in Table 7.

The effects of dynamic strength increase of strain rate were investigated. Three curves for compressive strength enhancement were used (cf. Figure 21); no strength enhancement, linear strength enhancement and bilinear strength enhancement. The Doppler radar curves were integrated and plotted together with the measured penetration depths and the three resulting projectile velocity-displacement curves from the simulations, see Figure 24 and Figure 25. Only data up to 0.5ms was used from the Doppler radar according to discussion in Chapter 2.

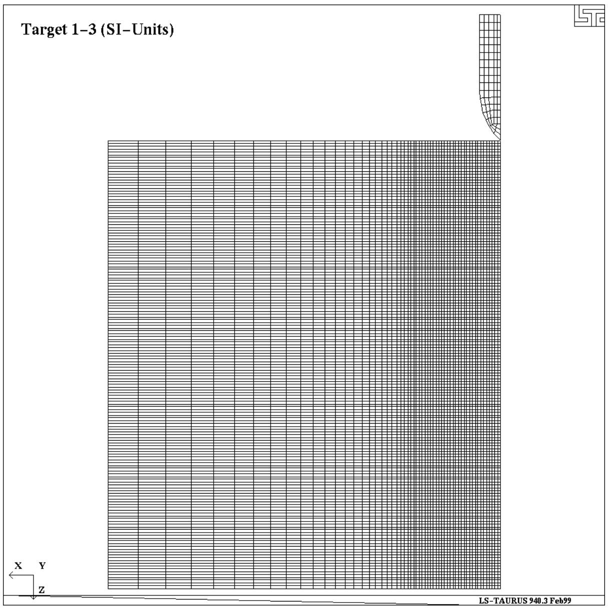

Figure 22. Mesh A in elevation view.

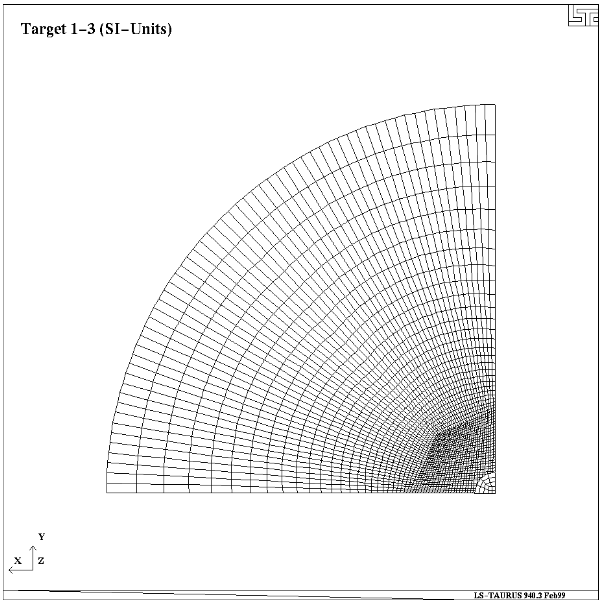

Figure 23. Mesh A in plan view.

Table 7. Mesh data for target 1-3.

Mesh	A
Characteristic element size	5mm
Nodes	419 800
Solid elements	403 200
Approx. CPU time	12 h

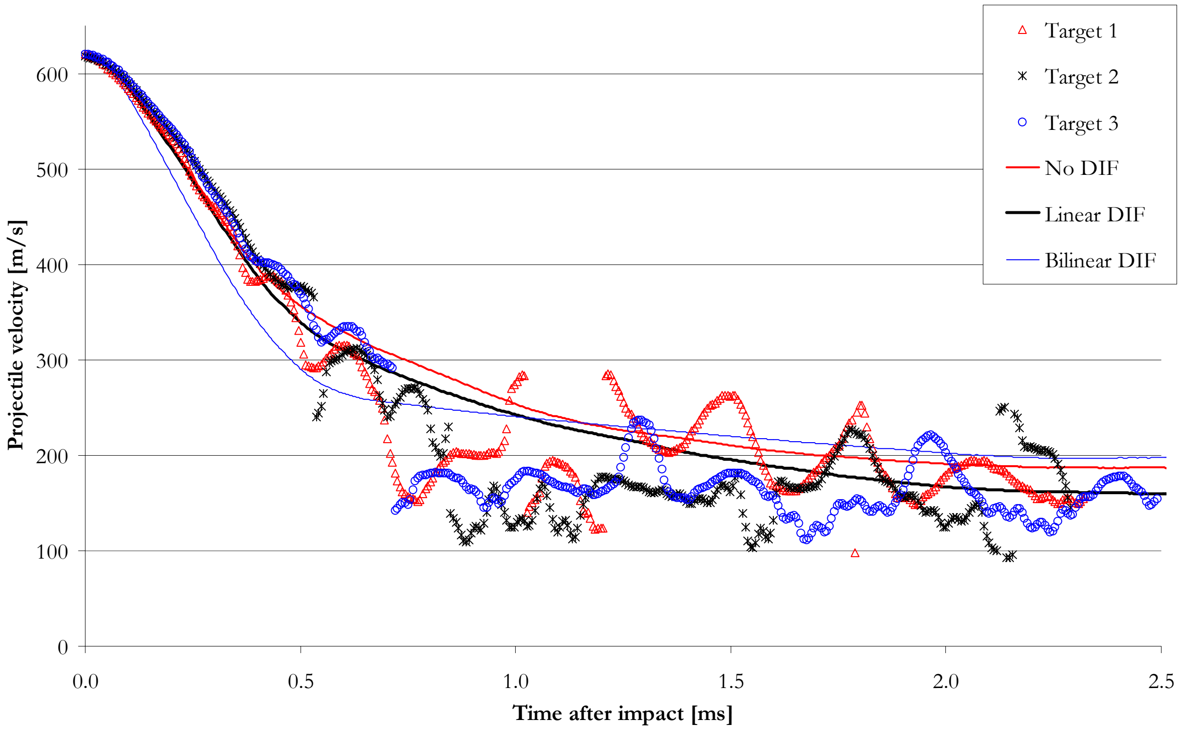

Figure 24. Comparison between numerical simulations and test data.

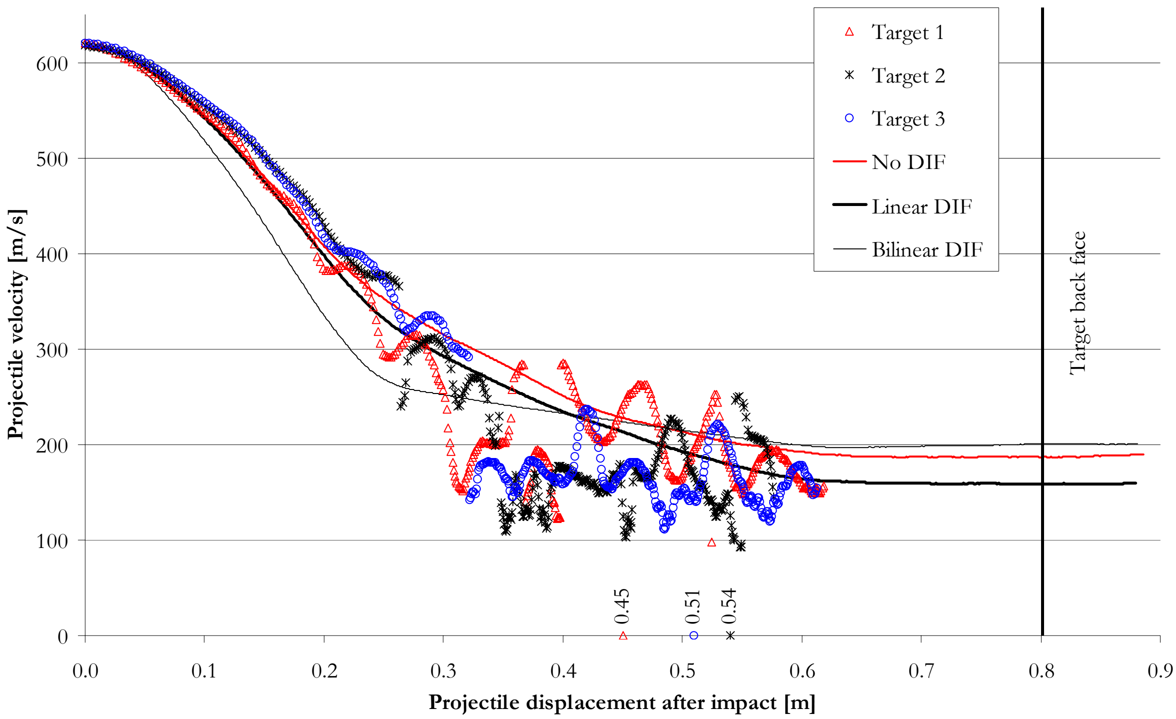

Figure 25. Comparison between numerical simulations and test data. Data points with values are depths of penetration measured after test.

Compared to data from the Doppler radar, the simulations show a higher retardation of the projectile in the beginning of the penetration phase. At a projectile displacement of about 0.25m (or 0.5ms), the retardation decreases and the decrease is more pronounced when using the bilinear DIF relation. Post-processing of the simulations shows that at this moment a plug is formed in the target, see Figure 26, due to a great amount of shear damage in the element size transition zone.

To investigate if the plug and thus the sudden decrease in retardation was caused by the models inability to handle different element sizes, i.e. different fracture energies, a new geometry model was constructed consisting of 5mm elements all through the target. Due to lack of memory, modelling of the whole target geometry could not be carried out. However, a smaller model with square geometry 330x330x800mm (1/4 model) and boundaries with fixed displacement and rotational constraints was created, see Figure 27 to Figure 28 and Appendix E for the LS-INGRID input file, with the specifications given in Table 8.

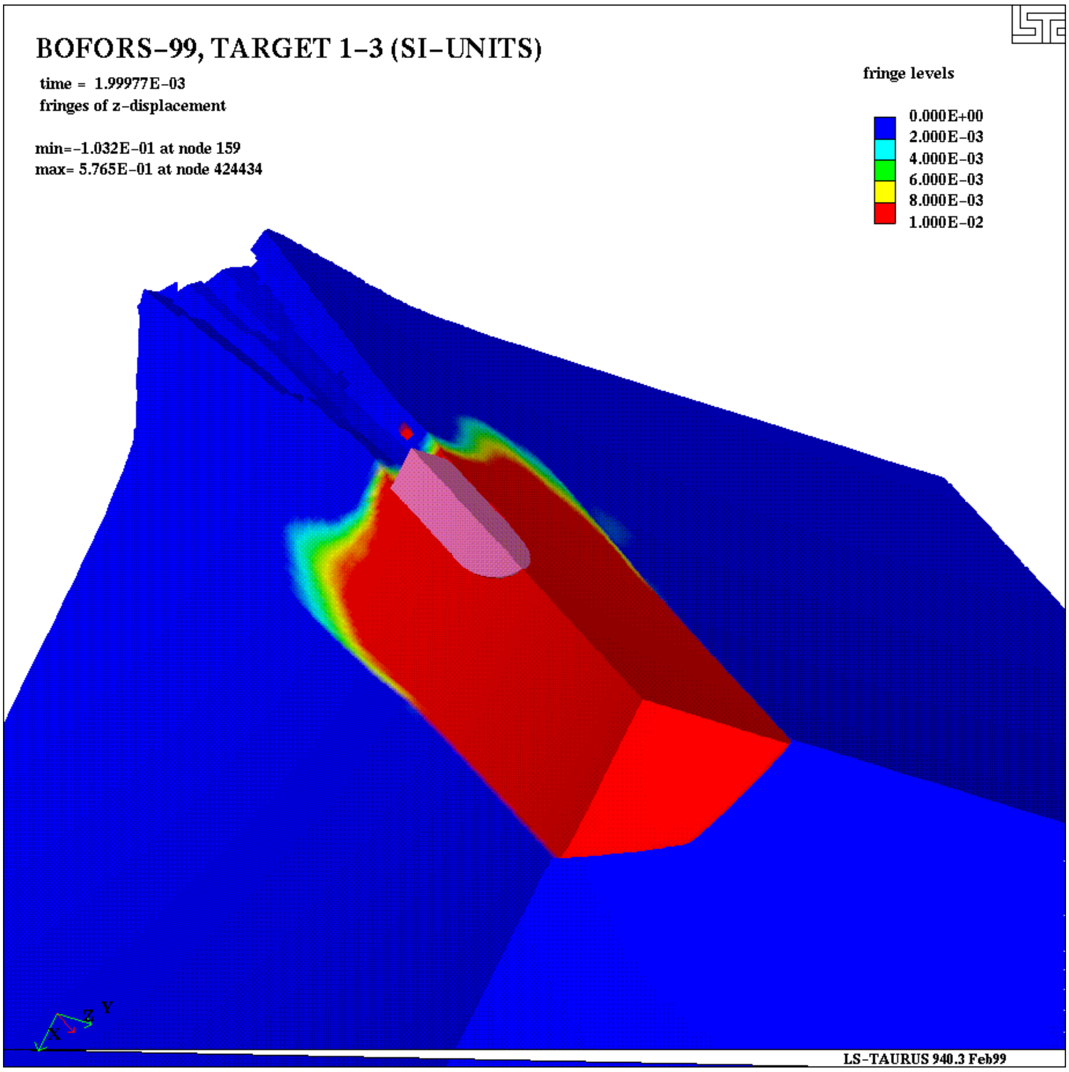

Figure 26. Formation of a plug in the target due to great amount of shear damage

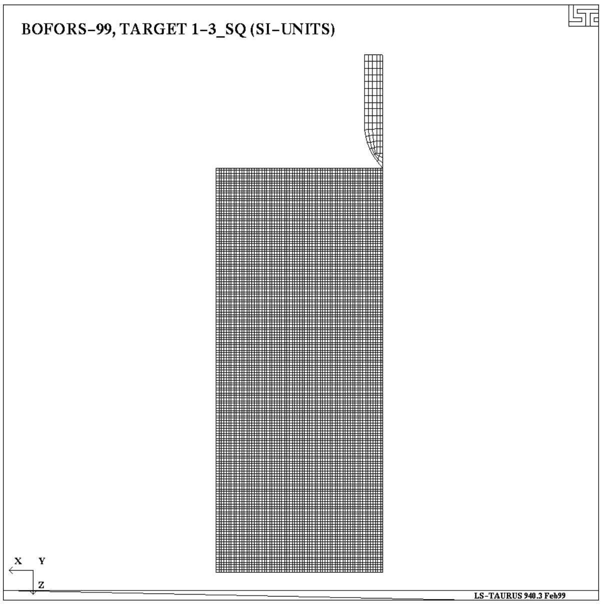

Figure 27. Mesh C in elevation view

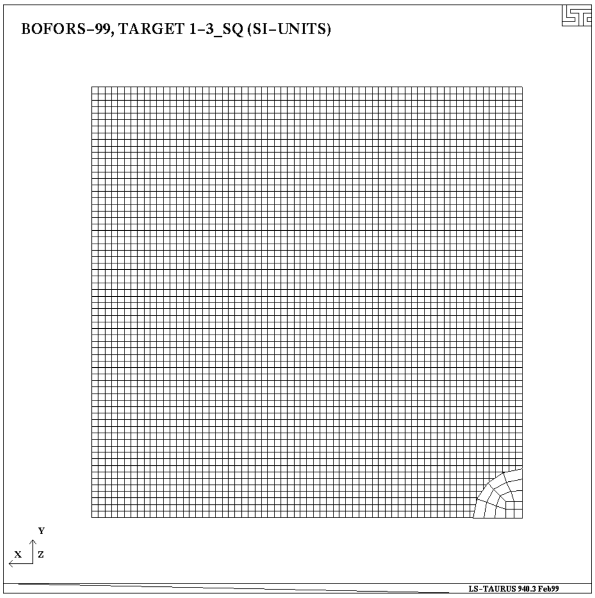

Figure 28. Mesh C in plan view

Table 8. Mesh data for square geometry target 1-3

Mesh	C
Characteristic element size	5mm
Nodes	723 125
Solid elements	697 212
Approx. CPU time	35 h

In Figure 29 and Figure 30 it is shown that when using the same element size in the whole target no plug is formed, but the sudden decrease in retardation is still there. Nevertheless, the formation of a plug leading to lower structural bearing capacity shows that there is a need to improve the model in order to make the fracture energy release objective, i.e. mesh independent. An explanation for the sudden decrease in retardation has not been found nor has it been possible to conclude that this is not a real phenomenon. But, the data from the Doppler radar and the measured penetration depths indicate that this is not the case.

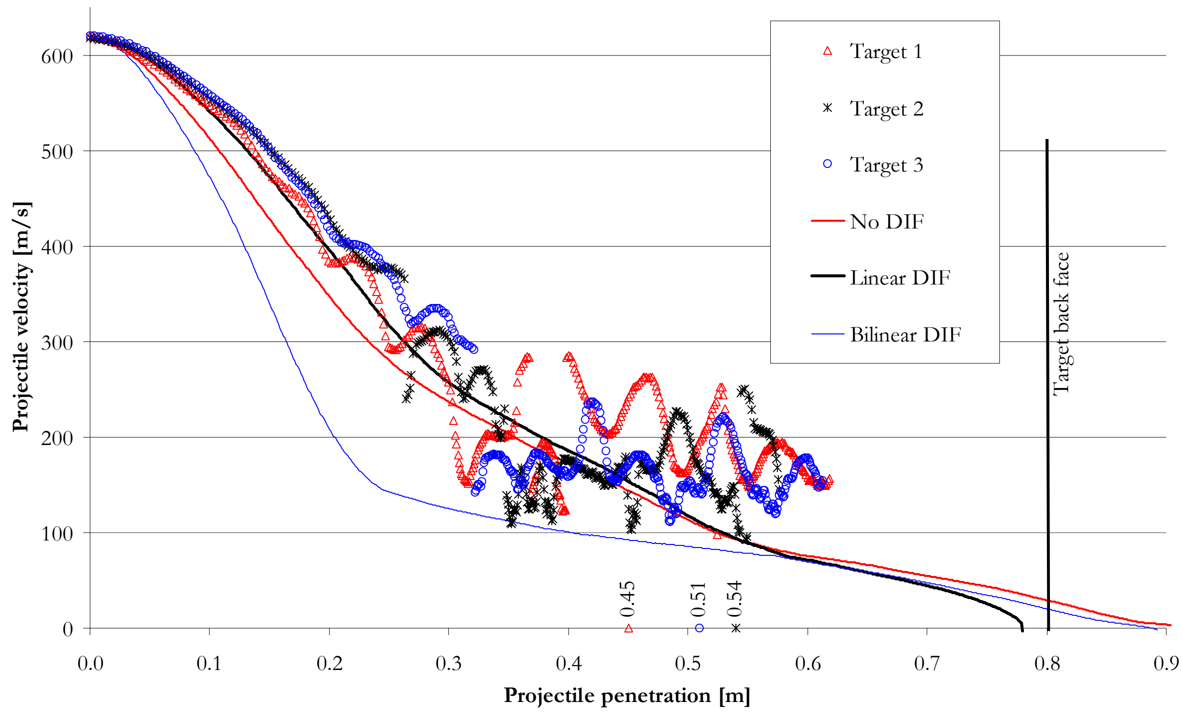

Figure 29. Comparison between numerical simulations and test data. Data points with values are depths of penetration measured after test.

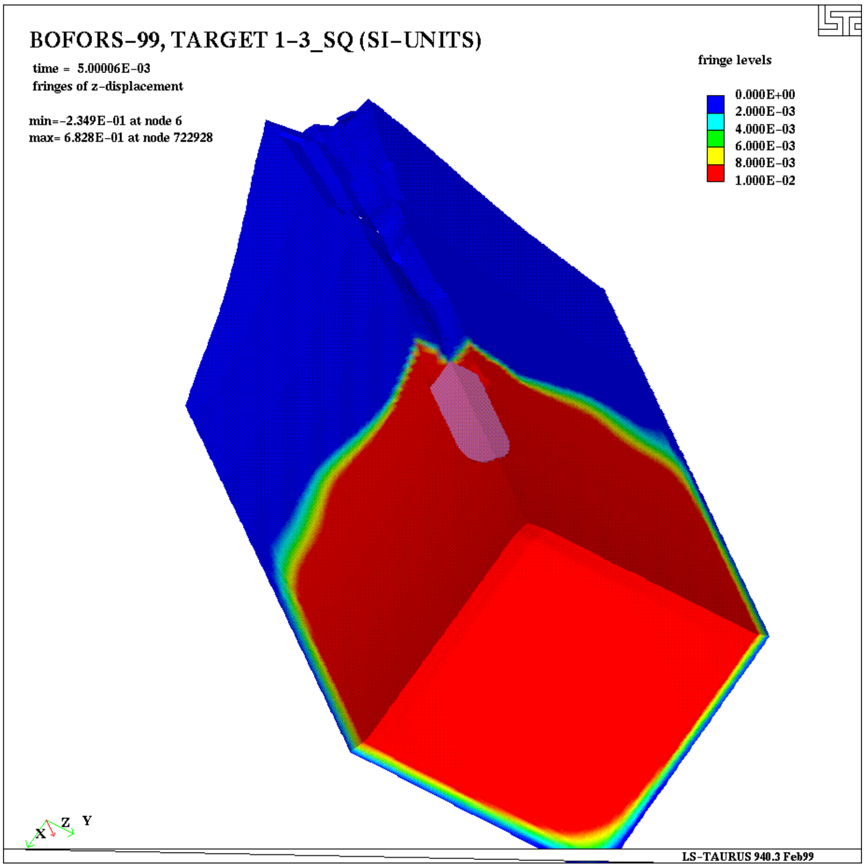

Figure 30. Longitudinal displacement for the square geometry model.

Returning now to the previous geometry model for targets 1-3, mesh A with a bilinear DIF. In Figure 31 and Figure 34 comparisons of damage are made with photos taken after the tests.

Figure 31. Post condition for the front face of target 3 (shot 6).

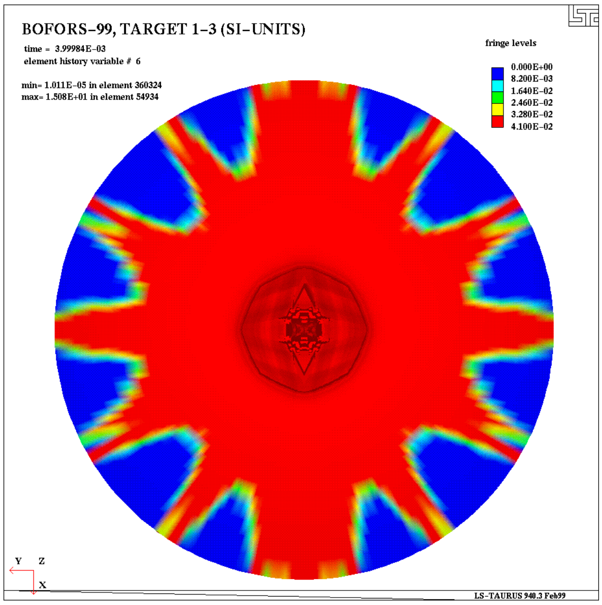

Figure 32. Damage on the front face from simulation.

Figure 33. Post condition for the back face of target 3 (shot 6).

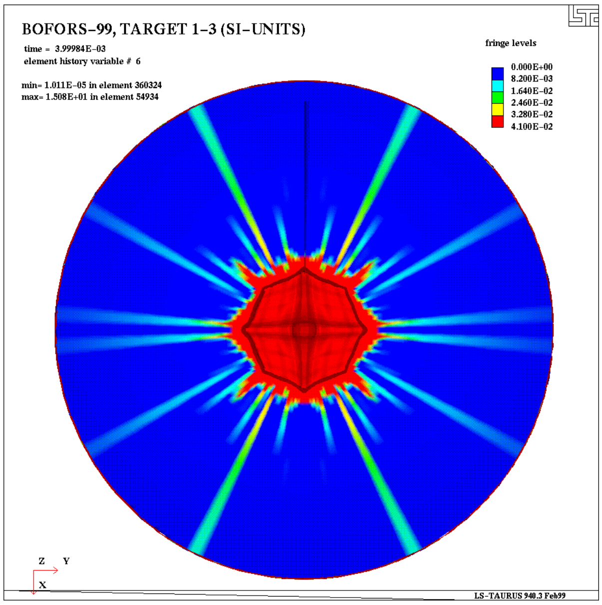

Figure 34. Damage on the back face from simulation.

In Figure 35 the damage variable lambda is plotted on the symmetry plane. According to this figure the target is almost completely damaged, which is not consistent with the test results.

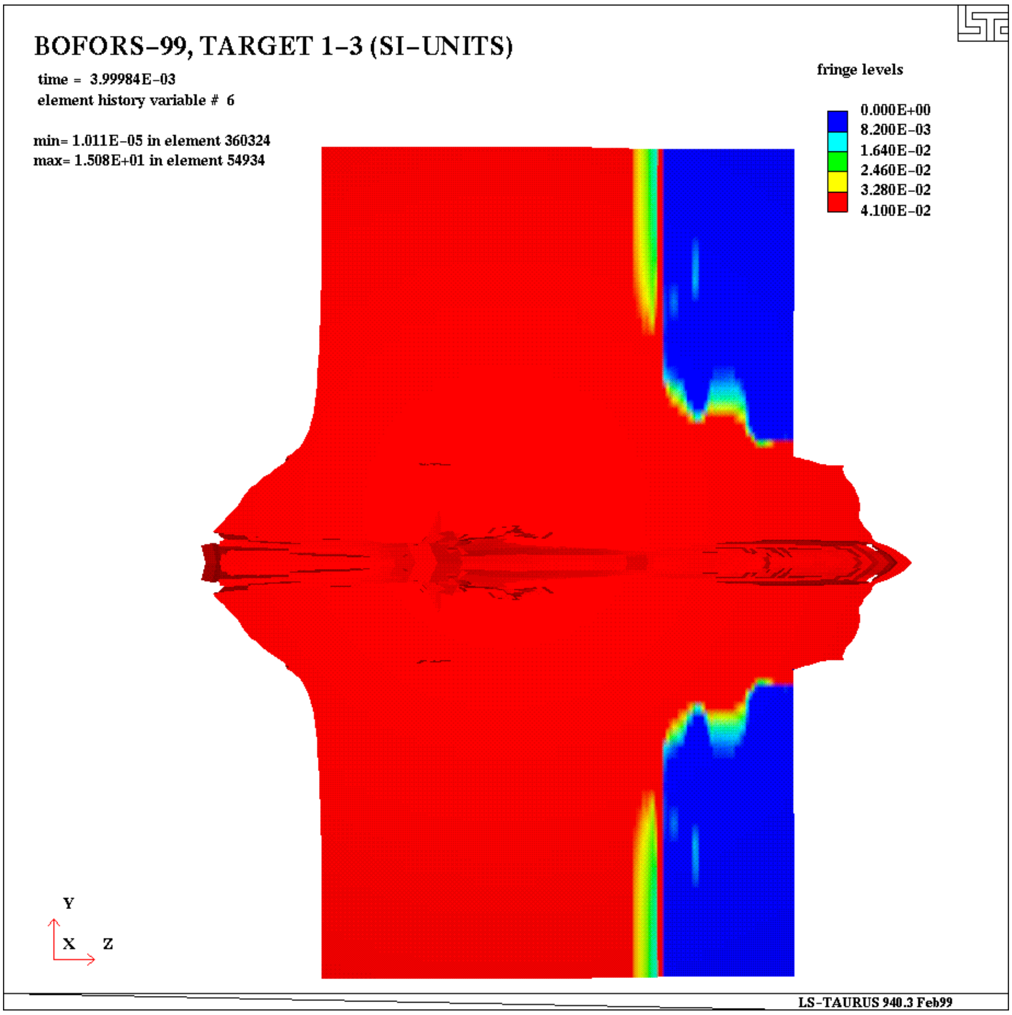

Figure 35. Damage in the target, side view.

4.2 Target 4-6

The LS-INGRID input file and changes made to the created LS-DYNA keyword format input file are found in Appendix C. The mesh used for this target is shown in Figure 36 and Figure 37 and in Table 9 mesh specifications are given.

First, the element size dependency was investigated using no DIF relationship. The results are presented in Figure 38 where it is obvious that the fracture energy release is not objective, i.e. adjusting the parameters b1, b2, and b3 does not eliminate mesh dependency. The elements outside the impacting area that are bigger than 5mm and 7.5mm respectively might also influence the result. For larger elements, the energy release is lower giving a higher residual velocity. This is consistent with the observed results. For erosion shear strain values over 0.9 the mesh becomes heavily distorted, why this value is taken as maximum.

The influence of dynamic friction (no DIF) was also investigated, see Figure 39. Obviously, the friction has none or little effect on the result. This is due to the small area of contact between the projectile and the target, see Figure 40. At the nose, the elements are deleted according to the erosion criteria and towards the rear of the projectile, the hole in the target has a conical shape leaving a void between the projectile and the target.

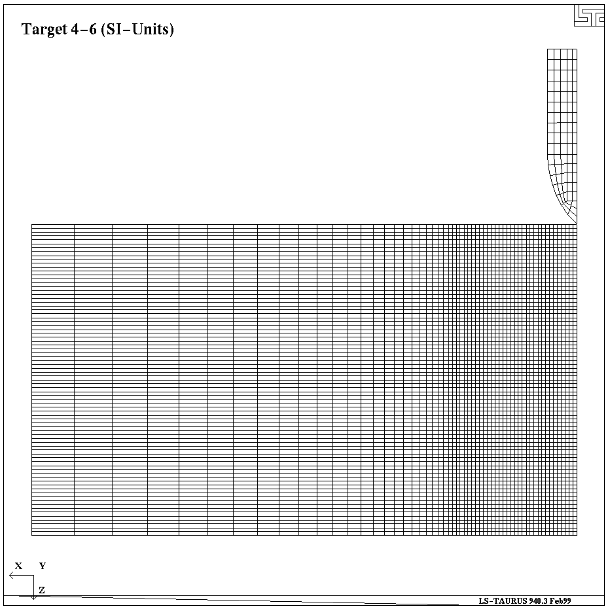

Figure 36. Mesh A in elevation view.

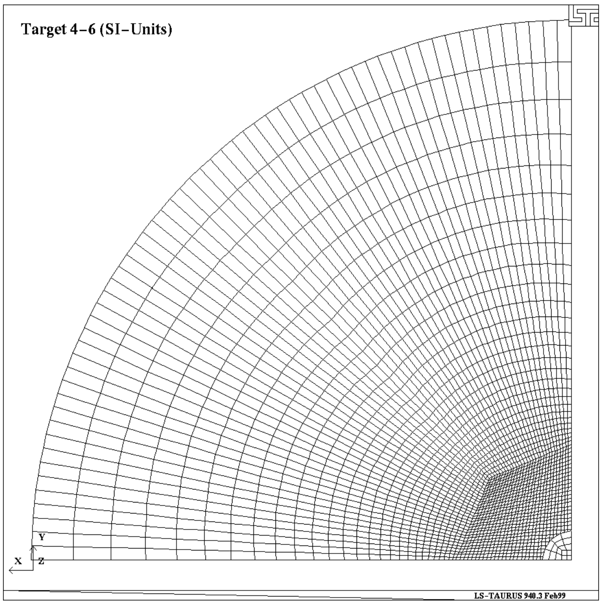

Figure 37. Mesh A in plan view.

Table 9. Mesh data for targets 4-6.

Mesh	A	B
Characteristic element size	5mm	7.5mm
Nodes	211 160	51 212
Solid elements	201 600	47 488
Approx. CPU time	3 hours	1 hour

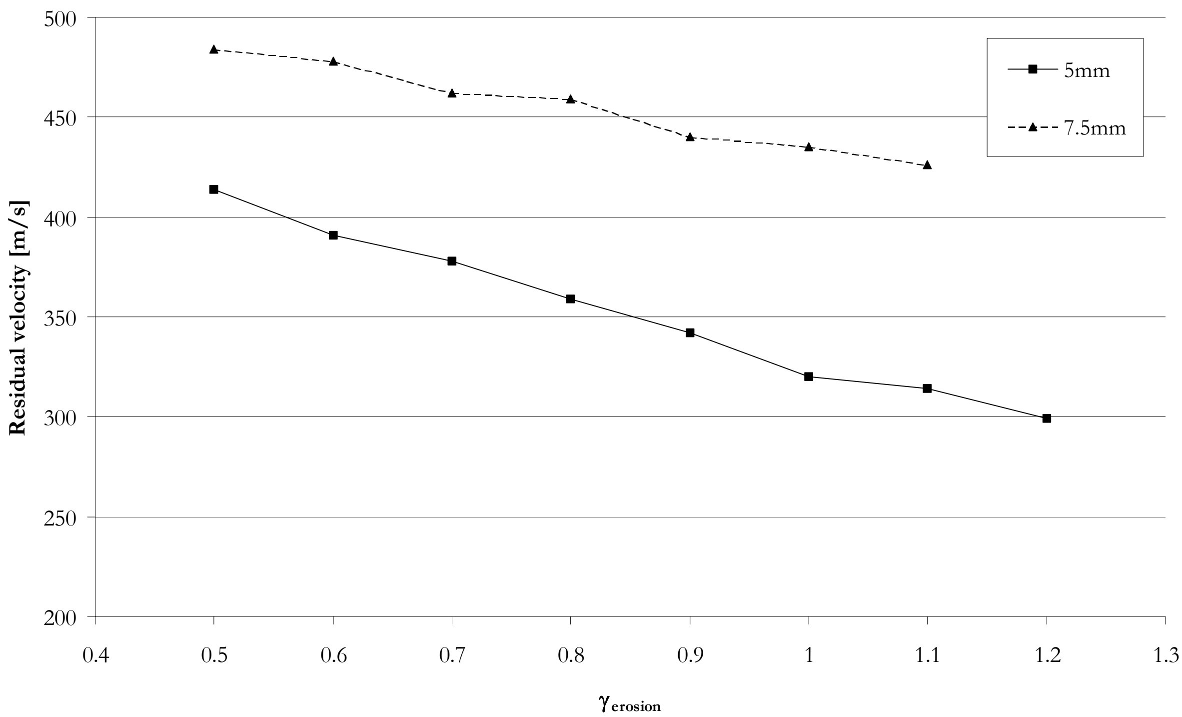

Figure 38. Influence of mesh element size and erosion shear strain on residual velocity (no DIF).

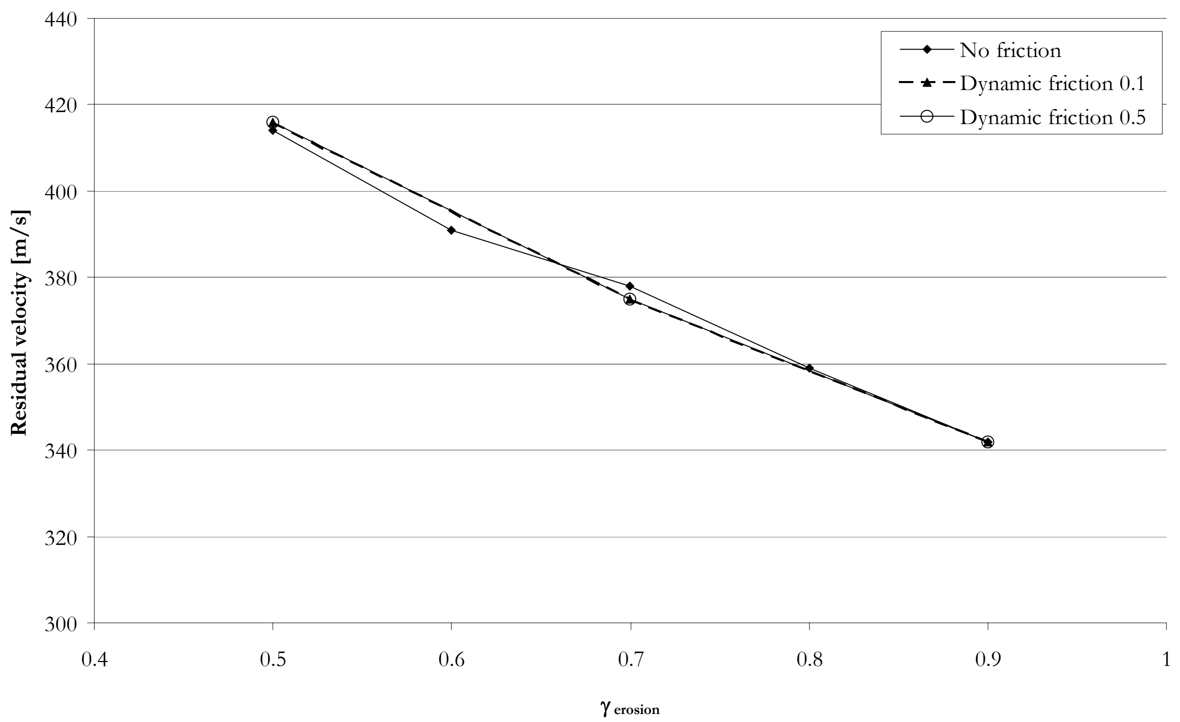

Figure 39. Influence of dynamic friction on residual velocity (no DIF).

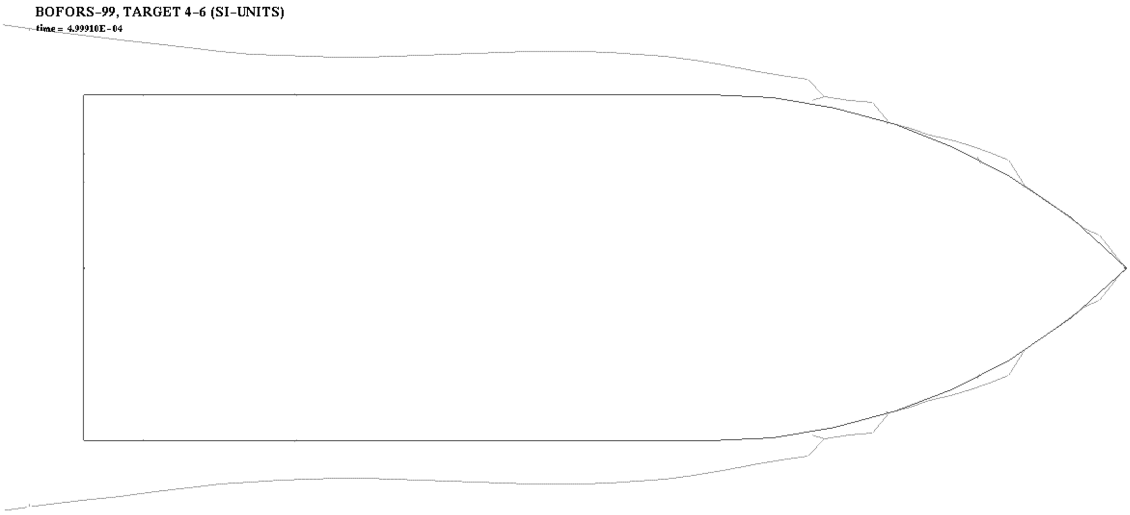

Figure 40. Contact between projectile and target

The strain rate dependency was investigated using two curves, see Figure 41, for dynamic increase of the target's compressive strength. The computations were carried out with an erosion shear strain of 0.9.

Integrating the Doppler radar curve and plotting it against the projectile velocity show the projectile trajectory through the target, see Figure 42.

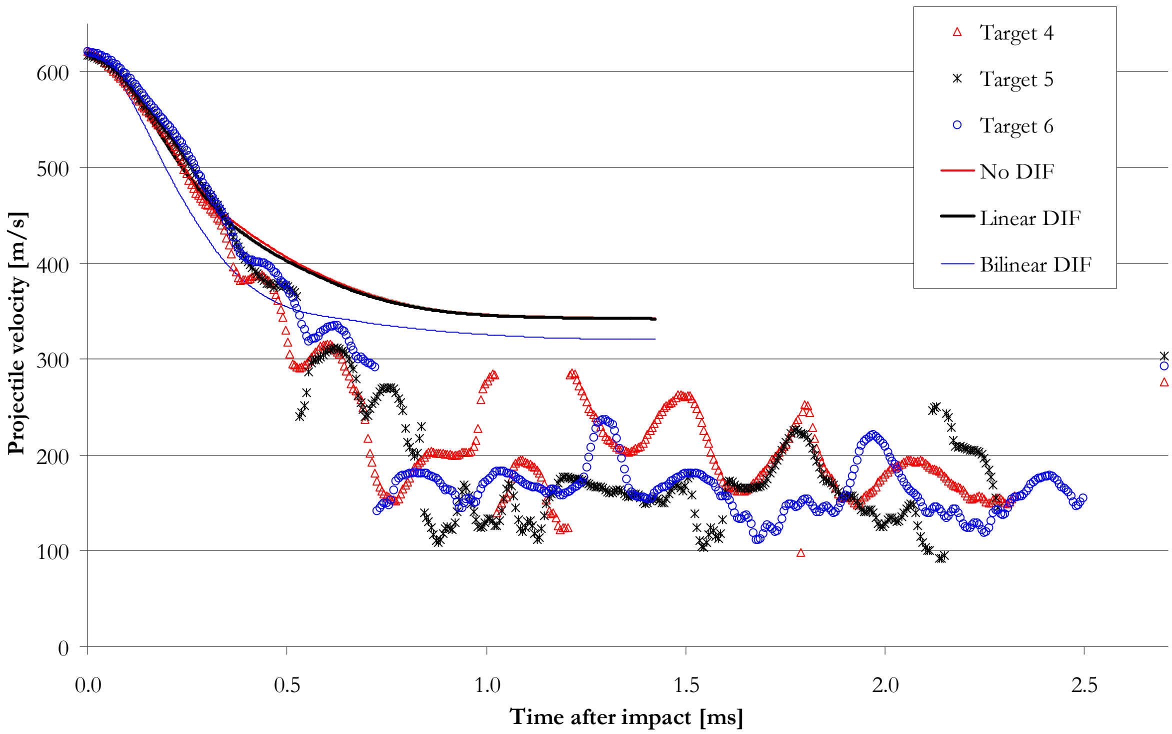

Figure 41. Comparison between numerical simulations and test data.

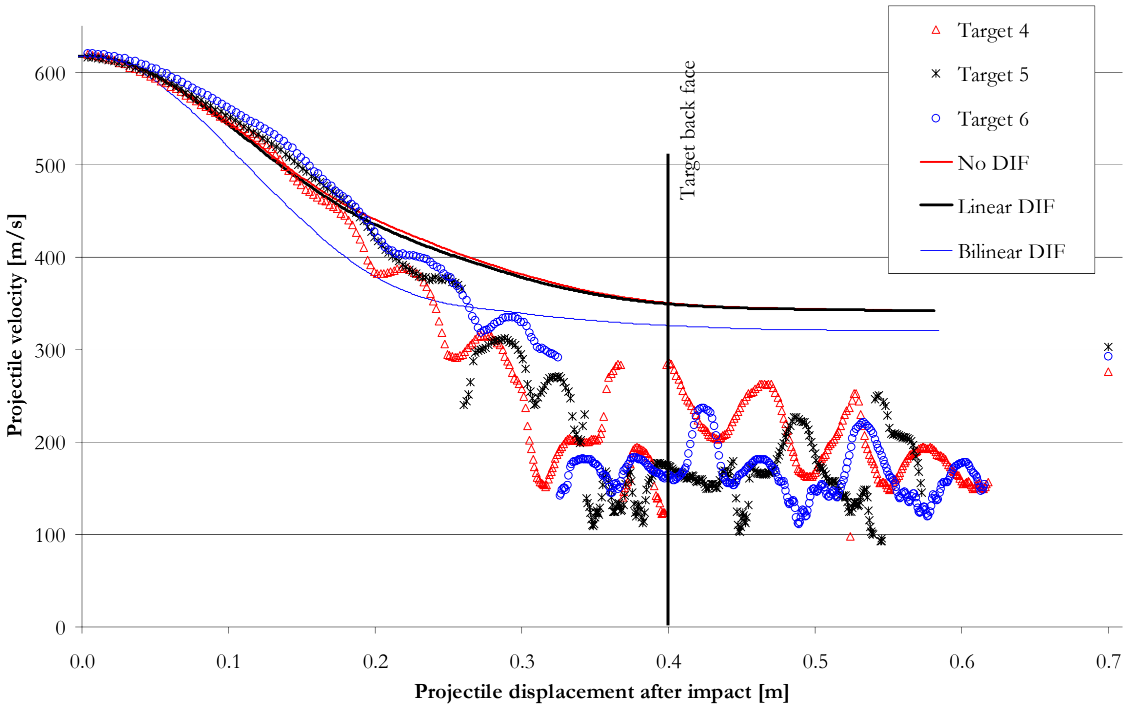

Figure 42. Comparison between numerical simulations and test data. Data points with values are taken from high-speed videos.

In this simulation, as for targets 1-3, a plug is formed in the transition zone between different element sizes, decreasing the structural bearing capacity, see Figure 43. However, the effect of this phenomenon seems less important because of the smooth retardation.

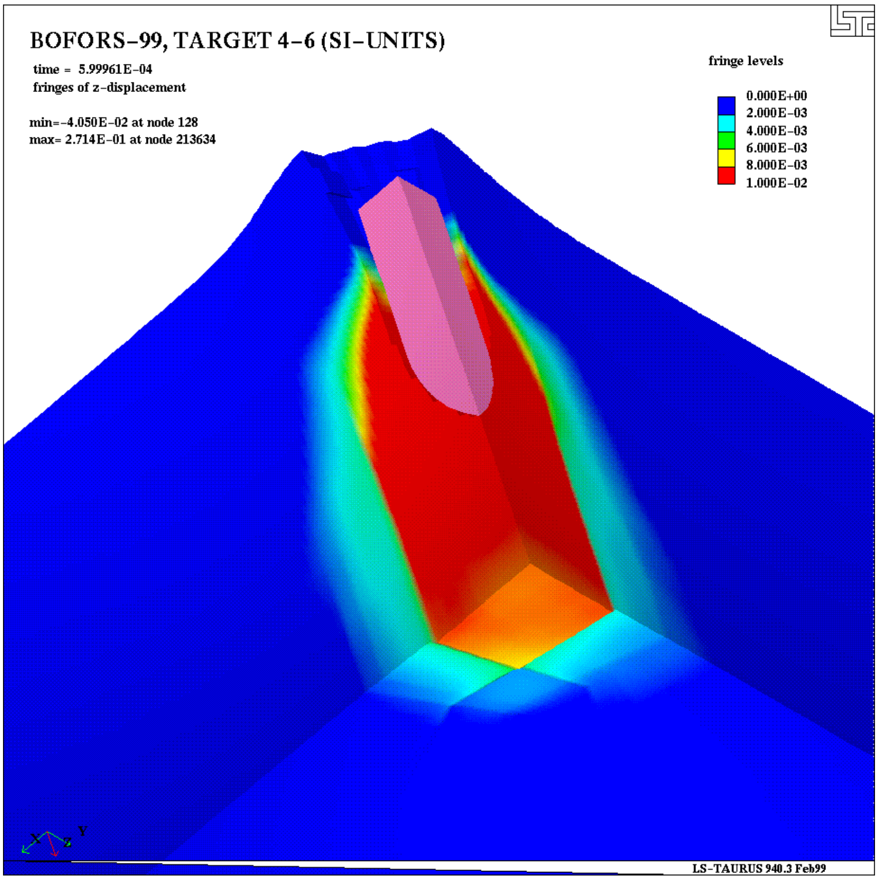

Figure 43. Longitudinal displacement for target 4-6, element size 5mm and no DIF.

Comparisons of photos from the tests with plots of the damage parameter lambda from the simulation (bilinear DIF), see Figure 44 to Figure 47, reveal almost the same damage pattern as for target 1-3.

Figure 44. Post condition for the front face of target 5 (shot 2).

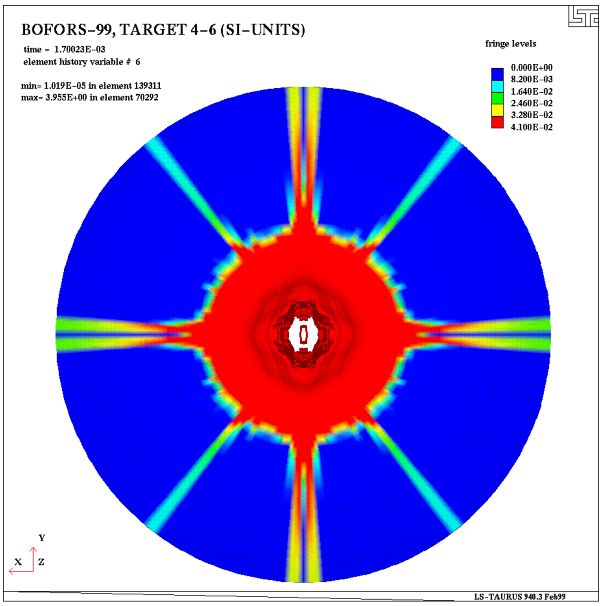

Figure 45. Damage on the front face from simulation.

Figure 46. Post condition for the back face of target 5 (shot 2).

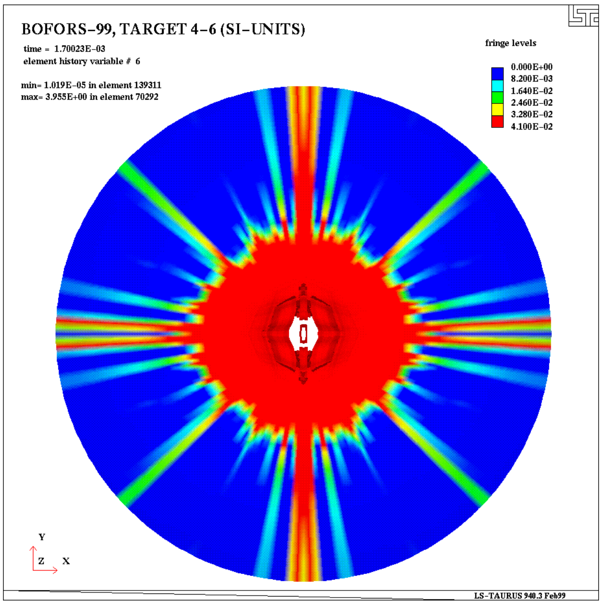

Figure 47. Damage on the back face from simulation.

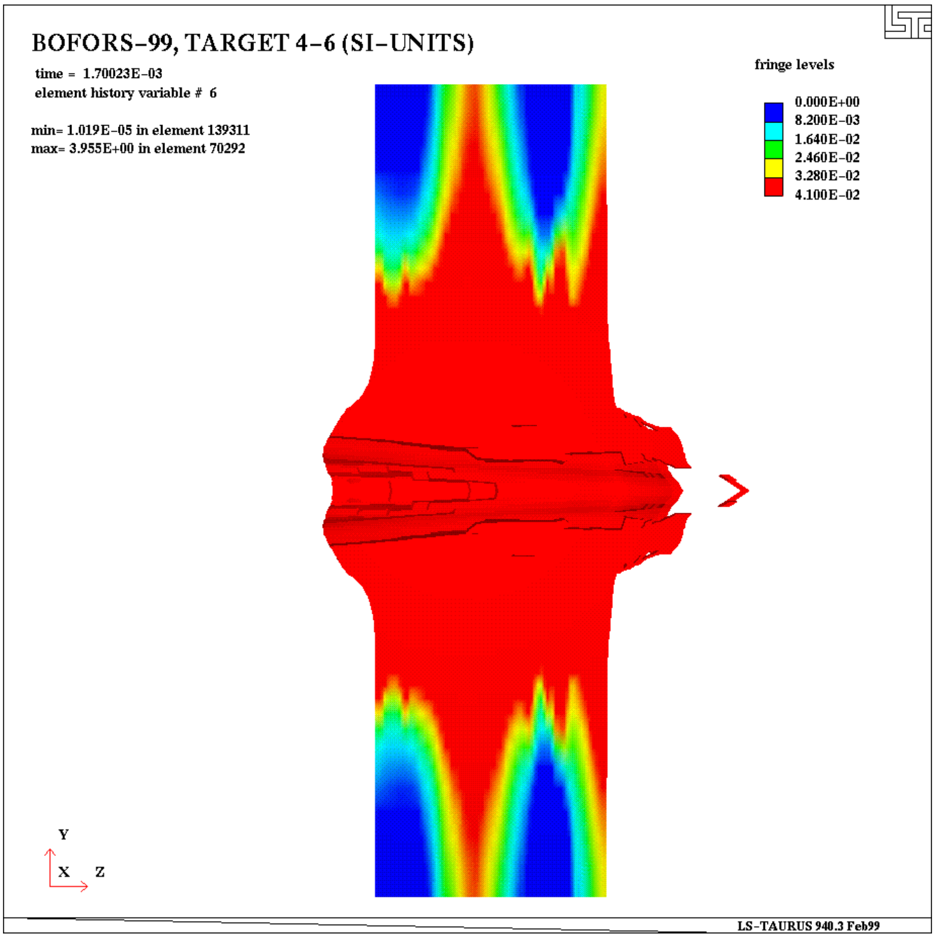

Figure 48. Damage in the target, side view.

4.3 Target 7-9

The LS-INGRID input file and changes made to the created LS-DYNA keyword format input file are found in Appendix C. Due to difficulties with connecting the reinforcement to the target mesh these tests were modelled using a square geometry, see Figure 49 to Figure 52. The reinforcement was modelled using truss elements and the nodes were tied to the corresponding nodes for the target brick elements. In Table 10 mesh specifications are given.

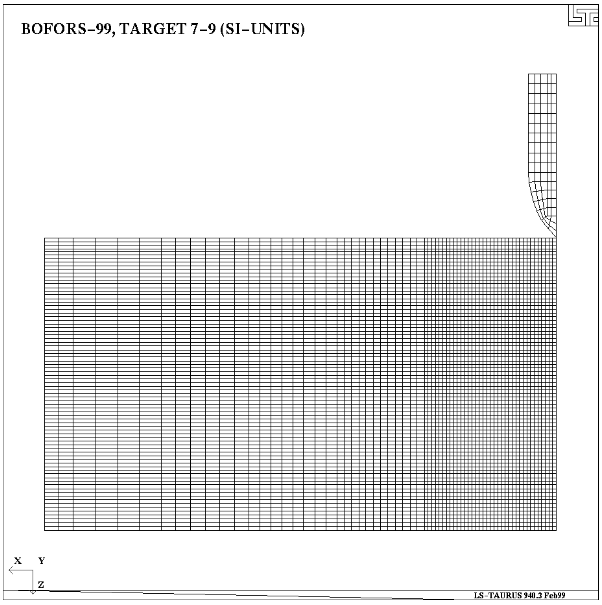

Figure 49. Mesh A in elevation view.

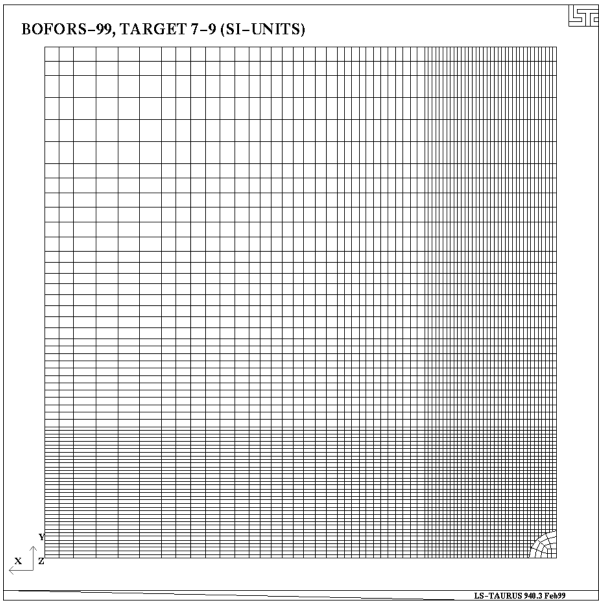

Figure 50. Mesh A in plan view.

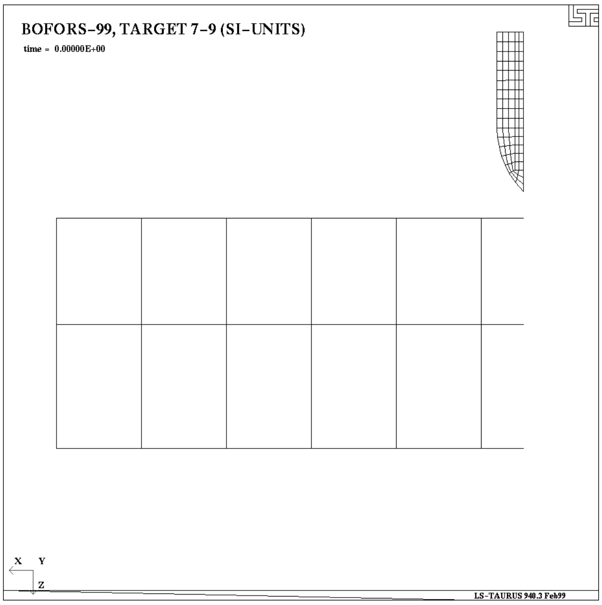

Figure 51. Elevation view of reinforcement cage.

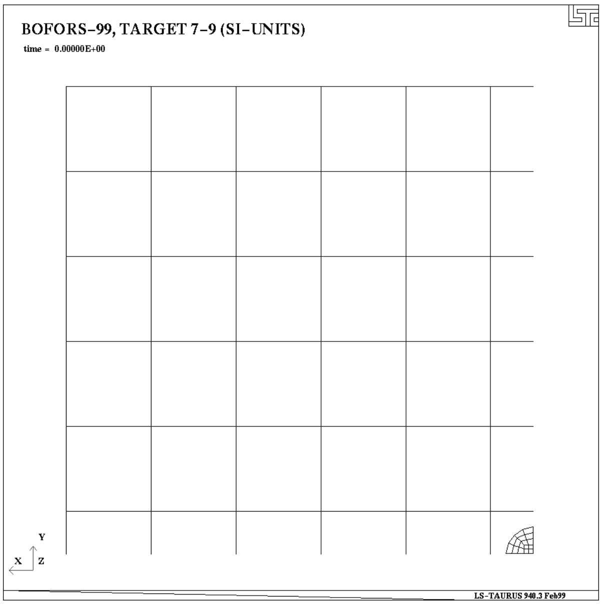

Figure 52. Plan view of reinforcement cage.

Table 10. Mesh data for targets 7-9.

Mesh	A
Characteristic element size	5mm
Nodes	392 792
Solid elements	369 920
Truss elements	7 092
Approx. CPU time	7 h

The strain rate dependency was investigated with an erosion shear strain of 0.9. Integrating the curves in Figure 53 and plotting it against the projectile velocity show the projectile trajectory through the target, see Figure 54. In Figure 55, a damage plot is given showing the formation of a plug .

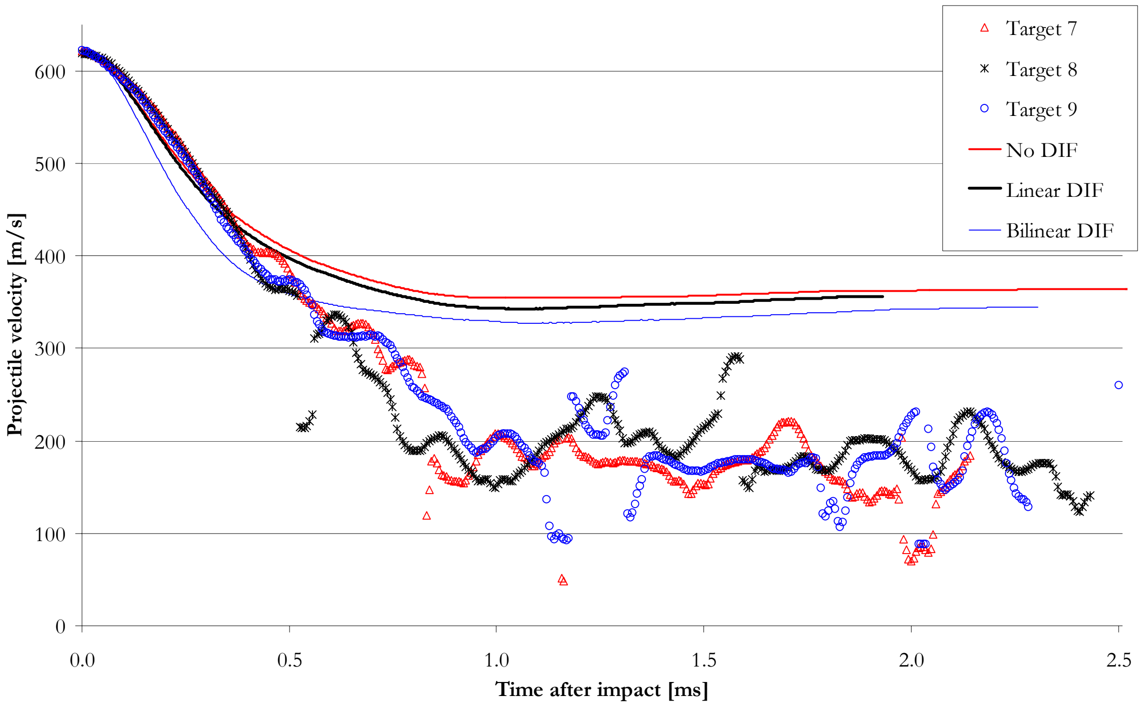

Figure 53. Influence of dynamic increase factor (DIF) on projectile retardation.

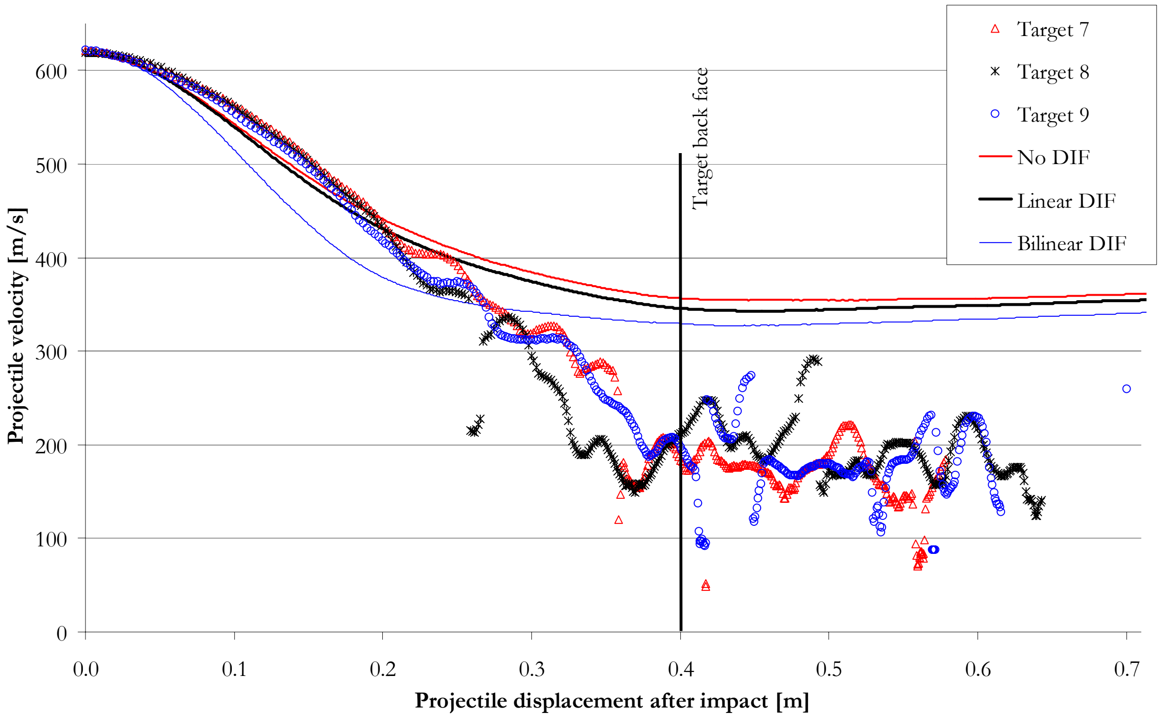

Figure 54. Influence of dynamic increase factor (DIF) on projectile retardation.

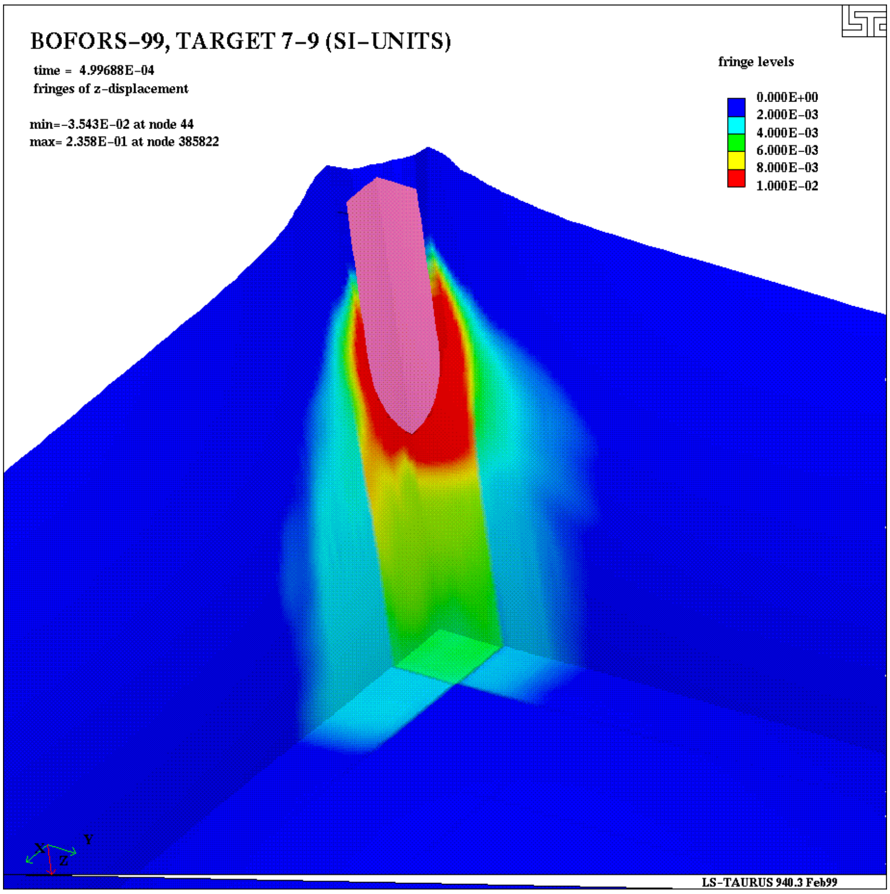

Figure 55. Longitudinal displacement for target 7-9, element size 5mm and no DIF.

In Figure 56 to Figure 59 comparisons of the damage parameter lambda are made with photos taken after the tests. In Figure 61 to Figure 62 a comparison is made for reinforcement displacement at the target back face after perforation.

Figure 56. Post condition for the front face of target 7 (shot 7).

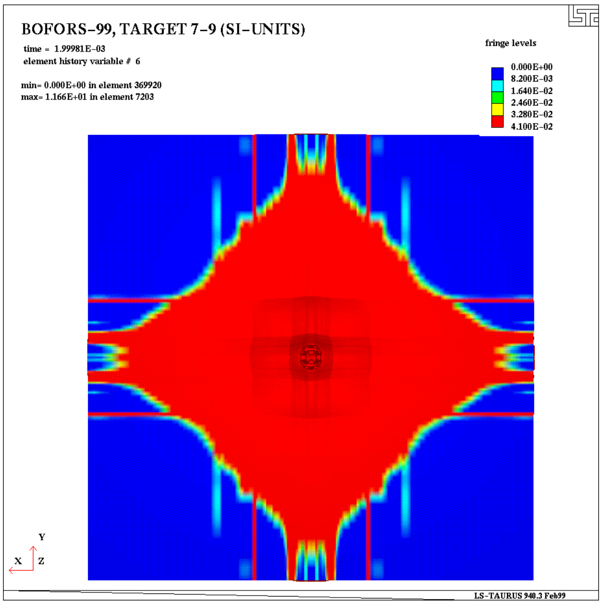

Figure 57. Damage on the front face from simulation (bilinear DIF).

Figure 58. Post condition for the back face of target 9 (shot 9).

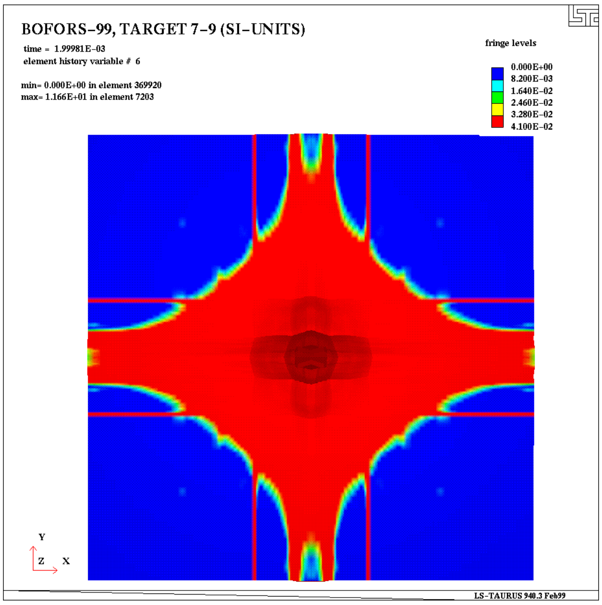

Figure 59. Damage on the back face from simulation (bilinear DIF).

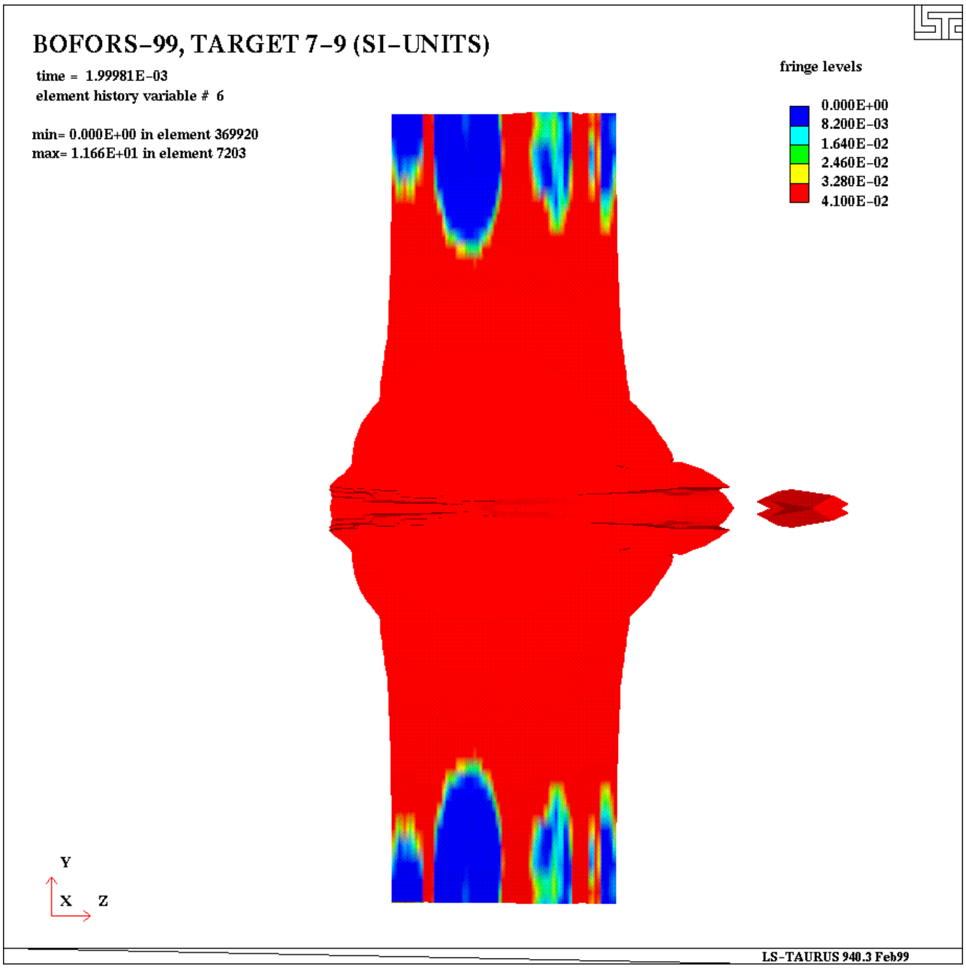

Figure 60. Damage in the target, side view (bilinear DIF).

Figure 61. Post condition for the reinforcement at back face of target 7 (shot 7).

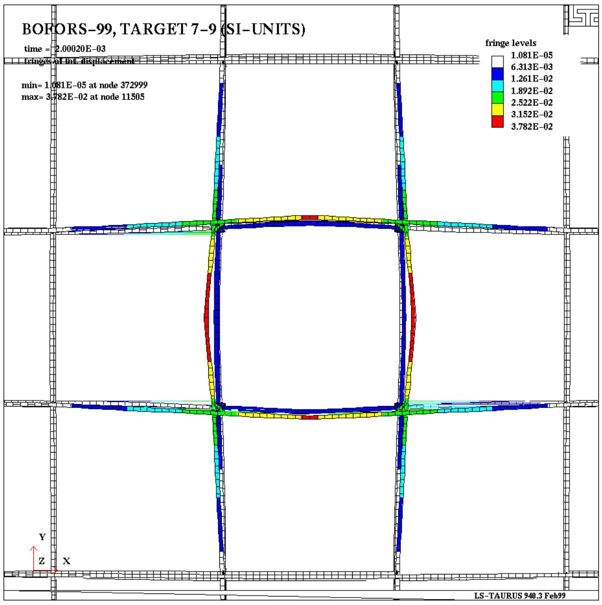

Figure 62. Post condition for the reinforcement at back face of target from simulation.

5 SUMMARY

Numerical simulations of penetration and perforation tests of high strength concrete have been carried out. The structural systems were modelled in LS-DYNA and solved using Lagrangian technique. Influence of strength enhancement based on strain rate, numerical erosion criteria, friction between target and projectile and mesh dependency has been investigated.

Results from the computations were compared to test data on the projectile trajectory and photos showing the damaged targets. For perforation, the projectile's trajectory was derived from Doppler radar and high-speed photos. In the case of penetration, the projectile's trajectory was derived from Doppler radar and measurements on depth of penetration.

The simulations show good agreement with test data for perforation. For penetration, the results are not satisfying since in the simulations the projectile perforates the target, which was not the case for the tests, see Table 11.

Table 11. Comparison of results from test and numerical simulations.

		Test		Numerical simulation	
Target number	Projectile impact velocity [m/s]	Depth of penetration [mm]	Projectile residual velocity [m/s]	Depth of penetration [mm]	Projectile residual velocity [m/s]
1-3	616	500	-	-	200
4-6	617	-	291	-	320
7-9	616	-	260	-	330

During the work with the simulations, problems have been encountered in the following areas.

- Material type 72

The target material model does not allow different element sizes to be used in one material definition. The damage curve is fitted to one specific element size and when using different sizes of elements, one does not get the correct energy release. Future improvements of the model should include regularisation of the fracture so that the fracture energy release becomes objective, i.e. mesh independent. This problem with the fracture energy release seems to be a possible explanation for the large amount of shear damage in the element transition zones. The authors of the material model have improved the model since the first release, which is the one implemented in LS-DYNA. In Appendix B improvements made in the more recent release II of the model are listed.

- Numerical erosion

In LS-DYNA, six different types of erosion criteria can be used, with all material types and one-point integrated solid elements. The value on the erosion criteria has a great influence on the results but the determination of the erosion criteria parameters is difficult, as the mesh becomes much distorted at large values. This problem suggests that another solution technique should be used, for example using an Euler reference frame or a smooth particle hydrodynamic (SPH) approach. A new erosion criterion should also be added to this particular material type, based on the modified effective plastic strain parameter lambda. This would give the possibility to ensure that all fracture energy has been released before eroding, or deleting, the element.

- Interaction between concrete and reinforcement

With concrete to reinforcement mass ratio of 6%, one cannot use a smeared approach to model the rebars and stirrups. In this report, truss-elements were used, but this is not sufficient to take into account the confinement contributed by the reinforcement. The rebars should be modelled either as solid elements with a concrete-rebar interface or beam elements with and a slip model. For beam elements there is a possibility to model slip in LS-DYNA with an option called 1-D slide line, which have not been applied to this problem.

- Dynamic increase factor (DIF)

When enhancing the material strength using a DIF relation the structural response changes in the beginning of the penetration phase, i.e. the retardation of the projectile increases. However, for all cases considered here this effect seems to last only to half the targets depth and we almost got a converging residual velocity for all three DIF relations. For targets 1-3, where the projectile should come to rest in the target according to the test, a extrapolation of the initial retardation phase points to the measured depths of penetration. An explanation for what causes the pronounced bend on the projectiles penetration path, see for example Figure 25, has not been found in this report.

REFERENCES

1. LSTC (1999). *LS-DYNA keyword user's manual, non-linear dynamic analysis of structures, version 950*. Livermore Software Technology Corporation, LSTC report.
2. Malvar L J, Crawford J E, Wesevich J W, Simons D: *A Plasticity Concrete Material Model for Hydrocodes*. International Journal of Impact Engineering, Vol. 19, Nos. 9-10, pp 847-873. Elsevier Science Ltd. 1997.
3. LSTC (1990). *LS-TAURUS: An interactive post-processor for the analysis codes LS-NIKE3D, LS-DYNA3D and TOPAZ3D*. Livermore Software Technology Corporation.
4. AB Svensk Byggtjänst (1997): *Betonghandboken Material, utgåva 2*. ISBN 91-7332-799-9.
5. CEB (1993): *CEB-FIP Model Code 1990, Design Code*. ISBN 0-7277-1696-4. Thomas Telford publishing.
6. LSTC (1998). *LS-INGRID: A pre-processor and three-dimensional mesh generator for the programs LS-DYNA, LS-NIKE3D and TOPAZ3D, version 3.5*. Livermore Software Technology Corporation, LSTC report.
7. O'Carroll, Cathy (1999): Advances for modelling of geological materials. *Material Test Procedures in Support of Dynamic Material Modelling*. Defence Research Establishment, Report FOA-R- -99-01227-311- -SE. ISSN 1104-9154.

APPENDICES

Appendix A

The following plots show the frequency intensity from the Doppler radar and a predicted projectile path. For each target two plots are presented, the first showing all data and the second only for the penetration phase.

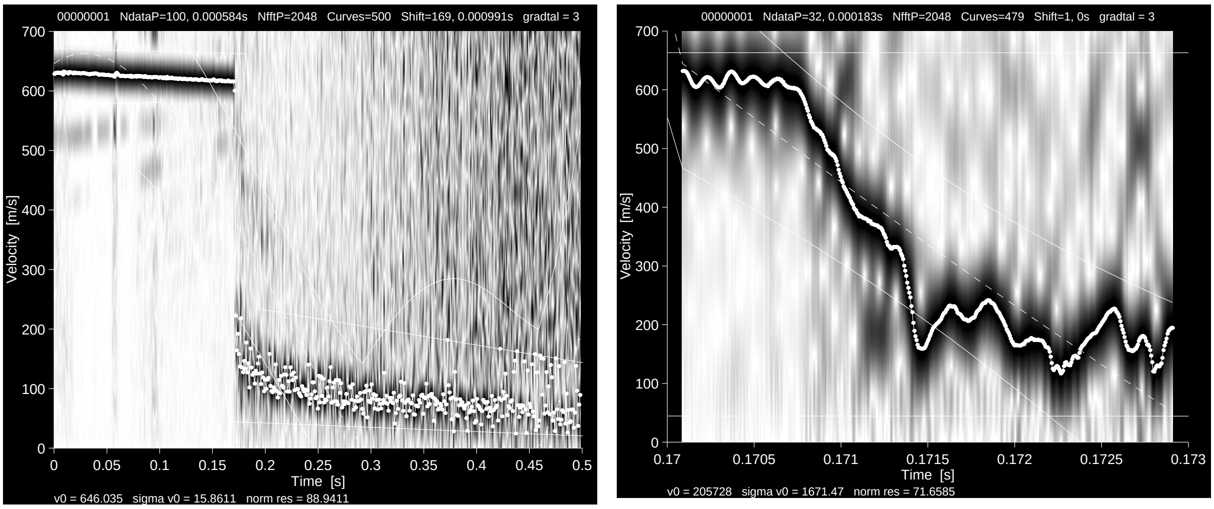

Figure 63. Doppler radar data for target 1

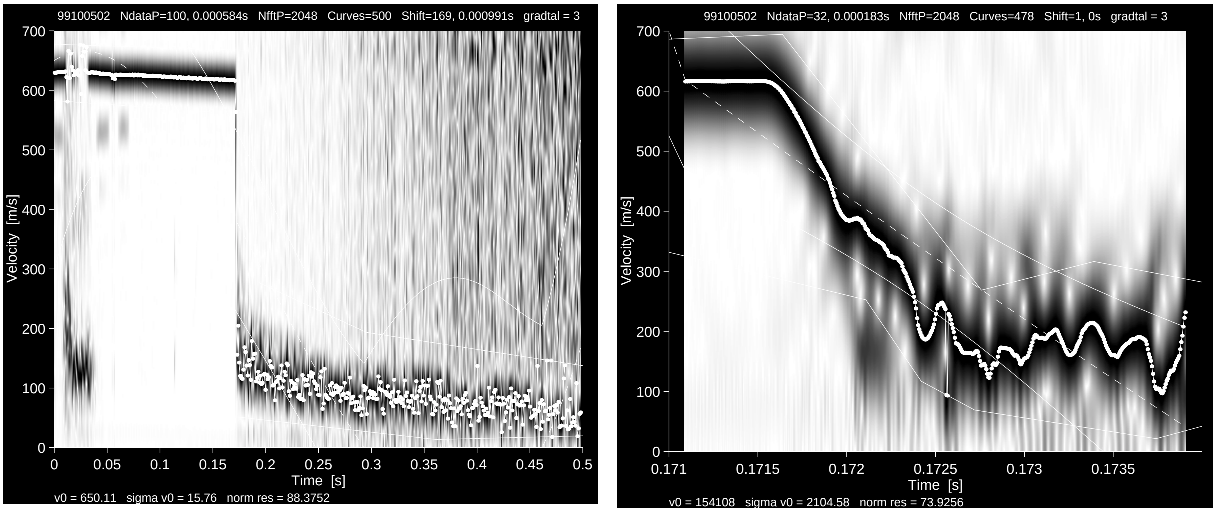

Figure 64. Doppler radar data for target 2

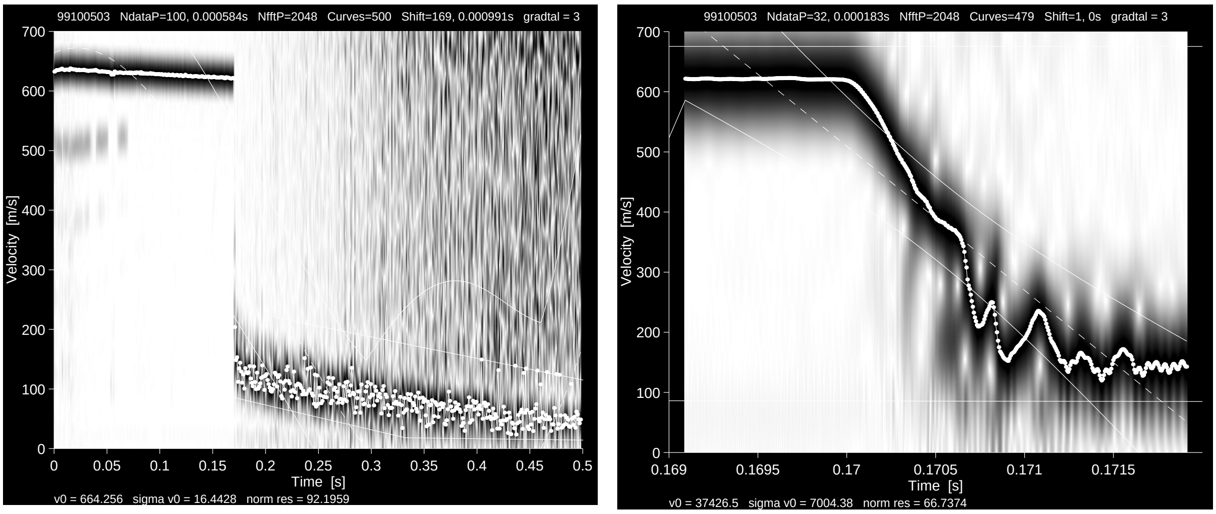

Figure 65. Doppler radar data for target 3

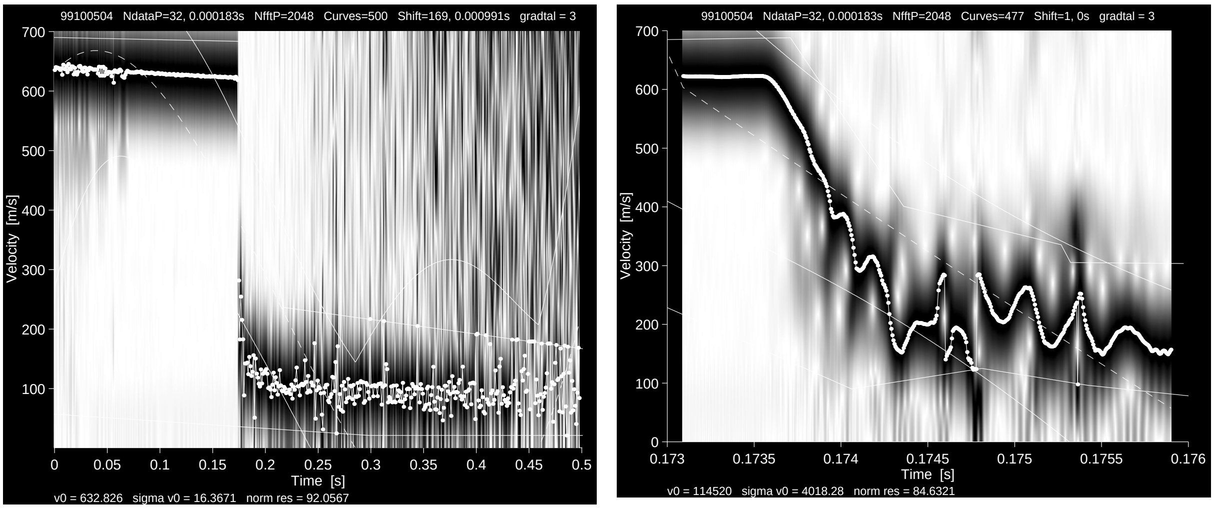

Figure 66. Doppler radar data for target 4

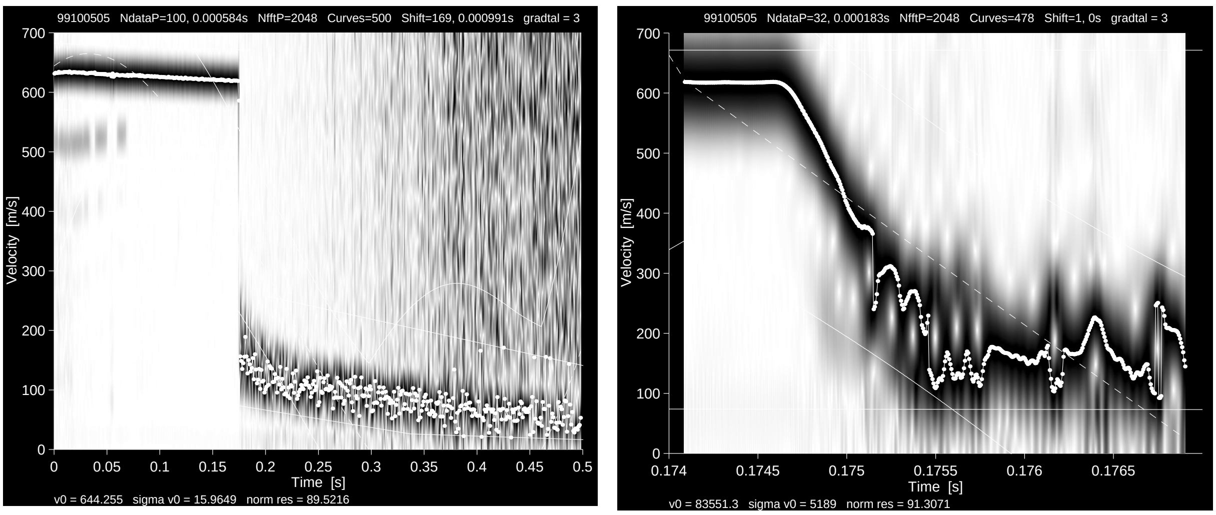

Figure 67. Doppler radar data for target 5

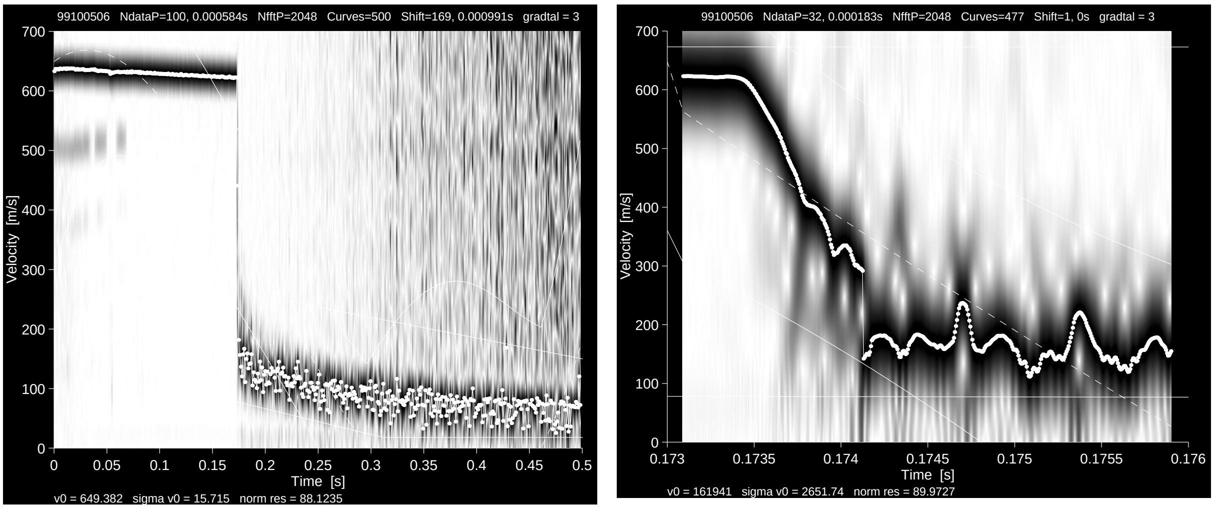

Figure 68. Doppler radar data for target 6

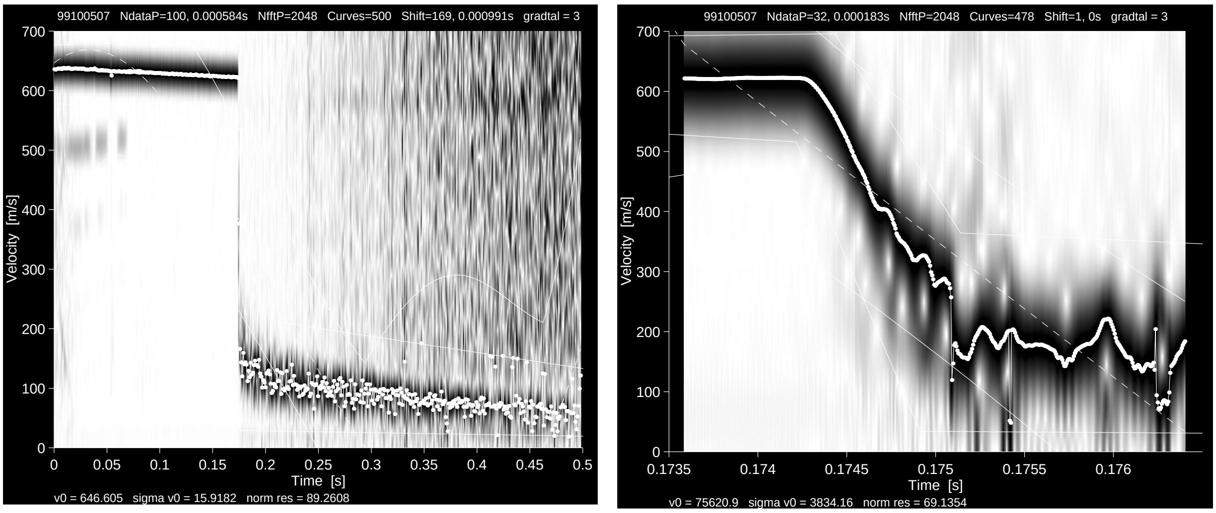

Figure 69. Doppler radar data for target 7

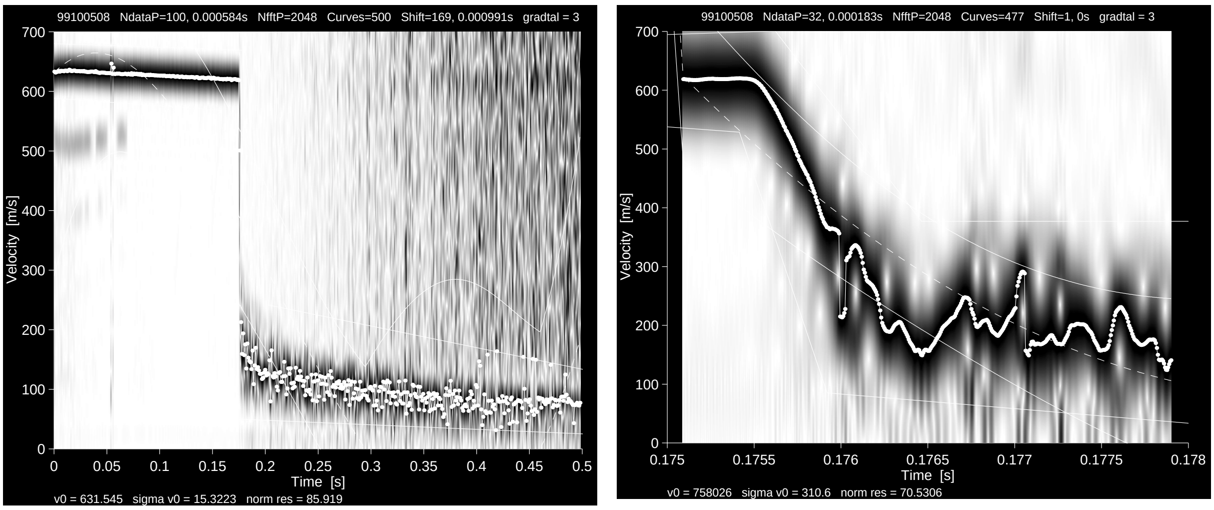

Figure 70. Doppler radar data for target 8

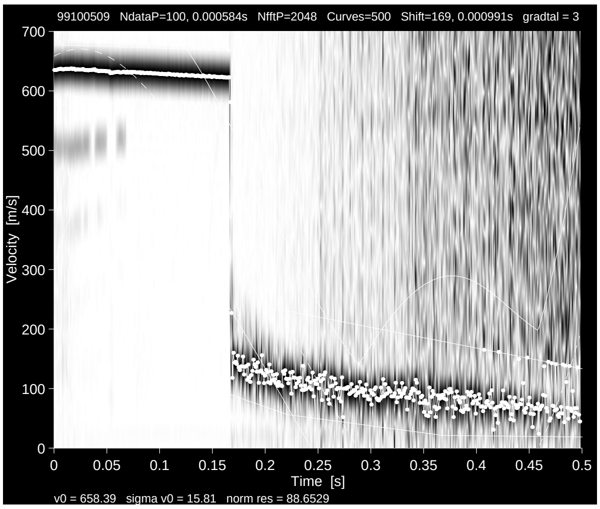

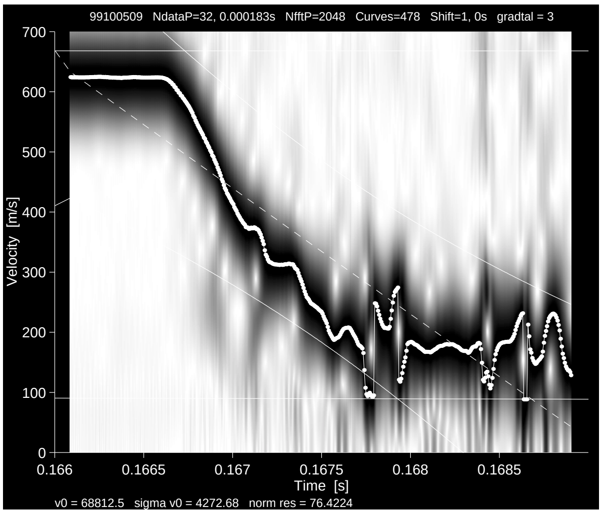

Figure 71. Doppler radar data for target 9

Appendix B

Starting from the material model ”Pseudo Tensor” (LS-DYNA material type 16), as a basis Karagozian & Case in 1994 released a constitutive concrete model for the Defence Nuclear Agency (DNA) Conventional Weapons Effects program. This model is part of the LS-DYNA standard material library since 1996 (version 940), where it is referred to as material type 72 ”Concrete Damage”. This version of the material model is called release I.

Strength surfaces

The strength surfaces limit the deviatoric stress at the corresponding pressure and in the model the construction of the strength surface in stress space is based on:

- User input of the uniaxial tensile strength

- User input of a curve for the compression meridian valid for pressures above one third of the uniaxial compression strength, i.e. including the unconfined uniaxial compression test.

$$\Delta\sigma = \sqrt{3J_2} = a_0 + \frac{p}{a_1 + a_2 p}$$

- the assumption that the tri-axial tensile strength is equal to the uniaxial tensile strength

- the assumption (based on studies of experimental data) that the bi-axial compressive strength is equal to 1.15 times the uniaxial compressive strength

- the assumption (based on studies of experimental data) that the ratio between the compressive and extension meridian at a pressure of three times the uniaxial compressive strength is 0.753.

- the assumption (based on studies of experimental data) that the ratio between the compressive and extension meridian at pressures higher than 8.45 times the uniaxial compressive strength is 1.

- the 3D-shape proposed by William and Warnke for the strength surface leading to the following expression for the distance from the hydro static pressure axis to an arbitrary point in stress space lying on the strength surface.

$$\frac{r}{r_c} = \frac{2\left(1-\psi^2\right)\cos\theta + \left(2\psi-1\right)\sqrt{4\left(1-\psi^2\right)\cos^2\theta + 5\psi^2 - 4\psi}}{4\left(1-\psi^2\right)\cos^2\theta + \left(1-2\psi\right)^2}$$

$$\psi(p) = \frac{r_t}{r_c} = \text{relative distance between compression and tension meridian}$$

$$\cos 3\theta = \frac{3\sqrt{3}J_3}{2J_2^{\,3/2}}$$

- User input of a curve describing the migration between yield, maximum and residual strength surfaces, $\lambda = \lambda(\eta)$

The compression and extension meridians with stress paths for some tests are schematically shown in Figure B-1 and a schematically strength surface in 3D-stress space is shown in Figure B-2.

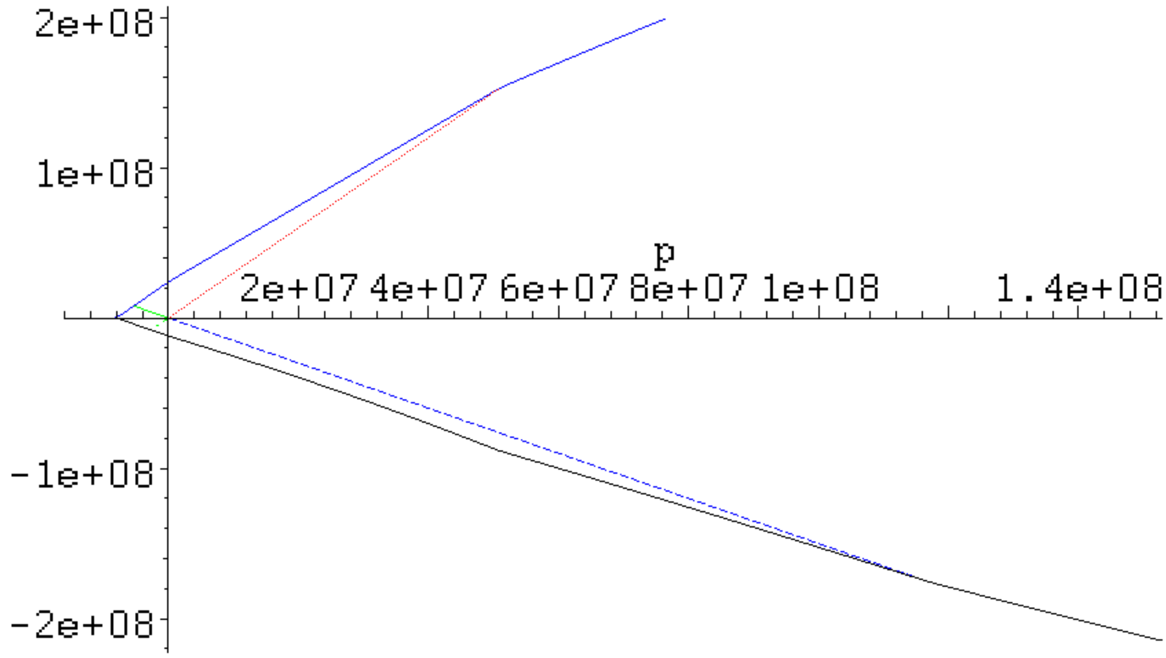

Figure B-1. Compression and extension meridians with stress paths in the Rendulic plane for different tests. Axis units in [Pa].

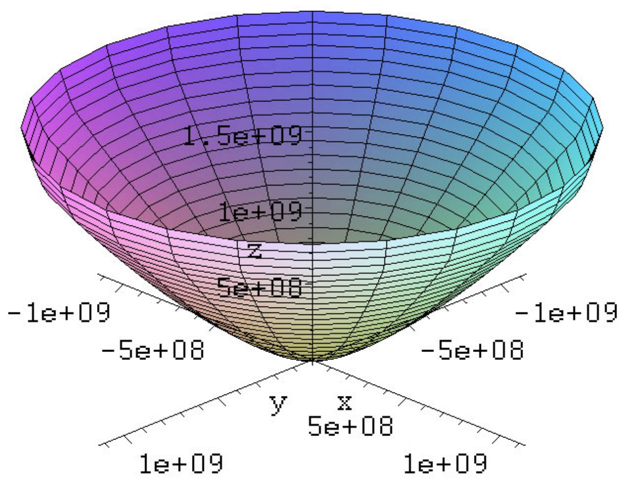

Figure B-2. Strength surface in principal stress space. Axis units in [Pa].

Strength enhancement due to strain rates

The strength enhancement due to strain rates is done along radial stress paths in the stress space. This is in accordance with data from unconfined compressive and tensile tests, but since the enhancement is based on effective strain, the model does not differentiate between compressive and tensile stress paths.

$$\Delta\sigma = r_f \Delta\sigma(p / r_f)$$

$$r_f\left(\varepsilon^{effective}\right) = \text{Strength enhancement factor}$$

The strength enhancement factor is given by the user as a piecewise linear curve, e.g. see Figure B-3.

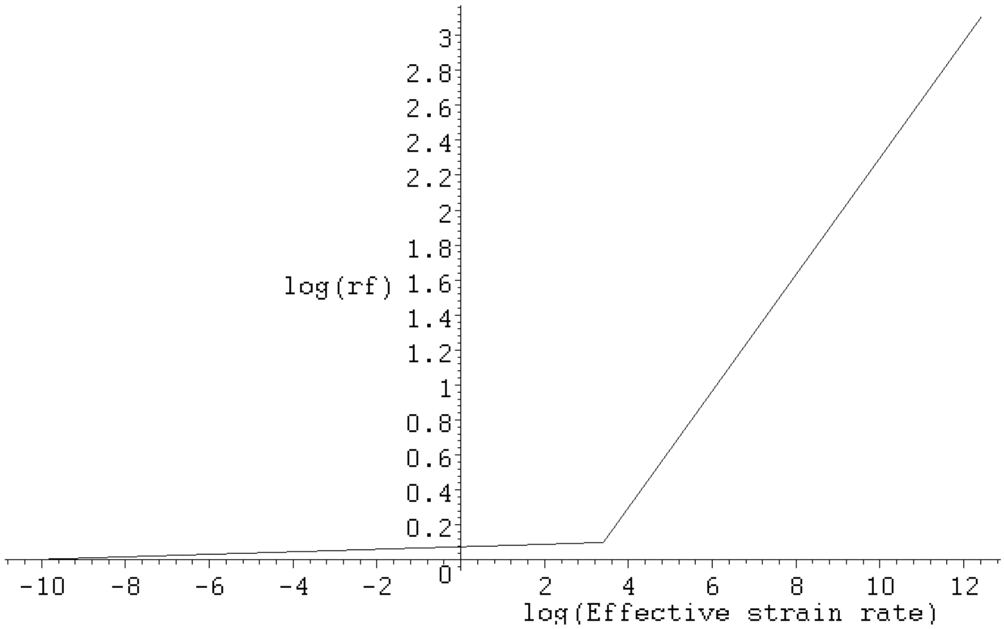

Figure B-3. Example of an strength enhancement function

Damage accumulation

In order to incorporate the yield strength and the residual strength two additional surfaces are defined, see Figure B-4 for a schematic representation.

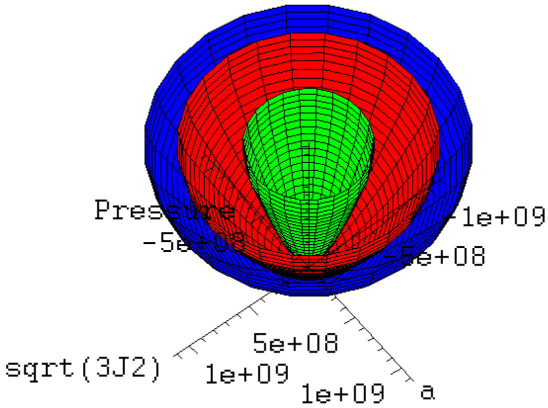

Figure B-4. Yield (red), max. (blue) and residual (green) strength surfaces in stress space

During loading the strength surface has to migrate between the three strength surfaces and this is done using the following relations.

$$\Delta\sigma = \eta(\Delta\sigma_{\max} - \Delta\sigma_{\min})\Delta\sigma_{\min}$$

$$p_c = \begin{cases} -f_{ct} \\ -\eta(\lambda) f_{ct} \end{cases}$$

$$\eta = \eta(\lambda)$$

P_c is the pressure cut-off, i.e. the maximum tensile that can be reached, η is the migration function and λ is called the modified effective plastic strain measure, which is calculated according to:

$$\lambda = \int_0^{\bar{\varepsilon}^p} \frac{d\bar{\varepsilon}^p}{r_f\left(1 + \frac{p}{rf} f_{ct}\right)^{b_i}} + b_3 f_d k_d \left(\varepsilon_v - \varepsilon_v^{yield}\right)$$

where

$$d\bar{\varepsilon}^{p} = \sqrt{\frac{2}{3}\varepsilon_{ij}^{p}\varepsilon_{ij}^{p}}$$

$$b_i = \text{scalar multiplier for uniaxial stress states} = \begin{cases} b_1 \text{ for } p \geq 0 \\ b_2 \text{ for } p < 0 \end{cases}$$

$$b_3 = \text{scalar multiplier for triaxial stress states}$$

$$f_d = \begin{cases} 1 - \dfrac{\left|p^{-1}\sqrt{3J_2}\right|}{0.1} & \text{for } 0 \leq \left|p^{-1}\sqrt{3J_2}\right| \leq 0.1 \\ 0 & \text{for } \left|p^{-1}\sqrt{3J_2}\right| > 0.1 \end{cases}$$

$$k_d = \text{internal scalar multiplier} = -\frac{\varepsilon_v K}{3 f_{ct}}$$

$$\varepsilon_v = -\frac{1}{3}\varepsilon_{ii}$$

The function $\eta(\lambda)$ is given by the user as a piecewise linear curve and the b-parameters are determined through iterative calculations to get the correct fracture energy for different stress paths. The parameter η ranges from some start value <1 representing the yield strength surface, up to 1 for the maximum strength surface and down to 0 for the residual strength surface. An example is given in Figure B-5.

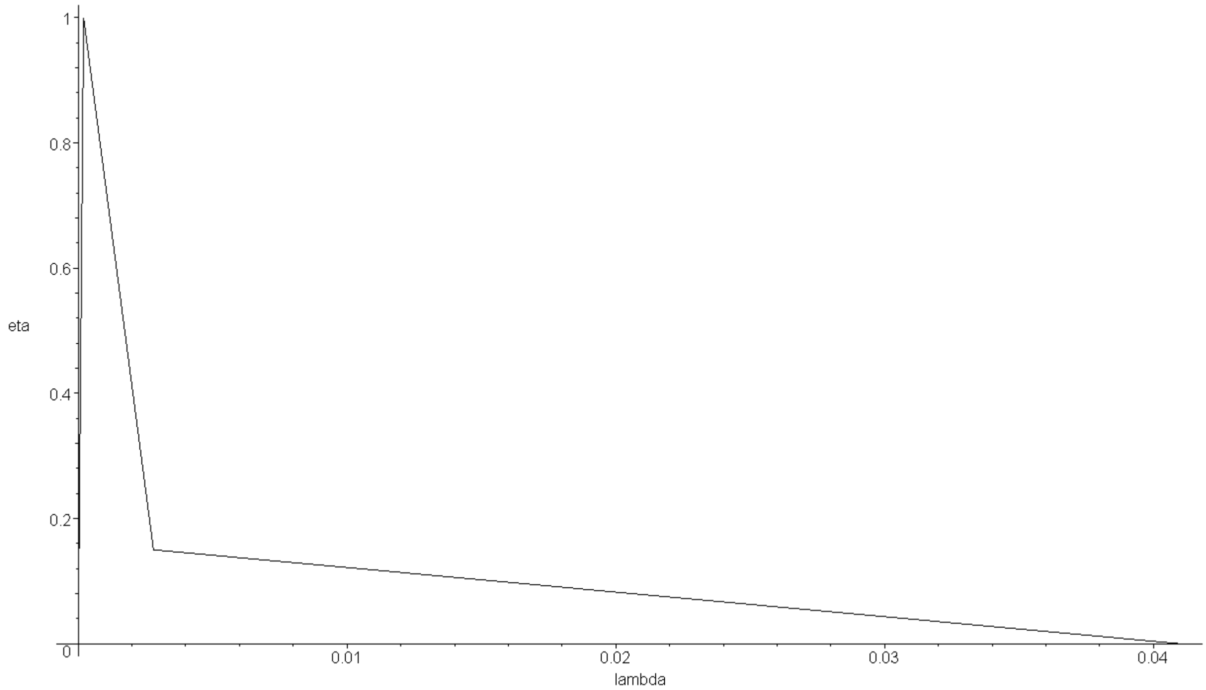

Figure B-5. Example of a damage function

In a situation with negative pressure and softening a modified maximum strength surface is used to avoid a vertical pressure cut-off plane in the stress space:

$$\Delta\sigma_{\max}^{\text{mod}ified} = \begin{cases} \eta\Delta\sigma_{\max} + (1-\eta)\Delta\sigma_{res} & \text{for } p > 0 \\ 3(p + \eta f_{ct}) & \text{for } p \geq 0 \end{cases}$$

Plastic flow

The Concrete Damage model uses the volume-preserving Prandtl-Reuss flow rule, i.e. the plastic flow has a radial direction from the hydrostatic pressure axis.

$$f(p,\eta)=\sqrt{3J_2}-Y$$

where Y is the current position of the strength surface in stress space. The update to the strength surface (after the elastic trial step) becomes

$$Y_{n+1}-Y^* = \frac{Y_{,\eta}\eta'(\lambda)h(\sigma)}{3G}\frac{f(\sigma^*)}{1+Y_{,\eta}\eta'(\lambda)h(\sigma)/3G}$$

where

Y^* = Updated strength surface due to increment pressure

$$Y_{,\eta}\begin{cases} r_f[\Delta\sigma_m(p/r_t)-\Delta\sigma_f(p-r_f)], p\geq p_f, \\ 3r_f f_t, & p<p_f. \end{cases}$$

$$h(\sigma)=r_f\left(1+\frac{p}{rf}f_{ct}\right)^{b_i}$$

The increment for the modified effective plastic strain measure λ is:

$$d\lambda = h(\sigma)d\overline{\varepsilon^p} = h(\sigma)\frac{2}{3}\sqrt{J_2}d\mu = \frac{h(\sigma)[\sqrt{3J_2}*-Y(p^*,\eta_n)]}{3G\left[1+\frac{Y_{,\eta}\eta'(\lambda)h(\sigma)}{3G}\right]}$$

Calculation of shear modulus

The Poisson's ratio is constant and given by the user and the shear modulus is calculated using this value and the bulk modulus from the given equation of state.

$$G=\frac{(1.5-3\nu)K'}{1+\nu}$$

$$K'=(K_L-K_U)e^{-5.55\varphi}+K_U$$

$$\varphi=\frac{-\Delta\varepsilon}{-\Delta\varepsilon+(p-p_f)/K_U}$$

$$\Delta\varepsilon=\varepsilon_{v,\min}-\varepsilon_v$$

where

K_L = Loading bulk modulus

K_U = Unloading bulk modulus

Release II

A second release of the material model was presented in February 1996, but the model is not implemented in the LS-DYNA material library. The main new capabilities in the model are:

(1) incorporation of shear dilatancy

Using a flow rule that assures the plastic strain increments to be normal to the strength surface, i.e. an associative flow rule, yields excessive dilatancy (change in volume) in shear. The Prandtl-Reuss flow rule is a special case of a non-associative flow rule that yields no dilatancy at all. From shear tests on concrete it is found that dilatancy occurs, to a certain degree. In release II the introduction of a general non-associative flow rule controlled by a input parameter ω gives the possibility to handle shear dilatancy.

(2) different rate enhancement in tension and compression

Tests show that strength enhancement due to strain rate is different in tension than in compression. In release II the possibility is given to account for this via a user defined curve ranging from negative (tensile enhancement) to positive (compressive enhancement) strain rates.

(3) variable strain enhancement with strain rate

In addition, strain rate dependency on the peak strain has been added, which the user controls by entering a scalar representing how large a fraction of the strength enhancement curve to be used for strain enhancement.

Release III

In release III beta 20 of the material model, the generation of input material parameters has been automated. The parameter generation is based on the concrete compressive strength, the system of units, and the element size (or relative element size). In addition, release III beta 21 will be able to handle different element sizes using a unit length conversion factor (a characteristic length).

Appendix C

Bofors-99, Constitutive model behaviour (SI-units)

```
dn3d kw93
batch

term 1. plti 1.
gmprt elout 1.E-10 nodout 1.E-10;

c ************************************************************** PARAMETERS ***
c Load rate
 [lr=1.E-4]

c Element size
 [lch=5.E-3]
c [lch=7.5E-3]

c ********************************************************* SYMMETRY PLANES ***
plane 3
 0.  0.  0. -1.  0.  0. 1.E-6 symm
 0.  0.  0.  0. -1.  0. 1.E-6 symm
 0.  0.  0.  0.  0. -1. 1.E-6 symm

c ************************************************************** LOAD CURVE ***
c Deformation load curve
lcd 1 2
 0.    1.
 1000. 1.

c **************************************************** MATERIAL DEFINITIONS ***
mat 1
 type 12 brfo 1 hgqt 5
 ro 2770 g [50.E+9/(2*(1+.2))] sigy 50.E+6 eh [100.E+6/0.0025] bulk 2.843E+10
endmat

eos 8
 npts 7 gamma 0.0 e0 0.0 v0 1.0
 lnv  0.000000  -0.007034  -0.028960   -0.050979
     -0.062837  -0.072613  -0.144392
 pc         0.      2.E+08    2.4E+08    3.9E+08
      5.65E+08   7.37E+08     2.E+09
 ku   2.843E+10  2.843E+10  2.843E+10  2.843E+10
      2.843E+10  2.843E+10  2.843E+10
endeos

c ************************************************ SPECIMEN PART DEFINITION ***
Start
 1 2;
 1 2;
 1 2;
 0. [.5*lch]
 0. [.5*lch]
 0. [.5*lch]

c Uniaxial compression - b1
 fv 1 1 2 2 2 2 1 [lr]  0.  0. -1. 0. 1000.
 b 1 1 2 2 2 2 000111

c Uniaxial tension - b2
c fv 1 1 2 2 2 2 1 [lr]  0.  0.  1. 0. 1000.
c b 1 1 2 2 2 2 000111

c Triaxial tension - b3
c fv 1 1 2 2 2 2 1 [lr]  0.  0.  1. 0. 1000.
c fv 1 2 1 2 2 2 1 [lr]  0.  1.  0. 0. 1000.
c fv 2 1 1 2 2 2 1 [lr]  1.  0.  0. 0. 1000.
c b 1 1 2 2 2 2 000111
```

```
c b 1 2 1 2 2 2 000111
c b 2 1 1 2 2 2 000111

 npb 1 1 2;
 epb 1 1 1;
 mat 1
end

c ********************************************************************** END ***
end
continue

c ****************************************************************** KEYWORD ***
c 5mm mesh
*MAT_CONCRETE_DAMAGE
         1      2770      0.16
    8.0E+6 50.643E+6     0.465  0.657E-9
 22.789E+6     1.033  1.460E-9     0.465  0.657E-9       1.0       1.0      .023
         0         0         0         0         0         0         0
        0.    .02E-3    2.8E-3    41.E-3

        0.        1.       .15        .0

c 7.5mm mesh
*MAT_CONCRETE_DAMAGE
         1      2770      0.16
    8.0E+6 50.643E+6     0.465  0.657E-9
 22.789E+6     1.033  1.460E-9     0.465  0.657E-9     0.682      6.46      .035
         0         0         0         0         0         0         0
        0.    1.5E-4     9.E-4    35.E-4

        0.        1.        .2        .0
```

Appendix D

```
Bofors-99, Target 1-3 (SI-units)

dn3d kw93
batch

term 5.0E-3 plti 1.E-1
gmprt nodout 1.E-10 elout 1.E-10 matsum 1.E-10;
taurus int8 8;

c ************************************************************ PARAMETERS ***
c Projectile
[v = 616] [r = 0.075 / 2] [nose = 0.090] [length = 0.225]
[rc = (r*r+nose*nose)/2/r] [a = asin(nose/rc)]

c *********************************************************** LOAD CURVES ***
c Dynamic increase factor (DIF) in compression according to
c CEB-FIP Model Code 1990
c Linear function.
lcd 1 65
3.00E-05 1.000 3.00E-04 1.017 3.00E-03 1.034 3.00E-02 1.051 3.00E-01 1.069
3.00E+00 1.086 3.00E+01 1.105 4.00E+01 1.107 5.00E+01 1.109 6.00E+01 1.110
7.00E+01 1.111 8.00E+01 1.112 9.00E+01 1.113 1.00E+02 1.114 2.00E+02 1.120
3.00E+02 1.123 4.00E+02 1.125 5.00E+02 1.127 6.00E+02 1.129 7.00E+02 1.130
8.00E+02 1.131 9.00E+02 1.132 1.00E+03 1.133 2.00E+03 1.138 3.00E+03 1.142
4.00E+03 1.144 5.00E+03 1.146 6.00E+03 1.147 7.00E+03 1.149 8.00E+03 1.150
9.00E+03 1.151 1.00E+04 1.152 1.10E+04 1.152 1.20E+04 1.153 1.30E+04 1.154
1.40E+04 1.154 1.50E+04 1.155 1.60E+04 1.156 1.70E+04 1.156 1.80E+04 1.157
1.90E+04 1.157 2.00E+04 1.157 3.00E+04 1.161 4.00E+04 1.163 5.00E+04 1.165
6.00E+04 1.167 7.00E+04 1.168 8.00E+04 1.169 9.00E+04 1.170 1.00E+05 1.171
1.10E+05 1.172 1.20E+05 1.172 1.30E+05 1.173 1.40E+05 1.174 1.50E+05 1.174
1.60E+05 1.175 1.70E+05 1.175 1.80E+05 1.176 1.90E+05 1.176 2.00E+05 1.177
2.10E+05 1.177 2.20E+05 1.178 2.30E+05 1.178 2.40E+05 1.178 2.50E+05 1.179

c Bilinear function.
lcd 2 65
3.00E-05 1.000 3.00E-04 1.017 3.00E-03 1.034 3.00E-02 1.051 3.00E-01 1.069
3.00E+00 1.086 3.00E+01 1.105 4.00E+01 1.216 5.00E+01 1.310 6.00E+01 1.392
7.00E+01 1.465 8.00E+01 1.532 9.00E+01 1.593 1.00E+02 1.650 2.00E+02 2.079
3.00E+02 2.380 4.00E+02 2.619 5.00E+02 2.821 6.00E+02 2.998 7.00E+02 3.156
8.00E+02 3.300 9.00E+02 3.432 1.00E+03 3.555 2.00E+03 4.479 3.00E+03 5.127
4.00E+03 5.643 5.00E+03 6.078 6.00E+03 6.459 7.00E+03 6.800 8.00E+03 7.109
9.00E+03 7.394 1.00E+04 7.658 1.10E+04 7.906 1.20E+04 8.138 1.30E+04 8.358
1.40E+04 8.567 1.50E+04 8.767 1.60E+04 8.957 1.70E+04 9.140 1.80E+04 9.316
1.90E+04 9.485 2.00E+04 9.649 3.00E+04 11.045 4.00E+04 12.157 5.00E+04 13.096
6.00E+04 13.916 7.00E+04 14.650 8.00E+04 15.317 9.00E+04 15.930 1.00E+05 16.499
1.10E+05 17.032 1.20E+05 17.533 1.30E+05 18.007 1.40E+05 18.458 1.50E+05 18.887
1.60E+05 19.298 1.70E+05 19.692 1.80E+05 20.071 1.90E+05 20.436 2.00E+05 20.788
2.10E+05 21.129 2.20E+05 21.459 2.30E+05 21.779 2.40E+05 22.091 2.50E+05 22.393

c ******************************************************* SYMMETRY PLANES ***
plane 2
 0. 0. 0. -1. 0. 0. 1.E-6 symm
 0. 0. 0. 0. -1. 0. 1.E-6 symm

c ************************************************************ INTERFACES ***
 si 1 t14 fd 0.0 material master 1; material slave 2; ;

c ****************************************** LINES AND SURFACES DEFINITIONS ***
 l3d 1 lp 1 [-r] 0.000 [-nose] lrot [rc-r] 0.000 [-nose] 0 1 0 [-90]
 sd 1 L3S 0 0 0 0 0 1 1
 sd 2 cyli 0 0 0 0 0 1. [r]
 sd 3 cyli 0 0 0 0 0 1. 0.700
 sd 4 cyli 0 0 0 0 0 1. 0.150

c ************************************************** MATERIAL DEFINITIONS ***
c Target dummy material
```

```
mat 1
 type 12
 ro 2770 g [50.E+9/(2*(1+.2))] sigy [0.3*150.E+6] eh [100.E+6/0.0025]
 bulk 17.E+9 hgqt 5 brfo 1
endmat

eos 8
 npts 7 gamma 0.0 e0 0.0 v0 1.0
 lnv  0.000000  -0.007034  -0.028960   -0.050979
     -0.062837  -0.072613  -0.144392
 pc         0.     2.E+08    2.4E+08    3.9E+08
      5.65E+08   7.37E+08     2.E+09
 ku   2.843E+10  2.843E+10  2.843E+10  2.843E+10
      2.843E+10  2.843E+10  2.843E+10
endeos

c Projectile
mat 2
 type 1
 ro 7800 e 200.E+9 pr 0.3 hgqt 5 brfo 2
endmat

c *************************************************** CONCRETE PART DEFINITION ***
start
c 5mm
c 1 31 58;
c 1 31 58;
c 1 161;

c 7.5mm
 1 21 44;
 1 21 44;
 1 108;

 0.000 0.010 0.010
 0.000 0.010 0.010
 0.000 0.800

 di 2 3; 2 3; 0;

 sfi -3; 1 2; ; sd 3
 sfi 1 2; -3; ; sd 3
 sfvi -2; 1 2; ; sd 4
 sfvi 1 2; -2; ; sd 4

 res 2 1 1 3 2 2 i 1.1
 res 1 2 1 2 3 2 j 1.1

 b 3 1 1 3 2 2 001000
 b 1 3 1 2 3 2 001000

c Elements in impact area
 epb 1 1 1;
 epb 1 1 1 po 0 0 1;
c Element in exiting area
 epb 1 1 2;
c Nodes in impact area to calculate model's maximum strain rates
 npb 1 1 1;
 npb 1 1 1 po 0 0 1;
 npb 1 1 1 po 0 0 2;

 mat 1
end

c ************************************************* PROJECTILE PART DEFINITION ***
start
 1 4 6 8 11;
 1 4 6 8 11;
```

```
 1 4 9 19;
 [-r/3] [-r/3] 0  [r/3]  [r/3]
 [-r/3] [-r/3] 0  [r/3]  [r/3]
 [-nose/3] [-nose/3] [-nose] [-length]

 di 1 2 0 4 5; 1 2 0 4 5; ;
 di 1 2 0 4 5; ; 1 2;
 di ; 1 2 0 4 5; 1 2;
 pa 3 3 1 z 0
 sfi -1 -5; -1 -5; -1 3; SD 1
 sfi -1 -5; -1 -5; 3 4; SD 2
 di 1 3; ; ;
 di ; 3 5; ;
 coor 1 mx -1.E-4 rz [90];
 lrep 1;
 b 3 1 0 3 3 0 110111
 b 3 3 0 5 3 0 110111

c Projectile rear node
 npb 3 3 4;
c Nose top element
 epb 3 3 1;

 mat 2
 velocity 0 0 [v]
end

c ********************************************************************** end ***
end

c ****************************************** LS-INGRID INTERACTIVE COMMANDS ***
tp 1.E-5
cont
stop

c ********************************************************** KEYWORD FORMAT ***
*MAT_ADD_EROSION
         1
                                                 0.9
c 5mm mesh
*MAT_CONCRETE_DAMAGE
         1      2770      0.16
    8.0E+6 50.643E+6     0.465  0.657E-9
 22.789E+6     1.033  1.460E-9     0.465  0.657E-9       1.0       1.0      .023
         0         0         0         0         0         0         0
        0.    .02E-3    2.8E-3    41.E-3

        0.        1.       .15        .0

c 7.5mm mesh
*MAT_CONCRETE_DAMAGE
         1      2770      0.16
    8.0E+6 50.643E+6     0.465  0.657E-9
 22.789E+6     1.033  1.460E-9     0.465  0.657E-9     0.682      6.46      .035
         0         0         0         0         0         0         0
        0.    1.5E-4     9.E-4    35.E-4

        0.        1.        .2        .0
```

Appendix E

Bofors-99, Target 1-3_sq (SI-units)

```
dn3d kw93
batch

term 5.0E-3 plti 1.E-1
gmprt nodout 1.E-10 elout 1.E-10 matsum 1.E-10;
taurus int8 8;

c ************************************************************** PARAMETERS ***
c Projectile
[v = 616] [r = 0.075 / 2] [nose = 0.090] [length = 0.225]
[rc = (r*r+nose*nose)/2/r] [a = asin(nose/rc)]

c ************************************************************* LOAD CURVES ***
c Dynamic increase factor (DIF) in compression according to
c CEB-FIP Model Code 1990
c Linear function.
lcd 1 65
3.00E-05 1.000 3.00E-04 1.017 3.00E-03 1.034 3.00E-02 1.051 3.00E-01 1.069
3.00E+00 1.086 3.00E+01 1.105 4.00E+01 1.107 5.00E+01 1.109 6.00E+01 1.110
7.00E+01 1.111 8.00E+01 1.112 9.00E+01 1.113 1.00E+02 1.114 2.00E+02 1.120
3.00E+02 1.123 4.00E+02 1.125 5.00E+02 1.127 6.00E+02 1.129 7.00E+02 1.130
8.00E+02 1.131 9.00E+02 1.132 1.00E+03 1.133 2.00E+03 1.138 3.00E+03 1.142
4.00E+03 1.144 5.00E+03 1.146 6.00E+03 1.147 7.00E+03 1.149 8.00E+03 1.150
9.00E+03 1.151 1.00E+04 1.152 1.10E+04 1.152 1.20E+04 1.153 1.30E+04 1.154
1.40E+04 1.154 1.50E+04 1.155 1.60E+04 1.156 1.70E+04 1.156 1.80E+04 1.157
1.90E+04 1.157 2.00E+04 1.157 3.00E+04 1.161 4.00E+04 1.163 5.00E+04 1.165
6.00E+04 1.167 7.00E+04 1.168 8.00E+04 1.169 9.00E+04 1.170 1.00E+05 1.171
1.10E+05 1.172 1.20E+05 1.172 1.30E+05 1.173 1.40E+05 1.174 1.50E+05 1.174
1.60E+05 1.175 1.70E+05 1.175 1.80E+05 1.176 1.90E+05 1.176 2.00E+05 1.177
2.10E+05 1.177 2.20E+05 1.178 2.30E+05 1.178 2.40E+05 1.178 2.50E+05 1.179

c Bilinear function.
lcd 2 65
3.00E-05 1.000 3.00E-04 1.017 3.00E-03 1.034 3.00E-02 1.051 3.00E-01 1.069
3.00E+00 1.086 3.00E+01 1.105 4.00E+01 1.216 5.00E+01 1.310 6.00E+01 1.392
7.00E+01 1.465 8.00E+01 1.532 9.00E+01 1.593 1.00E+02 1.650 2.00E+02 2.079
3.00E+02 2.380 4.00E+02 2.619 5.00E+02 2.821 6.00E+02 2.998 7.00E+02 3.156
8.00E+02 3.300 9.00E+02 3.432 1.00E+03 3.555 2.00E+03 4.479 3.00E+03 5.127
4.00E+03 5.643 5.00E+03 6.078 6.00E+03 6.459 7.00E+03 6.800 8.00E+03 7.109
9.00E+03 7.394 1.00E+04 7.658 1.10E+04 7.906 1.20E+04 8.138 1.30E+04 8.358
1.40E+04 8.567 1.50E+04 8.767 1.60E+04 8.957 1.70E+04 9.140 1.80E+04 9.316
1.90E+04 9.485 2.00E+04 9.649 3.00E+04 11.045 4.00E+04 12.157 5.00E+04 13.096
6.00E+04 13.916 7.00E+04 14.650 8.00E+04 15.317 9.00E+04 15.930 1.00E+05 16.499
1.10E+05 17.032 1.20E+05 17.533 1.30E+05 18.007 1.40E+05 18.458 1.50E+05 18.887
1.60E+05 19.298 1.70E+05 19.692 1.80E+05 20.071 1.90E+05 20.436 2.00E+05 20.788
2.10E+05 21.129 2.20E+05 21.459 2.30E+05 21.779 2.40E+05 22.091 2.50E+05 22.393

c ********************************************************* SYMMETRY PLANES ***
plane 2
 0. 0. 0. -1. 0. 0. 1.E-6 symm
 0. 0. 0. 0. -1. 0. 1.E-6 symm

c ************************************************************** INTERFACES ***
 si 1 t14 fd 0.0 material master 1; material slave 2; ;

c ****************************************** LINES AND SURFACES DEFINITIONS ***
 l3d 1 lp 1 [-r] 0.000 [-nose] lrot [rc-r] 0.000 [-nose] 0 1 0 [-90]
 sd 1 L3S 0 0 0 0 0 1 1
 sd 2 cyli 0 0 0 0 0 1. [r]

c ************************************************ MATERIAL DEFINITIONS ***
c Target dummy material
mat 1
 type 12
```

```
 ro 2770 g [50.E+9/(2*(1+.2))] sigy [0.3*150.E+6] eh [100.E+6/0.0025]
 bulk 17.E+9 hgqt 5 brfo 1
endmat

eos 8
 npts 7 gamma 0.0 e0 0.0 v0 1.0
 lnv  0.000000  -0.007034  -0.028960   -0.050979
     -0.062837  -0.072613  -0.144392
 pc         0.     2.E+08    2.4E+08    3.9E+08
      5.65E+08   7.37E+08     2.E+09
 ku   2.843E+10  2.843E+10  2.843E+10  2.843E+10
      2.843E+10  2.843E+10  2.843E+10
endeos

c Projectile
mat 2
 type 1
 ro 7800 e 200.E+9 pr 0.2 hgqt 5 brfo 2
endmat

c ************************************************** CONCRETE PART DEFINITION ***
start
c 5mm square
 1 67;
 1 67;
 1 161;
 0 0.330
 0 0.330
 0 0.800
 b 2 1 2 2 2 2 001000
 b 1 2 2 2 2 2 001000

c Elements in impact area
 epb 1 1 1;
 epb 1 1 1 po 0 0 1;
c Element in exiting area
 epb 1 1 2;
c Nodes in impact area to calculate model's maximum strain rates
 npb 1 1 1;
 npb 1 1 1 po 0 0 1;
 npb 1 1 1 po 0 0 2;

 mat 1
end

c ************************************************ PROJECTILE PART DEFINITION ***
start
 1 4 6 8 11;
 1 4 6 8 11;
 1 4 9 19;
 [-r/3] [-r/3] 0  [r/3]  [r/3]
 [-r/3] [-r/3] 0  [r/3]  [r/3]
 [-nose/3] [-nose/3] [-nose] [-length]

 di 1 2 0 4 5; 1 2 0 4 5; ;
 di 1 2 0 4 5; ; 1 2;
 di ; 1 2 0 4 5; 1 2;
 pa 3 3 1 z 0
 sfi -1 -5; -1 -5; -1 3; SD 1
 sfi -1 -5; -1 -5; 3 4; SD 2
 di 1 3; ; ;
 di ; 3 5; ;
 coor 1 mx -1.E-4 rz [90];
 lrep 1;
 b 3 1 0 3 3 0 110111
 b 3 3 0 5 3 0 110111

c Projectile rear node
```

```
 npb 3 3 4;
c Nose top element
 epb 3 3 1;

 mat 2
 velocity 0 0 [v]
end

c ********************************************************************** end ***
end

c ****************************************** LS-INGRID INTERACTIVE COMMANDS ***
tp 1.E-5
cont
stop

c ********************************************************** KEYWORD FORMAT ***
*MAT_ADD_EROSION
         1
                                                 0.9
c 5mm mesh
*MAT_CONCRETE_DAMAGE
         1      2770      0.16
    8.0E+6 50.643E+6     0.465  0.657E-9
 22.789E+6     1.033  1.460E-9     0.465  0.657E-9       1.0       1.0      .023
         0         0         0         0         0         0         0
        0.    .02E-3    2.8E-3    41.E-3

        0.        1.       .15        .0
```

Appendix F

Bofors-99, Target 4-6 (SI-units)

```
dn3d kw93
batch

term 2.0E-3 plti 1.E-4
gmprt nodout 1.E-10 elout 1.E-10 matsum 1.E-10;
taurus int8 8;

c ************************************************************** PARAMETERS ***
c Projectile
[v = 617] [r = 0.075 / 2] [nose = 0.090] [length = 0.225]
[rc = (r*r+nose*nose)/2/r] [a = asin(nose/rc)]

c ************************************************************* LOAD CURVES ***
c Dynamic increase factor (DIF) in compression according to
c CEB-FIP Model Code 1990
c Linear function.
lcd 1 65
3.00E-05 1.000 3.00E-04 1.017 3.00E-03 1.034 3.00E-02 1.051 3.00E-01 1.069
3.00E+00 1.086 3.00E+01 1.105 4.00E+01 1.107 5.00E+01 1.109 6.00E+01 1.110
7.00E+01 1.111 8.00E+01 1.112 9.00E+01 1.113 1.00E+02 1.114 2.00E+02 1.120
3.00E+02 1.123 4.00E+02 1.125 5.00E+02 1.127 6.00E+02 1.129 7.00E+02 1.130
8.00E+02 1.131 9.00E+02 1.132 1.00E+03 1.133 2.00E+03 1.138 3.00E+03 1.142
4.00E+03 1.144 5.00E+03 1.146 6.00E+03 1.147 7.00E+03 1.149 8.00E+03 1.150
9.00E+03 1.151 1.00E+04 1.152 1.10E+04 1.152 1.20E+04 1.153 1.30E+04 1.154
1.40E+04 1.154 1.50E+04 1.155 1.60E+04 1.156 1.70E+04 1.156 1.80E+04 1.157
1.90E+04 1.157 2.00E+04 1.157 3.00E+04 1.161 4.00E+04 1.163 5.00E+04 1.165
6.00E+04 1.167 7.00E+04 1.168 8.00E+04 1.169 9.00E+04 1.170 1.00E+05 1.171
1.10E+05 1.172 1.20E+05 1.172 1.30E+05 1.173 1.40E+05 1.174 1.50E+05 1.174
1.60E+05 1.175 1.70E+05 1.175 1.80E+05 1.176 1.90E+05 1.176 2.00E+05 1.177
2.10E+05 1.177 2.20E+05 1.178 2.30E+05 1.178 2.40E+05 1.178 2.50E+05 1.179

c Bilinear function.
lcd 2 65
3.00E-05 1.000 3.00E-04 1.017 3.00E-03 1.034 3.00E-02 1.051 3.00E-01 1.069
3.00E+00 1.086 3.00E+01 1.105 4.00E+01 1.216 5.00E+01 1.310 6.00E+01 1.392
7.00E+01 1.465 8.00E+01 1.532 9.00E+01 1.593 1.00E+02 1.650 2.00E+02 2.079
3.00E+02 2.380 4.00E+02 2.619 5.00E+02 2.821 6.00E+02 2.998 7.00E+02 3.156
8.00E+02 3.300 9.00E+02 3.432 1.00E+03 3.555 2.00E+03 4.479 3.00E+03 5.127
4.00E+03 5.643 5.00E+03 6.078 6.00E+03 6.459 7.00E+03 6.800 8.00E+03 7.109
9.00E+03 7.394 1.00E+04 7.658 1.10E+04 7.906 1.20E+04 8.138 1.30E+04 8.358
1.40E+04 8.567 1.50E+04 8.767 1.60E+04 8.957 1.70E+04 9.140 1.80E+04 9.316
1.90E+04 9.485 2.00E+04 9.649 3.00E+04 11.045 4.00E+04 12.157 5.00E+04 13.096
6.00E+04 13.916 7.00E+04 14.650 8.00E+04 15.317 9.00E+04 15.930 1.00E+05 16.499
1.10E+05 17.032 1.20E+05 17.533 1.30E+05 18.007 1.40E+05 18.458 1.50E+05 18.887
1.60E+05 19.298 1.70E+05 19.692 1.80E+05 20.071 1.90E+05 20.436 2.00E+05 20.788
2.10E+05 21.129 2.20E+05 21.459 2.30E+05 21.779 2.40E+05 22.091 2.50E+05 22.393

c ********************************************************* SYMMETRY PLANES ***
plane 2
 0. 0. 0. -1. 0. 0. 1.E-6 symm
 0. 0. 0. 0. -1. 0. 1.E-6 symm

c ************************************************************** INTERFACES ***
 si 1 t14 fd 0.0 material master 1; material slave 2; ;

c ****************************************** LINES AND SURFACES DEFINITIONS ***
 l3d 1 lp 1 [-r] 0.000 [-nose] lrot [rc-r] 0.000 [-nose] 0 1 0 [-90]
 sd 1 L3S 0 0 0 0 0 1 1
 sd 2 cyli 0 0 0 0 0 1. [r]
 sd 3 cyli 0 0 0 0 0 1. 0.700
 sd 4 cyli 0 0 0 0 0 1. 0.150

c *************************************************** MATERIAL DEFINITIONS ***
c Dummy material - replace in LS-DYNA keyword file with card at end.
```

```
mat 1
 type 12
 ro 2770 g [50.E+9/(2*(1+.2))] sigy [0.3*150.E+6] eh [100.E+6/0.0025]
 bulk 17.E+9 hgqt 5 brfo 1
endmat

eos 8
 npts 7 gamma 0.0 e0 0.0 v0 1.0
 lnv  0.000000  -0.007034  -0.028960   -0.050979
     -0.062837  -0.072613  -0.144392
 pc         0.     2.E+08    2.4E+08    3.9E+08
      5.65E+08   7.37E+08     2.E+09
 ku   2.843E+10  2.843E+10  2.843E+10  2.843E+10
      2.843E+10  2.843E+10  2.843E+10
endeos

mat 2
 type 1
 ro 7800 e 200.E+9 pr 0.3 brfo 2
endmat

c *************************************************** CONCRETE PART DEFINITION ***
start
c 5mm
 1 31 58;
 1 31 58;
 1 81;

c 7.5mm
c 1 21 44;
c 1 21 44;
c 1 54;

 0.000 0.010 0.010
 0.000 0.010 0.010
 0.000 0.400

 di 2 3; 2 3; 0;

 sfi -3; 1 2; ; sd 3
 sfi 1 2; -3; ; sd 3
 sfvi -2; 1 2; ; sd 4
 sfvi 1 2; -2; ; sd 4

 res 2 1 1 3 2 2 i 1.1
 res 1 2 1 2 3 2 j 1.1

 b 3 1 1 3 2 2 001000
 b 1 3 1 2 3 2 001000

c Elements in impact area
 epb 1 1 1;
 epb 1 1 1 po 0 0 1;
c Element in exiting area
 epb 1 1 2;
c Nodes in impact area to calculate model's maximum strain rates
 npb 1 1 1;
 npb 1 1 1 po 0 0 1;
 npb 1 1 1 po 0 0 2;

 mat 1
end

c ************************************************* PROJECTILE PART DEFINITION ***
start
 1 4 6 8 11;
 1 4 6 8 11;
 1 4 9 19;
```

```
 [-r/3] [-r/3] 0  [r/3]  [r/3]
 [-r/3] [-r/3] 0  [r/3]  [r/3]
 [-nose/3] [-nose/3] [-nose] [-length]

 di 1 2 0 4 5; 1 2 0 4 5; ;
 di 1 2 0 4 5; ; 1 2;
 di ; 1 2 0 4 5; 1 2;
 pa 3 3 1 z 0
 sfi -1 -5; -1 -5; -1 3; SD 1
 sfi -1 -5; -1 -5; 3 4; SD 2
 di 1 3; ; ;
 di ; 3 5; ;
 coor 1 mx -1.E-4 rz [90];
 lrep 1;
 b 3 1 0 3 3 0 110111
 b 3 3 0 5 3 0 110111

c Projectile rear node
 npb 3 3 4;
c Nose top element
 epb 3 3 1;

 mat 2
 velocity 0 0 [v]
end

c ********************************************************************** end ***
end

c ****************************************** LS-INGRID INTERACTIVE COMMANDS ***
tp 1.E-5
cont
stop

c ********************************************************** KEYWORD FORMAT ***
*MAT_ADD_EROSION
         1
                                                     0.8
c 5mm mesh
*MAT_CONCRETE_DAMAGE
         1      2770      0.16
    8.0E+6 50.643E+6     0.465  0.657E-9
 22.789E+6     1.033  1.460E-9     0.465  0.657E-9       1.0       1.0      .023
         0         0         0         0         0         0         0
        0.    .02E-3    2.8E-3    41.E-3

        0.        1.       .15        .0

c 7.5mm mesh
*MAT_CONCRETE_DAMAGE
         1      2770      0.16
    8.0E+6 50.643E+6     0.465  0.657E-9
 22.789E+6     1.033  1.460E-9     0.465  0.657E-9     0.682      6.46      .035
         0         0         0         0         0         0         0
        0.    1.5E-4     9.E-4    35.E-4

        0.        1.        .2        .0
```

Appendix G

Bofors-99, Target 7-9 (SI-units)

```
dn3d kw93
batch

term 2.0E-3 plti 1.E-4
gmprt nodout 1.E-10 elout 1.E-10 matsum 1.E-10;
taurus int8 8;

c ************************************************************ PARAMETERS ***
c Projectile
[v = 616] [r = 0.075 / 2] [nose = 0.090] [length = 0.225]
[rc = (r*r+nose*nose)/2/r] [a = asin(nose/rc)]

c *********************************************************** LOAD CURVES ***
c Dynamic increase factor (DIF) in compression according to
c CEB-FIP Model Code 1990
c Linear function.
lcd 1 65
3.00E-05 1.000 3.00E-04 1.017 3.00E-03 1.034 3.00E-02 1.051 3.00E-01 1.069
3.00E+00 1.086 3.00E+01 1.105 4.00E+01 1.107 5.00E+01 1.109 6.00E+01 1.110
7.00E+01 1.111 8.00E+01 1.112 9.00E+01 1.113 1.00E+02 1.114 2.00E+02 1.120
3.00E+02 1.123 4.00E+02 1.125 5.00E+02 1.127 6.00E+02 1.129 7.00E+02 1.130
8.00E+02 1.131 9.00E+02 1.132 1.00E+03 1.133 2.00E+03 1.138 3.00E+03 1.142
4.00E+03 1.144 5.00E+03 1.146 6.00E+03 1.147 7.00E+03 1.149 8.00E+03 1.150
9.00E+03 1.151 1.00E+04 1.152 1.10E+04 1.152 1.20E+04 1.153 1.30E+04 1.154
1.40E+04 1.154 1.50E+04 1.155 1.60E+04 1.156 1.70E+04 1.156 1.80E+04 1.157
1.90E+04 1.157 2.00E+04 1.157 3.00E+04 1.161 4.00E+04 1.163 5.00E+04 1.165
6.00E+04 1.167 7.00E+04 1.168 8.00E+04 1.169 9.00E+04 1.170 1.00E+05 1.171
1.10E+05 1.172 1.20E+05 1.172 1.30E+05 1.173 1.40E+05 1.174 1.50E+05 1.174
1.60E+05 1.175 1.70E+05 1.175 1.80E+05 1.176 1.90E+05 1.176 2.00E+05 1.177
2.10E+05 1.177 2.20E+05 1.178 2.30E+05 1.178 2.40E+05 1.178 2.50E+05 1.179

c Bilinear function.
lcd 2 65
3.00E-05 1.000 3.00E-04 1.017 3.00E-03 1.034 3.00E-02 1.051 3.00E-01 1.069
3.00E+00 1.086 3.00E+01 1.105 4.00E+01 1.216 5.00E+01 1.310 6.00E+01 1.392
7.00E+01 1.465 8.00E+01 1.532 9.00E+01 1.593 1.00E+02 1.650 2.00E+02 2.079
3.00E+02 2.380 4.00E+02 2.619 5.00E+02 2.821 6.00E+02 2.998 7.00E+02 3.156
8.00E+02 3.300 9.00E+02 3.432 1.00E+03 3.555 2.00E+03 4.479 3.00E+03 5.127
4.00E+03 5.643 5.00E+03 6.078 6.00E+03 6.459 7.00E+03 6.800 8.00E+03 7.109
9.00E+03 7.394 1.00E+04 7.658 1.10E+04 7.906 1.20E+04 8.138 1.30E+04 8.358
1.40E+04 8.567 1.50E+04 8.767 1.60E+04 8.957 1.70E+04 9.140 1.80E+04 9.316
1.90E+04 9.485 2.00E+04 9.649 3.00E+04 11.045 4.00E+04 12.157 5.00E+04 13.096
6.00E+04 13.916 7.00E+04 14.650 8.00E+04 15.317 9.00E+04 15.930 1.00E+05 16.499
1.10E+05 17.032 1.20E+05 17.533 1.30E+05 18.007 1.40E+05 18.458 1.50E+05 18.887
1.60E+05 19.298 1.70E+05 19.692 1.80E+05 20.071 1.90E+05 20.436 2.00E+05 20.788
2.10E+05 21.129 2.20E+05 21.459 2.30E+05 21.779 2.40E+05 22.091 2.50E+05 22.393

c ******************************************************* SYMMETRY PLANES ***
plane 2
 0. 0. 0. -1. 0. 0. 1.E-6 symm
 0. 0. 0. 0. -1. 0. 1.E-6 symm

c ************************************************************ INTERFACES ***
 si 1 t14 fd 0.0 material master 1; material slave 2; ;

c ****************************************** LINES AND SURFACES DEFINITIONS ***
 l3d 1 lp 1 [-r] 0.000 [-nose] lrot [rc-r] 0.000 [-nose] 0 1 0 [-90]
 sd 1 L3S 0 0 0 0 0 1 1
 sd 2 cyli 0 0 0 0 0 1. [r]

c ************************************************* MATERIAL DEFINITIONS ***
c Target dummy material
mat 1
 type 12
```

```
 ro 2770 g [50.E+9/(2*(1+.2))] sigy [0.3*150.E+6] eh [100.E+6/0.0025]
 bulk 17.E+9 hgqt 5 brfo 1
endmat

eos 8
 npts 7 gamma 0.0 e0 0.0 v0 1.0
 lnv  0.000000  -0.007034  -0.028960   -0.050979
     -0.062837  -0.072613  -0.144392
 pc         0.     2.E+08    2.4E+08    3.9E+08
      5.65E+08   7.37E+08     2.E+09
 ku   2.843E+10  2.843E+10  2.843E+10  2.843E+10
      2.843E+10  2.843E+10  2.843E+10
endeos

c Projectile
mat 2
 type 1
 ro 7800 e 200.E+9 pr 0.2 hgqt 5 brfo 2
endmat

c Rebars
mat 3
 type 3
 ro 7800 e 207.E+9 pr 0.3 sigy 586.E+6 etan 623.E+6 beta 0.5 fs 0.16
 beam bform truss care 491.E-6
endmat

c Stirrups
mat 4
 type 3
 ro 7800 e 207.E+9 pr 0.3 sigy 586.E+6 etan 623.E+6 beta 0.5 fs 0.16
 beam bform truss care 113.E-6
endmat

c *************************************************** CONCRETE PART DEFINITION ***
start
c 5mm
 1 13 37 49 57 63 67 69;
 1 13 37 49 57 63 67 69;
 1 9 14 39 44 69 74 81;

 0. 0.060 0.180 0.300 0.420 0.540 0.660 0.700
 0. 0.060 0.180 0.300 0.420 0.540 0.660 0.700
 0. 0.0375 0.0625 0.1875 0.2125 0.3375 0.3625 0.400

 b 8 1 1 8 8 8 001000
 b 1 8 1 8 8 8 001000

c Elements in impact area
 epb 1 1 1;
 epb 1 1 1 po 0 0 1;
c Element in exiting area
 epb 1 1 8;
c Nodes in impact area to calculate model's maximum strain rates
 npb 1 1 1;
 npb 1 1 1 po 0 0 1;
 npb 1 1 1 po 0 0 2;

 mat 1
end

c ************************************************* PROJECTILE PART DEFINITION ***
start
 1 4 6 8 11;
 1 4 6 8 11;
 1 4 9 19;
 [-r/3] [-r/3] 0  [r/3]  [r/3]
 [-r/3] [-r/3] 0  [r/3]  [r/3]
```

```
 [-nose/3] [-nose/3] [-nose] [-length]

 di 1 2 0 4 5; 1 2 0 4 5; ;
 di 1 2 0 4 5; ; 1 2;
 di ; 1 2 0 4 5; 1 2;
 pa 3 3 1 z 0
 sfi -1 -5; -1 -5; -1 3; SD 1
 sfi -1 -5; -1 -5; 3 4; SD 2
 di 1 3; ; ;
 di ; 3 5; ;
 coor 1 mx -1.E-4 rz [90];
 lrep 1;
 b 3 1 0 3 3 0 110111
 b 3 3 0 5 3 0 110111

c Projectile rear node
 npb 3 3 4;
c Nose top element
 epb 3 3 1;

 mat 2
 velocity 0 0 [v]
end

c ************************************************** REINFORCEMENT DEFINITION ***
beam
 rt 000000 0.000 0.000 0.000
 rt 000000 0.060 0.000 0.000
 rt 000000 0.180 0.000 0.000
 rt 000000 0.300 0.000 0.000
 rt 000000 0.420 0.000 0.000
 rt 000000 0.540 0.000 0.000
 rt 000000 0.660 0.000 0.000

 rt 111111 0.000 0.000 1.000
0
c 5mm
 1 2 12 3 1 8
 2 3 24 3 1 8
 3 4 24 3 1 8
 4 5 24 3 1 8
 5 6 24 3 1 8
 6 7 24 3 1 8
0
 coor 36
  my 0.060 mz 0.0375;
  my 0.180 mz 0.0375;
  my 0.300 mz 0.0375;
  my 0.420 mz 0.0375;
  my 0.540 mz 0.0375;
  my 0.660 mz 0.0375;

  my -0.060 mz 0.0625 rz 90;
  my -0.180 mz 0.0625 rz 90;
  my -0.300 mz 0.0625 rz 90;
  my -0.420 mz 0.0625 rz 90;
  my -0.540 mz 0.0625 rz 90;
  my -0.660 mz 0.0625 rz 90;

  my 0.060 mz 0.1875;
  my 0.180 mz 0.1875;
  my 0.300 mz 0.1875;
  my 0.420 mz 0.1875;
  my 0.540 mz 0.1875;
  my 0.660 mz 0.1875;

  my -0.060 mz 0.2125 rz 90;
  my -0.180 mz 0.2125 rz 90;
```

```
  my -0.300 mz 0.2125 rz 90;
  my -0.420 mz 0.2125 rz 90;
  my -0.540 mz 0.2125 rz 90;
  my -0.660 mz 0.2125 rz 90;

  my -0.060 mz 0.3375 rz 90;
  my -0.180 mz 0.3375 rz 90;
  my -0.300 mz 0.3375 rz 90;
  my -0.420 mz 0.3375 rz 90;
  my -0.540 mz 0.3375 rz 90;
  my -0.660 mz 0.3375 rz 90;

  my 0.060 mz 0.3625;
  my 0.180 mz 0.3625;
  my 0.300 mz 0.3625;
  my 0.420 mz 0.3625;
  my 0.540 mz 0.3625;
  my 0.660 mz 0.3625;

  lrep 1 2 3 4 5 6 7 8 9 10 11 12 13 14 15 16 17 18 19 20 21 22 23 24 25 26 27
       28 29 30 31 32 33 34 35 36

end

c ******************************************************* STIRRUPS DEFINITION ***
beam
 rt 000000 0.000 0.000 0.0375
 rt 000000 0.000 0.000 0.0625
 rt 000000 0.000 0.000 0.1875
 rt 000000 0.000 0.000 0.2125
 rt 000000 0.000 0.000 0.3375
 rt 000000 0.000 0.000 0.3625
 rt 111111 1.000 0.000 0.000
0
 1 2 5  4 1 7
 2 3 25 4 1 7
 3 4 5  4 1 7
 4 5 25 4 1 7
 5 6 5  4 1 7
0
coor 36
 mx 0.060 my 0.060;
 mx 0.060 my 0.180;
 mx 0.060 my 0.300;
 mx 0.060 my 0.420;
 mx 0.060 my 0.540;
 mx 0.060 my 0.660;

 mx 0.180 my 0.060;
 mx 0.180 my 0.180;
 mx 0.180 my 0.300;
 mx 0.180 my 0.420;
 mx 0.180 my 0.540;
 mx 0.180 my 0.660;

 mx 0.300 my 0.060;
 mx 0.300 my 0.180;
 mx 0.300 my 0.300;
 mx 0.300 my 0.420;
 mx 0.300 my 0.540;
 mx 0.300 my 0.660;

 mx 0.420 my 0.060;
 mx 0.420 my 0.180;
 mx 0.420 my 0.300;
 mx 0.420 my 0.420;
 mx 0.420 my 0.540;
 mx 0.420 my 0.660;
```

```
 mx 0.540 my 0.060;
 mx 0.540 my 0.180;
 mx 0.540 my 0.300;
 mx 0.540 my 0.420;
 mx 0.540 my 0.540;
 mx 0.540 my 0.660;

 mx 0.660 my 0.060;
 mx 0.660 my 0.180;
 mx 0.660 my 0.300;
 mx 0.660 my 0.420;
 mx 0.660 my 0.540;
 mx 0.660 my 0.660;

 lrep 1 2 3 4 5 6 7 8 9 10 11 12 13 14 15 16 17 18 19 20 21 22 23 24 25 26 27
      28 29 30 31 32 33 34 35 36
end

c ********************************************************************** end ***
end

c ****************************************** LS-INGRID INTERACTIVE COMMANDS ***
tp 1.E-5
cont
stop

c ********************************************************** KEYWORD FORMAT ***
*MAT_ADD_EROSION
         1
                                                     0.9
c 5mm mesh
*MAT_CONCRETE_DAMAGE
         1      2770      0.16
    8.0E+6 50.643E+6     0.465  0.657E-9
 22.789E+6     1.033  1.460E-9     0.465  0.657E-9       1.0       1.0      .023
         0         0         0         0         0         0         0
        0.    .02E-3    2.8E-3    41.E-3

        0.        1.       .15        .0

c 7.5mm mesh
*MAT_CONCRETE_DAMAGE
         1      2770      0.16
    8.0E+6 50.643E+6     0.465  0.657E-9
 22.789E+6     1.033  1.460E-9     0.465  0.657E-9     0.682      6.46      .035
         0         0         0         0         0         0         0
        0.    1.5E-4     9.E-4    35.E-4

        0.        1.        .2        .0
```

APPENDIX II

Fourth International Symposium on Impact Engineering, Kumamoto, Japan, 16-18 July 2001

NUMERICAL SIMULATIONS OF THE RESPONSE OF REINFORCED CONCRETE BEAMS SUBJECTED TO HEAVY DROP TESTS

M. Unosson

Swedish Defence Research Agency (FOI), Weapons and Protection
Grindsjön Research Centre, SE-147 25 Tumba, Sweden

ABSTRACT

This paper presents a finite element analysis of impact loading tests of reinforced concrete beams. The purpose of the work is to evaluate the ability of the chosen numerical method and material models to predict the material and structural response. The impact loading was carried out using a drop weight impacting a simply supported beam at mid-span. Four beams, reinforced with steel rebars and stirrups, were tested. The velocity of the drop-weight and the beam, the strain history of lower reinforcement bars and the acceleration history of the beam were registered. A high-speed film camera captured the crack development. The finite element analysis gave a different type of failure compared to the tests. In the test, the failure was mode I cracking combined with crushing in the impact zone. In the simulations, the failure was mainly due to mode II cracking. Changes were made to the model and to the material data but the results from the test could not be reproduced. The conclusion is that the chosen concrete material model does not seem to be capable of correctly describing the problem, given the material properties and the numerical tool of analysis.

KEYWORDS

impact loading, high performance concrete, finite element analysis, material model

TESTS

Tests were performed at FOI in 1999 where reinforced concrete beams were subjected to impact loading using a drop weight. The beams were 4.2 m and simply supported 0.1 m from the ends with a 0.17x0.34 m cross section. The reinforcement consisted of four ø12 mm rebars and 22ø10 mm stirrups. The drop weight had a mass of 718 kg and the cylindrical striker head impacted a steel pad fixed to the beam at 6.7 m/s. Dampers were used to stop the drop-weight after 90 mm of vertical displacement of the beam, corresponding to approximately 20 ms after impact. The test set-up and results are thoroughly presented in Ågårdh et al. (1999). Four beams were tested during which the following registrations were made:

- High speed photos of the beam mid-section
- Striker displacement history
- Striker head acceleration history
- Beam acceleration history near the point of impact
- Beam velocity history at mid-section
- Crack indication at beam side 20 mm above lower surface of beam
- Strain history in lower rebars 200 mm from mid-span
- Strain history in lower rebars at mid-span
- Strain history at the concrete surface at mid-span and at the same height as rebars

MECHANICAL MATERIAL CHARACTERIZATION

The concrete material was characterized through weighing of test specimens, uniaxial compression test of 150x150 mm cubes and ø100x200 mm cylinders and split tensile tests on 150x150 mm cubes. The fracture energy release was determined from RILEM beam testing, see Hilleborg (1985). Confined uniaxial compression tests of ø75x150 mm cylinders were performed by the Norwegian Defence Research Establishment (FFI) with the gauged reactive confinement (GREAC) cell, see Ågårdh (1999). The initial density was 2420 kg/m^3 and the Poisson's ratio was taken from (2000). The test results are given in Tables 1 and 2. The steel reinforcement was characterized through uniaxial tension test on a ø12 mm rebar. The density and Poisson's ration were set as defaults according to standard tables.

TABLE 1
UNCONFINED STATIC MECHANICAL PROPERTIES OF THE CONCRETE MATERIAL

Modulus of elasticity [GPa]	Poisson's ratio [-]	Compressive strength [MPa]	Split tensile strength [MPa]	Fracture energy [Nm^{-1}]
44	0.16	100	6.5	156

TABLE 2
CONFINED STATIC MECHANICAL PROPERTIES OF THE CONCRETE MATERIAL

Relative volume (V/V_0) [-]	Volumetric strain $\varepsilon_v=\ln(V/V_0)$ [-]	Pressure $p=-1/3\mathrm{tr}(\mathbf{T})$ [MPa]	Unloading/loading bulk modulus $dp/d\varepsilon_v$ [GPa]
1.0000	0.0000	0	9
0.9896	-0.0104	90	9
0.9715	-0.0289	216	-
0.9503	-0.0510	390	-
0.9391	-0.0628	565	-
0.9300	-0.0726	737	25

TABLE 3
STATIC MECHANICAL PROPERTIES OF THE REINFORCEMENT

Density [kgm^{-3}]	Modulus of elasticity [GPa]	Poisson's ratio [-]	Yield strength [MPa]	Tensile strength [MPa]
7 800	207	0.3	586	684

MECHANICAL CONSTITUTIVE MODELLING

To model the concrete beam the K&C concrete model release III, see Malvar et al. (1997), was used. The source code was made available to FOI through an agreement with the developers. Release I of this model is available in the LS-DYNA as material type 72. The input parameters for this model are valid for one element size only, which results in erroneous fracture energy release when using different element sizes in a model. Modifications were made to the source code to scale the plastic deformation relative the size of the current element during the softening phase of the material. In Figure 1 results from simulations of a uniaxial tension test with the modified material model using different element sizes are shown together with the recommendations in the CEB-FIP model code 90 (1993). The response curves display the same softening behaviour and integration gives the same energy release, i.e. related to fracture energy release the model is independent of the spatial discretization. In the model, the elastic material properties, except for the Poisson's ratio, are derived from the equation of state. The test data for the equation of state in Table 2 was complemented with two data points to get a correct elastic wave speed and to get correspondence with the uniaxial data on the modulus of elasticity. Strength enhancement factors due to high loading rate were taken from the CEB-FIP model code 90 (1993). For the stirrups, a linear elastic-plastic material model with isotropic hardening was used and for the rebars a linear elastic-perfectly plastic material model due to restrictions in the code. The drop weight was modelled with a linear elastic material model.

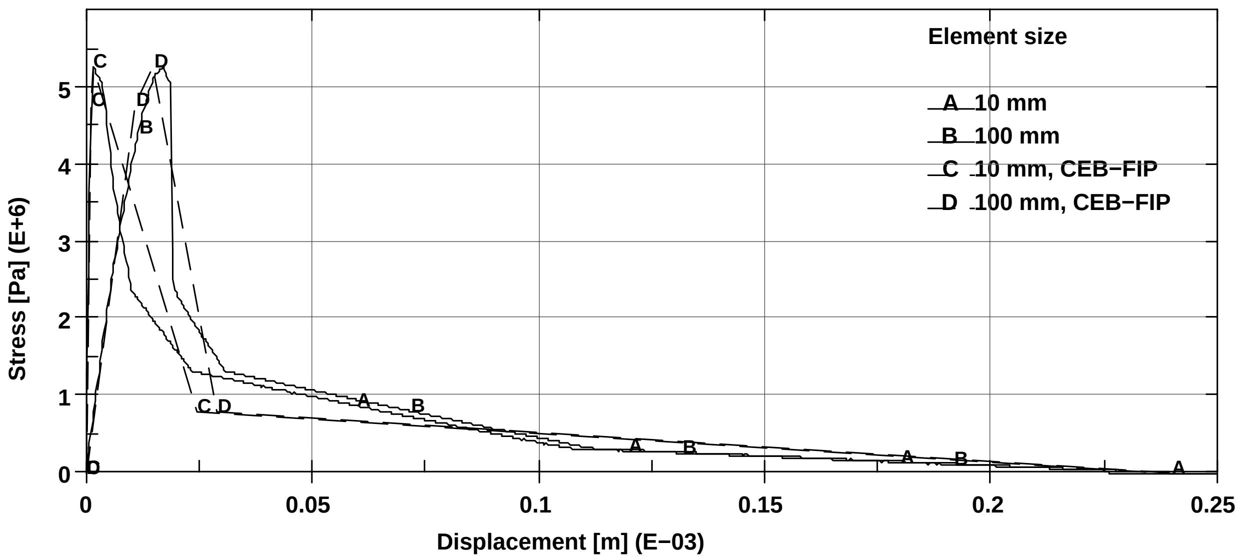

Figure 1: Uniaxial extension of hexahedral element with user-modified version of the K&C concrete material model and comparison with the recommendations in the CEB-FIP model code 90 (1993).

FINITE ELEMENT MODEL

The three dimensional problem was numerically analysed in the finite element code LS-DYNA version 950d, see the LS-DYNA Keyword user's manual (1999), and a material description of the motion was used. The concrete beam and drop weight were discretized in space with eight-node cubical elements. One-point Gauss integration and viscous hourglass control was used for the beam and weight. For the steel-pad and striker-head selectively reduced integration was used. The reinforcement bars were spatially discretized with beam elements and the stirrups with truss elements. For the problem double symmetry was used, see Figure 2. The mesh consisted of 42871 nodes, 36823 cube elements and 626 beam and truss elements. For the two contact interfaces, striker-steel pad and steel pad-beam, a surface to surface constraint algorithm with friction was used. Adjacent beam and reinforcement nodes were merged. The dampers were not incorporated in the model and the problem was only analysed up to 20 ms after impact.

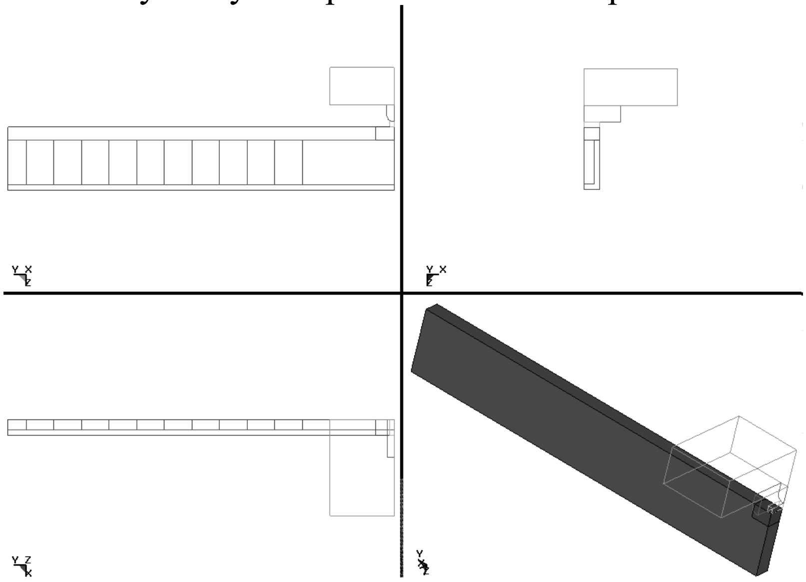

Figure 2: Problem geometry with double symmetry.

NUMERICAL ANALYSIS AND COMPARISON WITH TEST RESULTS

The results from the simulations displayed a different behaviour than the test results. In the tests cracks in mode I (tension) were initiated, the first approximately 0.3 ms after impact, at the bottom of the beam followed by crushing of the material in the impact zone. The simulations reproduced the first mode I crack but also displayed an almost instantaneous initiation of a mode II (in plane shear) crack 50 mm from the centre point of impact. This crack then propagated through the beam resulting in a partial separation of the material directly under the striker and the rest of the beam. This shear failure allowed for no additional mode I cracks to develop, as well as no crushing of the impact zone. Any problems induced by the double symmetry were investigated by performing computations using both single and double symmetry and it was concluded, based on negligible differences in the results, that double symmetry could be used in the problem. With the concrete model, various degrees of associativity of the flow rule can be used. This was also investigated and it was concluded that the degree of associativity also had negligible effect on the results. Three different equations of state were used but the type of failure changed only slightly. Comparisons are made below between the registrations from the test and the corresponding data from the numerical analysis.

- **High speed photos**. Comparisons between the high-speed photos and damage plots from the model are given in Figures 3 and 4.
- **Striker displacement**. In the numerical analysis, the striker is displaced more than compared to the test. This is due to the partitioning of the beam caused by the shear failure.
- **Striker head acceleration**. In the test, the peak acceleration is 18000 ms^{-2}. The model gives rigid body acceleration for the striker head of 8000 ms^{-2}. The lower value from the model can also be explained by the shear-induced failure.
- **Beam acceleration**. Data on the nodal acceleration was hard to use for comparisons due to oscillations. However, integration of the signals shows that the speed of the beam is lower in the model than in the test. Again, this is due to the shearing failure.
- **Beam displacement**. The model shows a larger displacement of the mid-centre section of the beam compared to the test. This is in accordance with the striker displacement.
- **Crack indication**. For the mode I crack at the lower surface of the beam, the model reproduces well the time for the initiation. A stress-strain plot reveals that the material behaviour in uniaxial extension is accurately described.
- **Strain in lower rebars.** The strain histories in the model show good agreement with the test but after approximately one millisecond the strain gauges reaches their maximum range.
- **Strain in concrete**, at the same height as the tension reinforcement. The strain in the model is slightly smaller than the test data. The strain gauges reaches their maximum range after 0.5 ms.

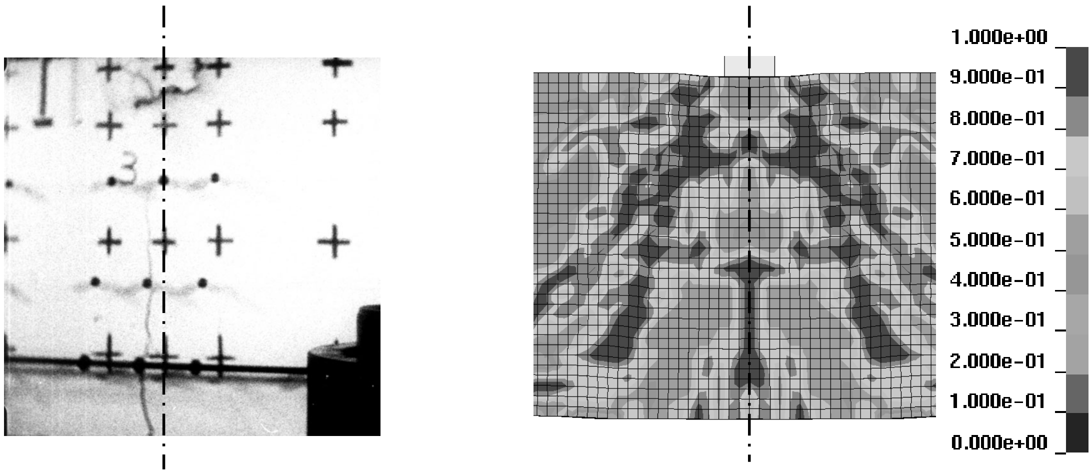

Figure 3: High-speed photo at mid-span and numerical damage plot after 1 ms. Beam mid-span indicated by dash-dotted line.

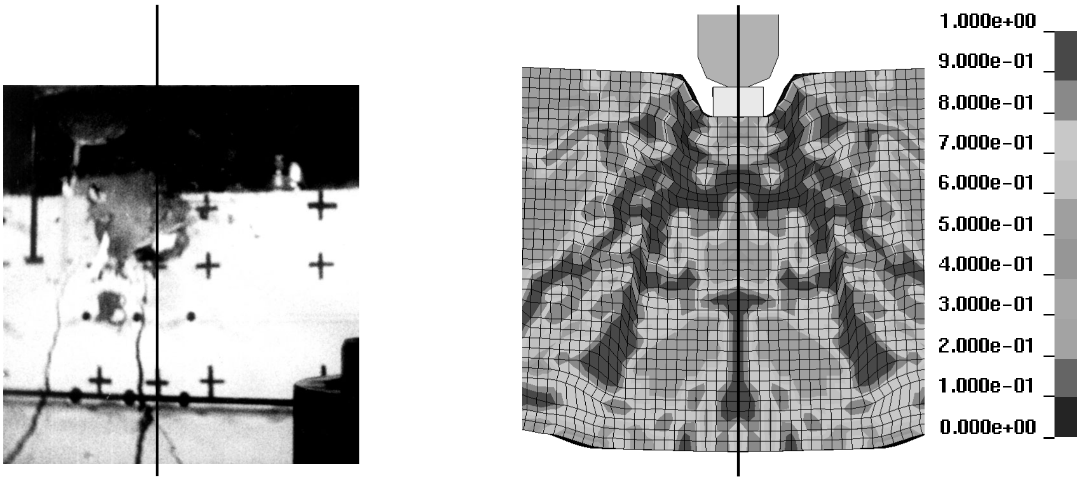

Figure 4: High-speed photo at mid-span and numerical damage plot after 20 ms. Beam mid-span indicated by dash-dotted line.

SUMMARY

An investigation has been carried out to determine if a numerical model could be used to reproduce the results from a drop-weight test on reinforced concrete beams. A short description of the tests performed is given with a reference to the corresponding test data report. Mechanical material characterization was performed on both the concrete and the steel reinforcement material. The data was then adapted to the concrete material model. Simulations were performed where investigations were made on how symmetry, flow rule associativity and the equation of state influenced the results.

The conclusion from this study is that the concrete material model is able to accurately describe material response for standard tests such as uniaxial extension and compression. However, it does not seem to be able to reproduce the structural response in the tests performed, given the available data on the material properties and the numerical tool of analysis used. Suggestions for future implementation of the material model are to include:

- The possibility to use full or selectively reduced integration for hexahedral elements. In the current implementation, the model is valid only for one-point integrated hexahedral elements and for the zone near the impact this can be insufficient.
- Inelastic deformations due to isotropic compression, i.e. the volumetric strain from the equation of state, in the model's damage evolution.
- Non-local material behaviour. This is one way to avoid strain localization, as in the present problem, by introducing non-local measures of deformation in the

material model Bazant & Planas (1997). A simple method is to calculate local strains and to choose a domain of influence. A weight function is then applied to the local strains in this domain and the resulting, weighted strain is used to calculate inelastic strain. In the present model the inelastic strain is represented by a scalar valued damage parameter.

ACKNOWLEDGEMENTS

The author thanks John E. Crawford, Javier Malvar and Kenneth B. Morrill at Karagozian & Case Structural Engineers for supplying the source code and for the discussion on the concrete model. Also, Eric Buzaud at the Centre d'études de Gramat on whose opinions and help the author always rely on and appreciate. Finally, thanks to Håkan Hansson and Lars Olovsson at FOI who made this study possible.

(1993) *CEB-FIP model code 1990, Comité euro-international du béton (CEB) et Fédération internationale de la précontrainte (FIP),* Thomas Telford, London.

(1999). *LS-DYNA Keyword user's manual, version 950.* Livermore Software Technology Corporation (LSTC), Livermore.

(2000). *Handbook for concrete, High performance concrete - Material and design (In Swedish).* AB Svensk byggtjänst, Stockholm.

Bazant, Z. P. and Planas, J. (1997). *Fracture and size effect in concrete and other quasibrittle materials.* CRC Press, Boca Raton.

Hilleborg, A. (1985). Determination of the fracture energy of mortar and concrete by means of three-point bend tests on notched beams. *Materials and structures.* **13:**285-290.

Malvar, L. J., Crawford, J. E., Wesevich, J. W. and Simons, D. (1997). A plasticity concrete material model for dyna3d. *International Journal of Impact Engineering.* **19**:9-10**,** 847-873.

Ågårdh, L. (1999). *Material Test Procedures in Support of Dynamic Material Modelling.* FOA-R--99-01227-311--SE. Defence research establishment (FOA), Tumba.

Ågårdh, L., Magnusson, J. and Hansson, H. (1999). *High strength concrete beams subjected to impact loading - An experimental study.* FOA-R--99-01187-311--SE. Defence research establishment (FOA), Tumba.

APPENDIX III

SWEDISH DEFENCE
RESEARCH AGENCY

FOI-R--0262--SE
March 2002
ISSN 1650-1942

Technical report

Mattias Unosson and Lars Olovsson

Finite element analysis of the splitting test

Weapons and Protection
SE-147 25 Tumba

SWEDISH DEFENCE RESEARCH AGENCY

Weapons and Protection
SE-147 25 Tumba

FOI-R--0262--SE

March 2002

ISSN 1650-1942

Technical report

Mattias Unosson and Lars Olovsson

Finite element analysis of the splitting test

1 Introduction

At the Swedish Defence Research Agency (FOI) applied research is done on how to assess and optimize the protection level of concrete structures subjected to conventional weapon loadings. The modelling of concrete material is a challenging task, especially when the loading is three dimensional and applied at high rates. Two different material models have been used extensively at the Swedish Defence Research Agency and one of them is used in this study. The scrutinized material model has mainly been used for problems involving impact loading and it is here shown to be inadequate for these purposes. This report presents the behaviour of this model in a splitting test and a simplified non-local continuum approach applied in a tensile test. Based on two years of experience in this field, the report is concluded with thoughts on what is necessary to better model concrete materials.

1.1 Splitting test

Performing a direct tension test on a concrete material is expensive and the preparation of the test specimen is time demanding. The loading rig has to be very stiff in order to capture the complete response curve due to the softening behaviour of the concrete material. The preparation of the specimen consists of manufacturing a notched specimen of the granular material and of gluing grips to the ends, to which the load cell is to be fastened. A simpler way of determining the tensile strength is the splitting test, or the Brazilian test, originating from rock mechanics. This test, on the other hand, is load-controlled and does not provide any information on the softening behaviour. In this method a cubical or cylindrical specimen is subjected to a uniaxial line-load that induces tensile stresses at the centre of the specimen, see Figure 1-1 and Figure 1-2.

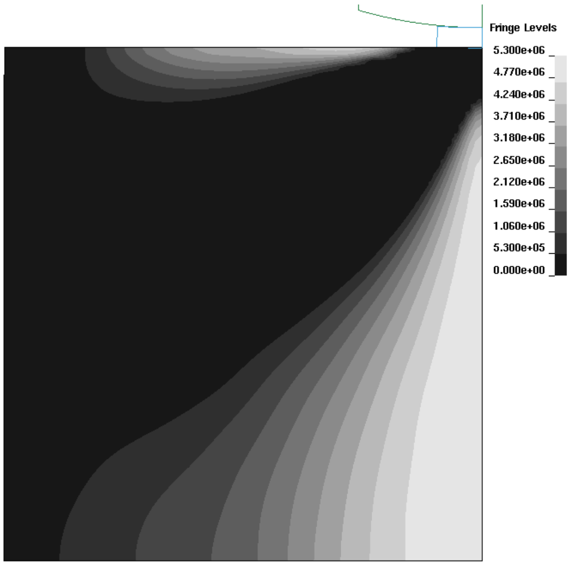

Figure 1-1 Fringes of lateral stresses in an elastic analysis.

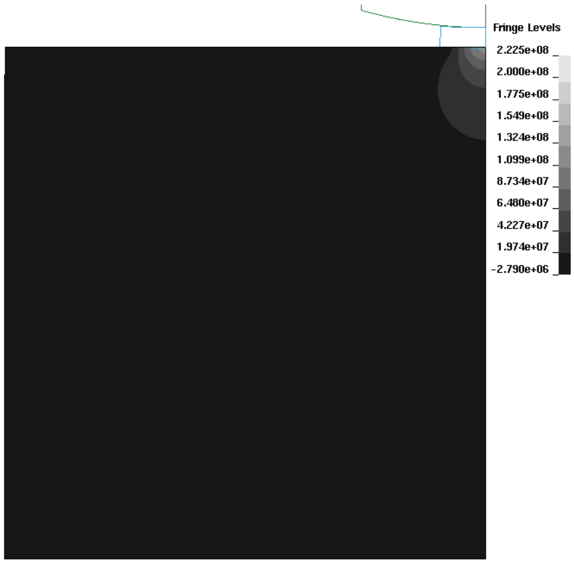

Figure 1-2 Fringes of hydrostatic pressure in an elastic analysis.

The splitting test only works with materials that have an increase in strength with increasing pressure. Otherwise the failure would not occur at the centre of the specimen but in the area under the applied load where large compressive stresses are induced. The test set-up is shown in Figure 1-3. In the test the peak load is registered and the splitting strength is then calculated using an analytical expression and an empirical relation to approximate the tensile strength, cf. Ljungkrantz et al. [1]. At the Swedish Defence Research Agency, this has been the prevailing method when estimating tensile strength input for numerical models. Examples of earlier work where this test has been studied numerically are Feenstra and Borst [2], who used a cubical specimen, Sawamoto et al. [3], who used a cylindrical specimen and a discrete element method and Comi [4], who used a cubical specimen and the Finite Element Method (FEM).

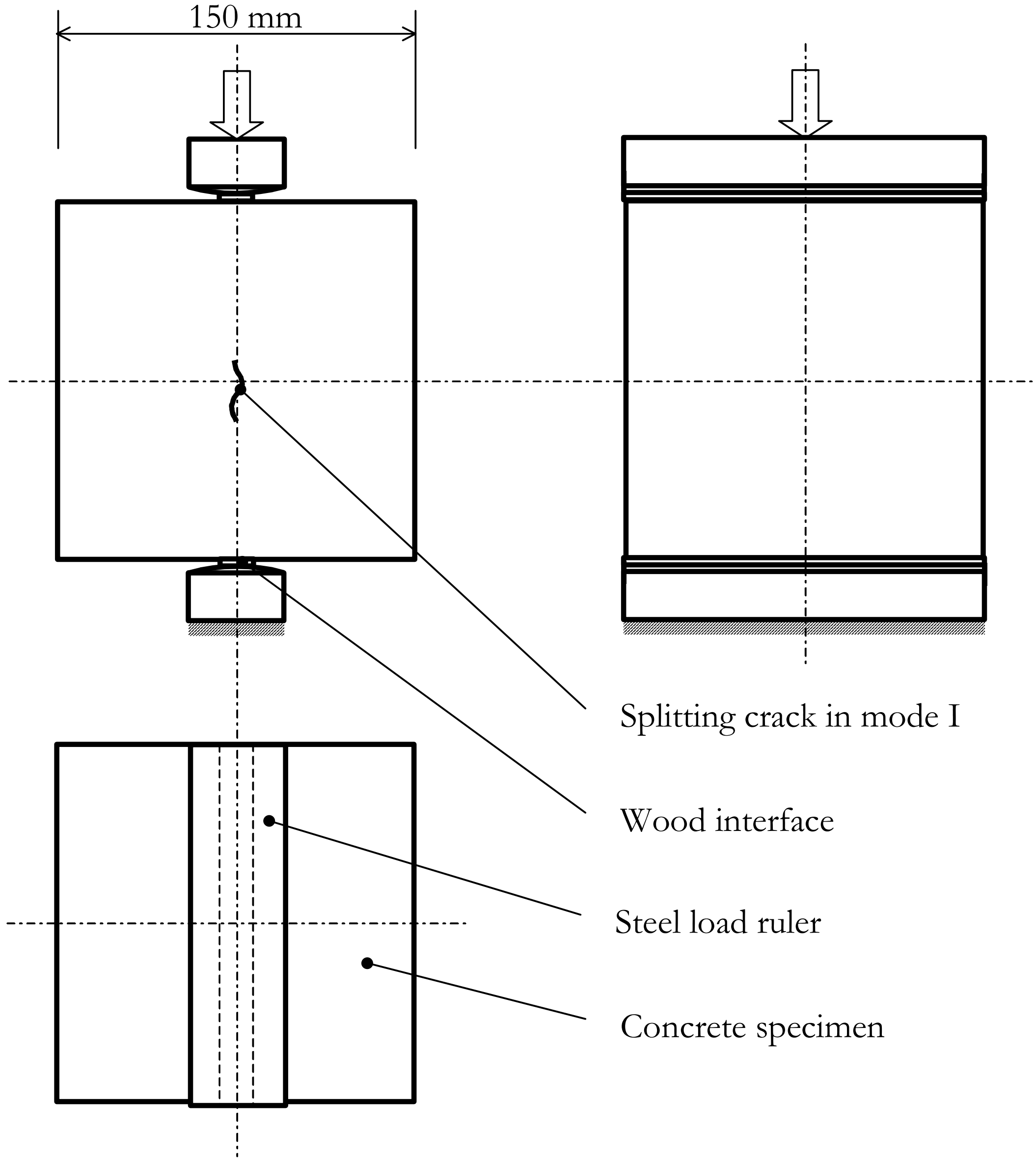

Figure 1-3 Test set-up of splitting test according to the Swedish standard SS 13 72 13 [5]**.**

1.2 Non-local model

The presence of a strain singularity gives rise to mesh sensitivity and in combination with a failure criterion a non-convergent solution. One way to circumvent problems of localization and singularities is to introduce a non-local measure of deformation. In this way the stress at a point does not only depend on the deformation at that point, which is one of the fundamental statements in continuum mechanics, cf. Noll [6], but also on the deformation in a neighbourhood to that point. The idea to use a non-local description of the continuum is found in Eringen [7]. A simple way of introducing non-locality is to define a non-local strain measure based on a weighted average of the local strain field, cf. Bazant and Planas [8].

2 Methods

2.1 Non-local kinematics

In LS-DYNA version 960 a simplified method for non-local treatment has been implemented for solid elements with one-point integration. The local strain measure is weighted and integrated over the element neighbourhood using the following expression, from Bazant and Planas [8], for the non-local rate of evolution of the strain:

$$D(\mathbf{x}_e) = \frac{\sum_{i=1}^{N_r} D_{local} w_{ei} V_i}{\sum_{i=1}^{N_r} w_{ei} V_i}$$

$$w_{ei} = w(\mathbf{x}_e - \mathbf{x}_i) = \frac{1}{\left[1 + \left(\frac{\|\mathbf{x}_e - \mathbf{x}_i\|}{L}\right)^p\right]^q}$$

where D_{local} is the local strain rate measure, w_{ei} is a weight function, $\mathbf{x}_e$ is the position vector of the element integration point, $\mathbf{x}_i$ is the position vector of a neighbouring element and V_i is the corresponding element volume. L is the radius of the element neighbourhood as shown in Figure 2-1. The weight function with the parameters p and q set to 8 and 2, respectively, is shown in Figure 2-2 for the two-dimensional case. In this study the parameters were set to p=8 and q=2 with neighbourhood radius 5 and 2.5 mm. The effect on the weight function of the parameters is shown in Figure 2-3 and Figure 2-4.

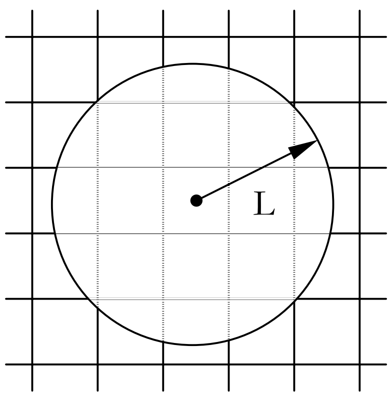

Figure 2-1 Element neighbourhood with radius L.

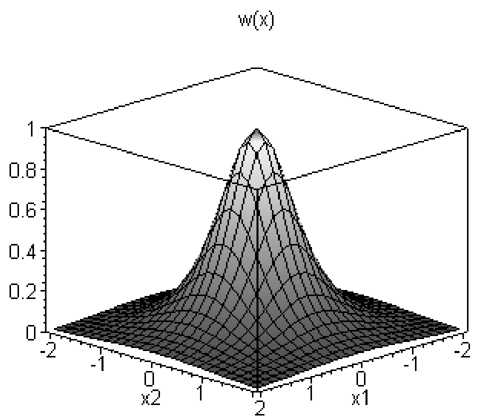

Figure 2-2 Weight function over element neighbourhood with p=8 and q=2.

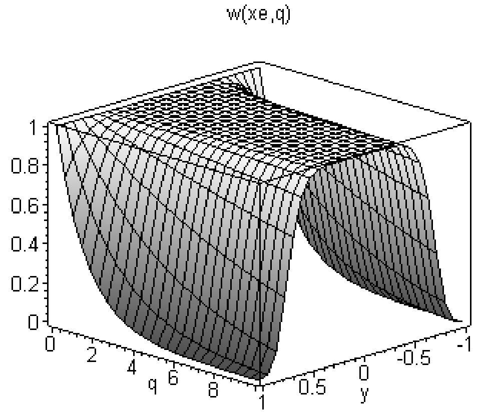

Figure 2-3 Weight function as a function of neighbouring element position and q with p=8.

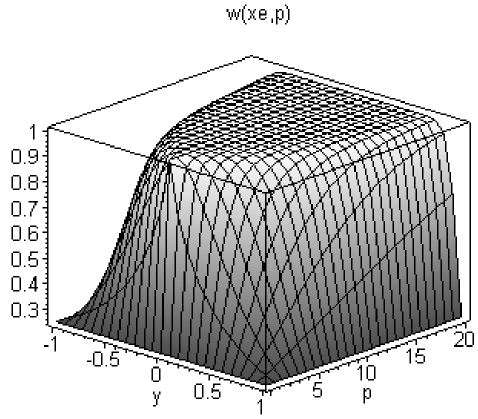

Figure 2-4 Weight function as a function of neighbouring element position and p with q=2.

2.2 Constitutive equations

The concrete material was modelled with a user-modified version of the K&C concrete model by Malvar et al. [9], where a scaling of the softening behaviour based on the element size was introduced. The material input parameters were taken the same as in Unosson [10] and [11]. The wood interface and the steel load ruler were modelled using an isotropic elastic model with the parameters given in Table 2-1.

Table 2-1 Isotropic elastic parameters for the wood interface and the steel load ruler.

Material	Mass density [kg m^{-3}]	Modulus of elasticity [GPa]	Poisson's ratio [-]
Wood	500	17	0.45
Steel	7 800	200	0.2

The non-local treatment of strains is not implemented in LS-DYNA version 960 for all material models, why an elastic-plastic model with the von Mises yield criterion and a kinematic hardening with the parameters given in Table 2-2 was used in a tensile test instead.

Table 2-2 Parameters for the elastic-plastic model with isotropic hardening.

Mass density [kg m^{-3}]	Modulus of elasticity [GPa]	Poisson's ratio [-]	Yield strength [MPa]	Hardening modulus [GPa]
2 420	44	0.16	5.3	1.0

2.3 Finite element analysis

For the spatial discretization reduced integrated eight node brick elements with viscous hourglass control were used. The contact definition relied on a penalty based surface-to-surface algorithm with friction. The loading was applied through prescribed nodal displacements. The finite element analysis was carried out using LS-DYNA version 960.

3 Results

3.1 Splitting test

The current version of the software is incapable of treating the K&C concrete model with a non-local theory. Consequently the splitting test has only been analyzed with a local formulation. Three different models were defined for the simulations; a three-dimensional model, a plane strain model and a plane stress model. The geometry for the three-dimensional model is shown in Figure 3-1 and the geometry for the plane stress and plane strain models in Figure 3-2. Four levels of spatial discretization were used with every geometry.

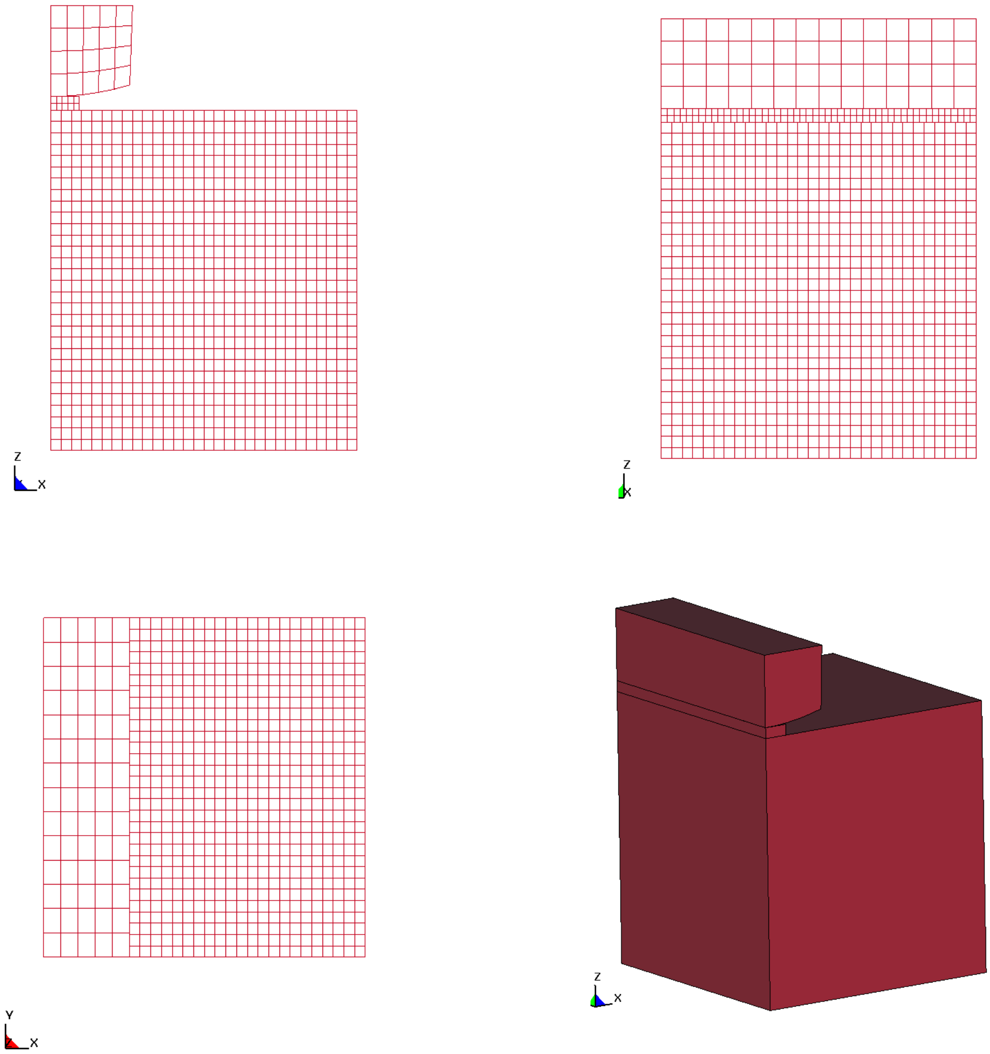

Figure 3-1 Three-dimensional geometry with symmetry in the xy-, yz- and xz-planes.

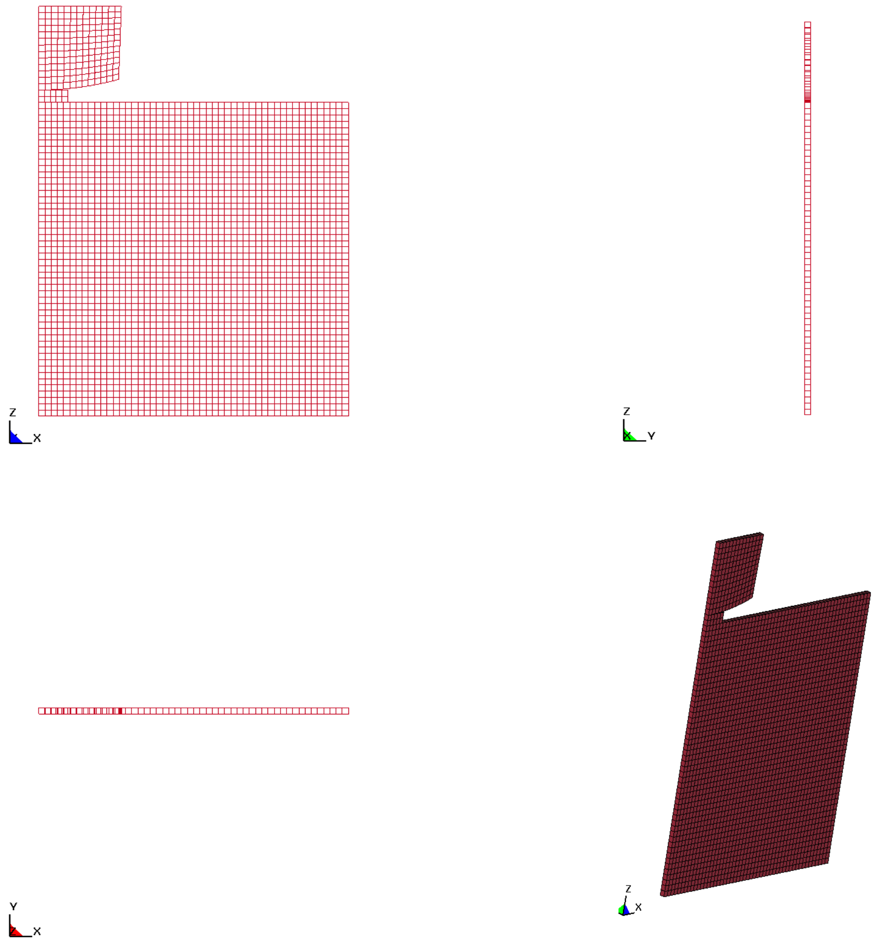

Figure 3-2 Plane strain and stress geometry with symmetry in the xy- and yz- planes.

The global convergence properties and the resulting load-displacement relations for these three models are shown in Figure 3-3 to Figure 3-8. In the figures *h* is the finite element size.

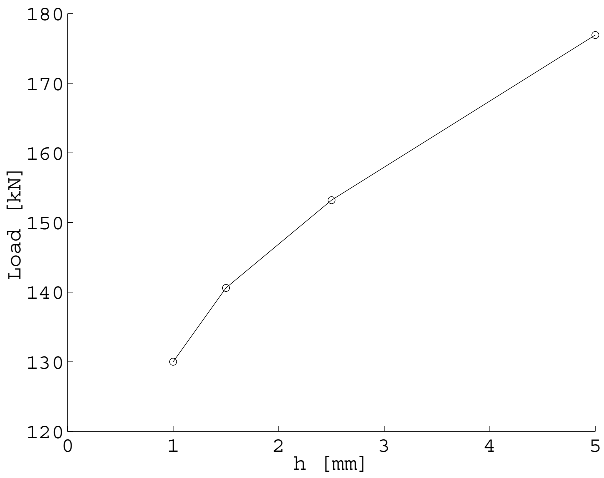

Figure 3-3 Peak load in the 3D-model versus finite element size.

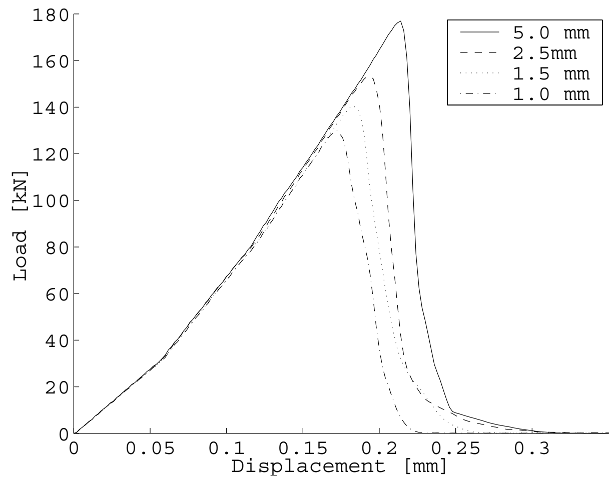

Figure 3-4 Load versus displacement in the 3D-model with four different finite element sizes.

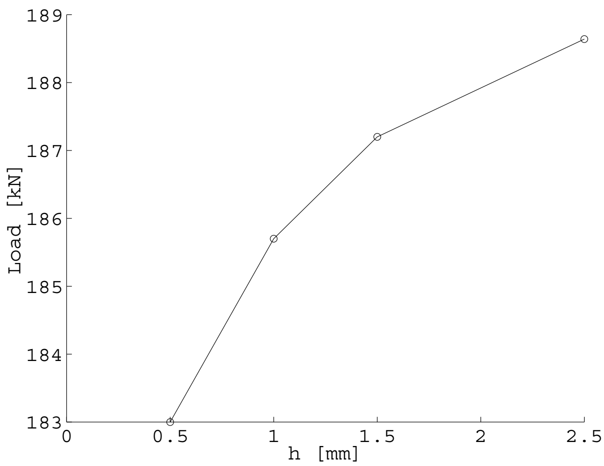

Figure 3-5 Peak load in the plane strain model versus finite element size.

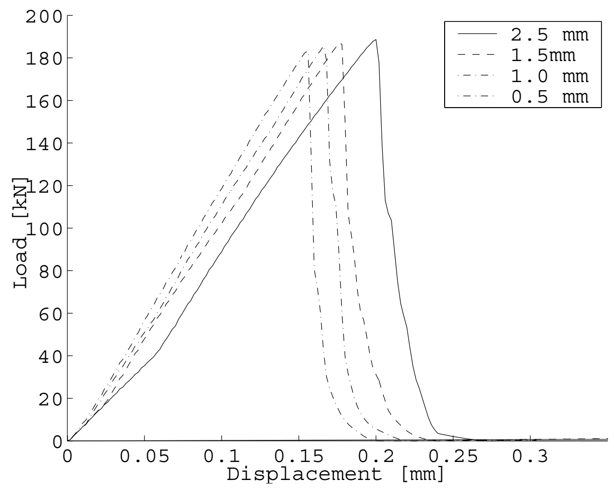

Figure 3-6 Load versus displacement in the plane strain model with four different finite element sizes.

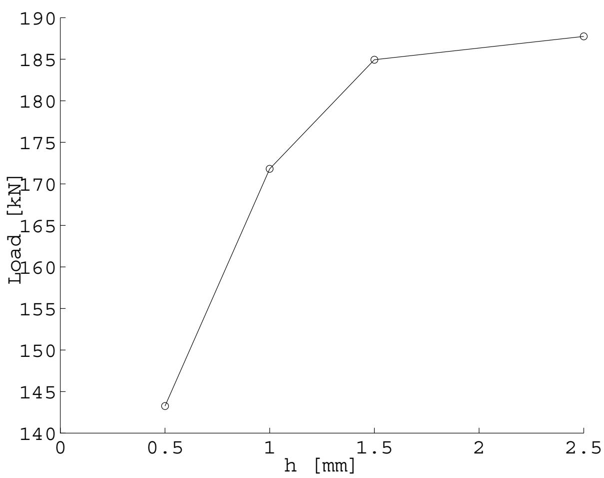

Figure 3-7 Peak load in the plane stress model versus finite element size.

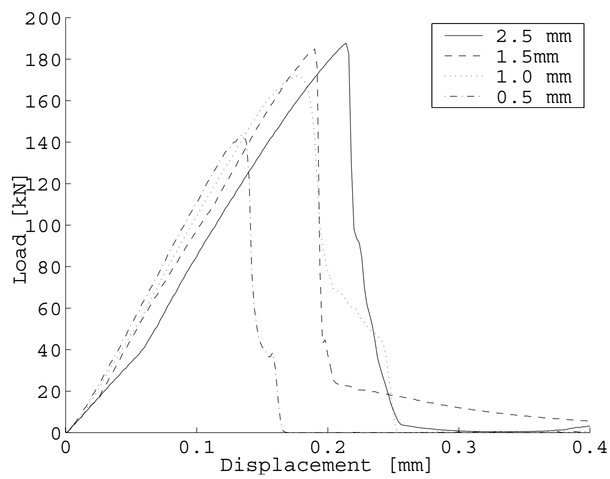

Figure 3-8 Load versus displacement in the plane stress model with four different finite element sizes.

For the 2.5 mm mesh a mode I crack is initiated at the centre of the specimen, in accordance with test results, see Figure 3-9. As the mesh is refined the point of crack initiation is moved to the loading zone, see Figure 3-10. Arrows in the figures indicates the points of crack initiation.

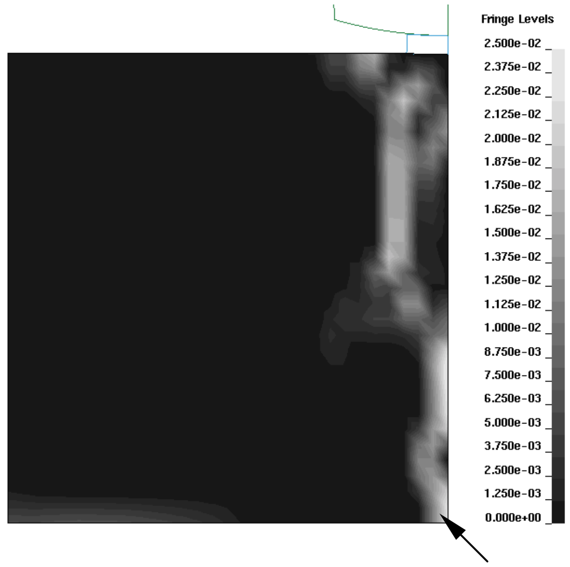

Figure 3-9 Fracture for the 2.5 mm mesh at 0.20 mm displacement. Representation by a scalar valued damage parameter.

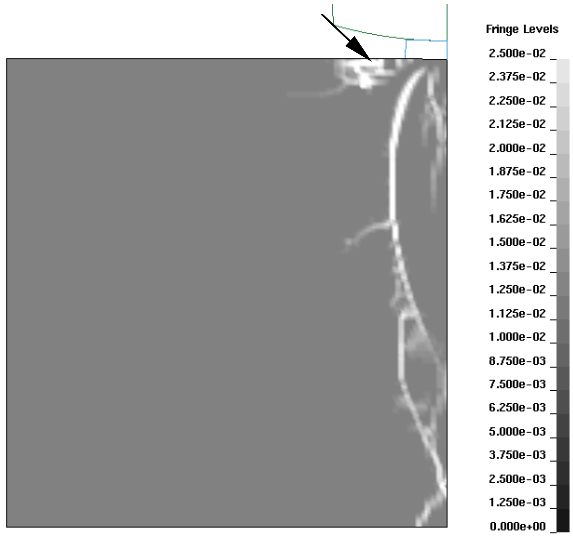

Figure 3-10 Fracture for the 0.5 mm mesh at 0.16 mm displacement. Representation by a scalar valued damage parameter.

3.2 Direct tension test with non-local theory

The splitting test only works with brittle materials that have pressure dependent strength. The non-local treatment is not available for any appropriate model in the current version of the software. To investigate the possibility of using a non-local theory when dealing with singularities the elastic-plastic model described in Section 2.2 was used in a direct tension test. A 100x50xh mm plate in plane stress was set up with a 2x2 mm notch introducing a singularity (see Figure 3-11). Computations were carried out with both local and non-local theory and the resulting plastic strain fields are shown in Figure 3-12 and Figure 3-13.

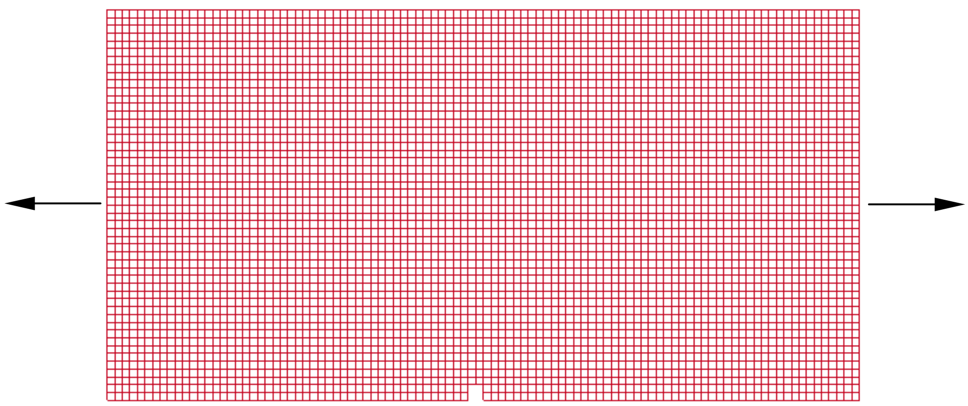

Figure 3-11 Notched geometry for the direct tension test. (h=1 mm)

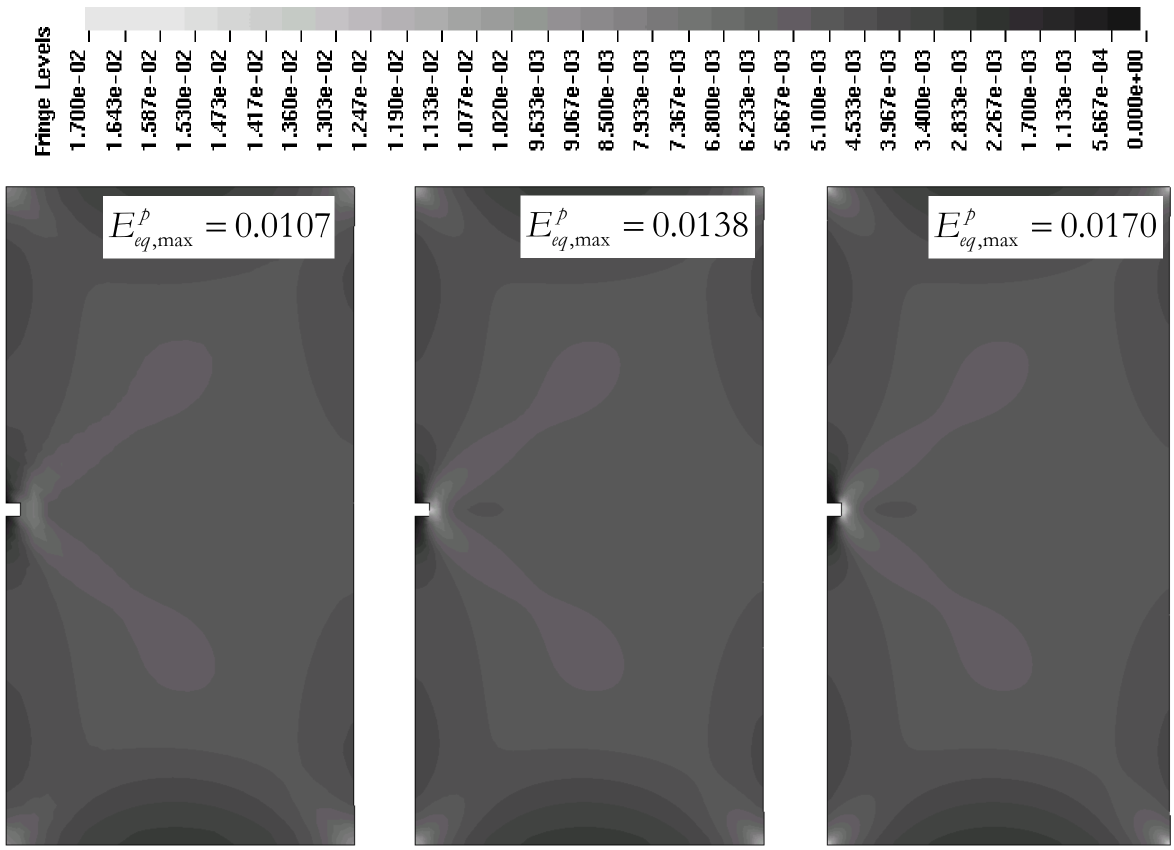

Figure 3-12 Local plastic strain fields (h=2.0, 1.0 and 0.5 mm).

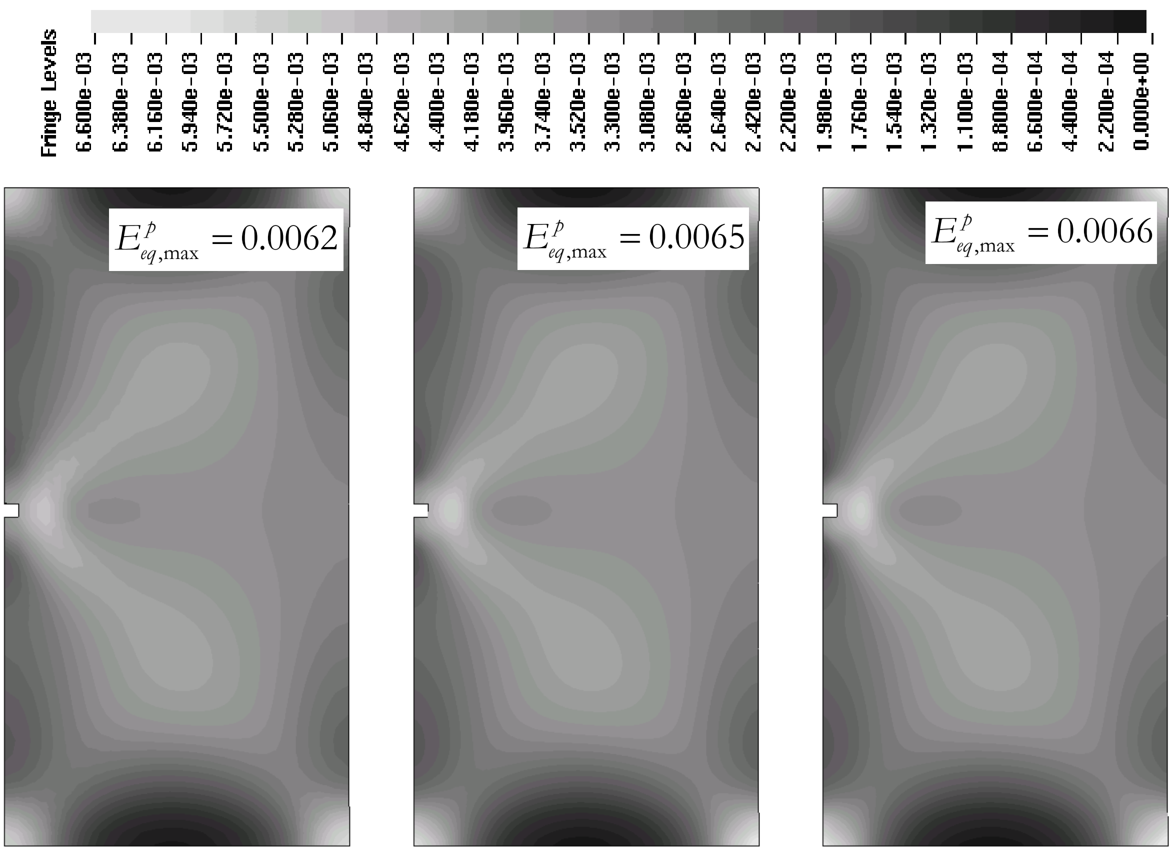

Figure 3-13 Non-local (L=5 mm) plastic strain fields (h=2.0, 1.0 and 0.5 mm).

With the local theory the maximum plastic strain in the finest mesh is 1.6 times the plastic strain in the 2.0 mm-mesh, whereas with the non-local theory the same comparison gives a factor 1.06. The global load-displacement relations are the same for all models as can be seen in Figure 3-14. The CPU-cost is shown graphically in Figure 3-15 for different levels of spatial discretization and non-local neighbourhood radius.

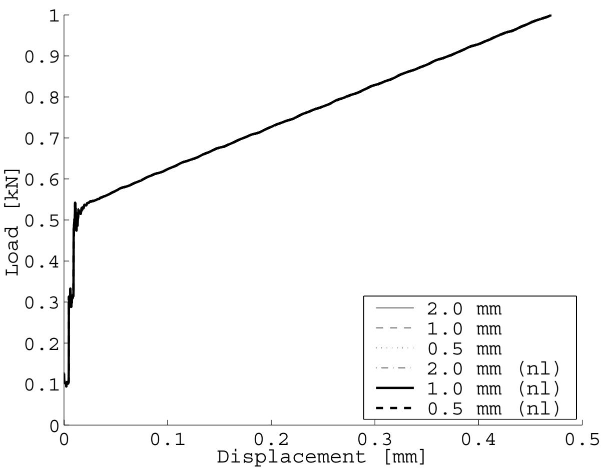

Figure 3-14 Global load-displacement relation for local and non-local theory with different finite element sizes.

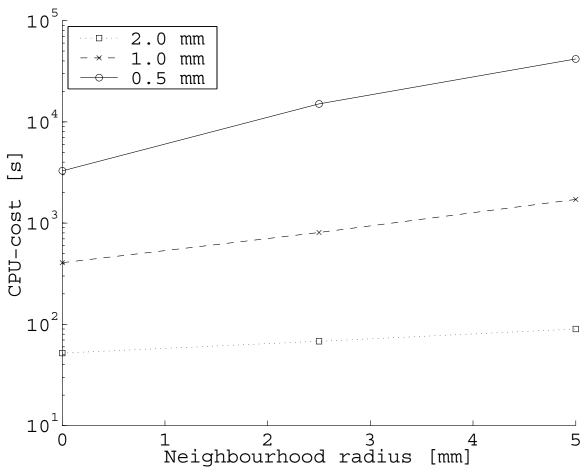

Figure 3-15 CPU-cost versus neighbourhood radius with different finite element sizes.

4 Discussion

Splitting test and the K&C concrete material model

The change of the fracture behaviour in the splitting test as the mesh is refined, is due to the occurrence of a singularity in the loading zone. At this singularity the solution converges towards immediate failure as the mesh density is increased. This is not in accordance with observations of experimental results. The overall experience from this material model gives that it will not be used in future work at FOI.

Non-local deformation

The use of a non-local theory results in a converging solution even though strain singularities are present. However, how large should the domain of influence, the element neighbourhood, be chosen? The neighbourhood corresponds to a statistical representative volume, i.e. the smallest volume for which the statistics do not change. In Bazant and Planas [8] it is suggested that tests of geometrically similar notched specimens with different sizes should be used. Iterative computations are then used to determine the size of the representative volume.

A discussion on mechanical constitutive equations for concrete

The following notes apply to the mechanical modelling of concrete materials subjected to monotonically increasing loads at high rates.

Elastic domain: It is sufficient to use isotropic hypoelasticity with the additative split of the rate-of-deformation tensor. The anisotropic elastic domain should be convex and defined in strain space in order to have a stable material description according to Lubliner [12]. In addition, from a theoretical point of view a closed elastic domain is more appealing than an open deviatoric domain combined with a separate pressure-compaction curve. Careful modelling of the elastic domain at low pressures is very important to correctly model spalling and to reproduce standard material characterization loading paths.

Inelastic domain: Plasticity is the theory of time-independent inelastic deformations, cf. Hill [13]. Strain-rate scaled plasticity, used in many material models, is thus a contradiction and can lead to numerical oscillations. Instead, a viscoplastic theory with a non-associated flow rule coupled to isotropic damage should be used, cf. Lemaitre and Chaboche [14]. Available experimental response curves can be used when defining relations governing inelastic deformations, both volumetric and deviatoric.

Implementation: For air blast loading applications, with relatively small deformations, a material description of the motion of the structure is the best approach. A material description of motion is computationally efficient and accurate at moderate strain levels. A target penetrated by a projectile should be described in a spatial reference frame so that the need for numerical erosion is eliminated. This calls for an implementation that allows both material (Lagrangian) and spatial (Eulerian) descriptions of motion.

A non-local theory such as the one used in this report should be used in the presence of singularities, keeping in mind that this calls for further size effect testing.

For the applications at hand solid elements are sufficient. However, the implementation should allow for full integration of elements near the impact zone.

Model input: Obtaining model parameters for the full range of loading magnitudes and loading rates in defence applications is not yet possible. However, registrations from high explosive planar wave set-ups enable the extraction of material data for uniaxial compaction at high strain rates and pressures. This method will be employed at the Swedish Defence Research Agency for different materials.

Fitting of material model parameters is possible by comparing simulation results to real projectile velocity history data. The velocity history through the target can be accurately registered with a Doppler radar or with accelerometers mounted inside the projectile.

Bibliography

[1] C. Ljungkrantz, G. Möller, and N. Peterson, eds. *Betonghandbok, Material.* 2 ed. 1994, AB Svensk byggtjänst och Cementa AB: Stockholm. 1127 p.

[2] P.H. Feenstra and R.D. Borst, A composite plasticity model for concrete. *International Journal of Solids and Structures* **33**, 1996, pp. 707-730

[3] Y. Sawamoto, et al., Analytical studies on local damage to reinforced concrete structures under impact loading by discrete element method. *Nuclear Engineering and Design* **179**, 1998, pp. 157-177

[4] C. Comi, A non-local model with tension and compression damage mechanisms. *European Journal of Mechanics - A/Solids* **20**, 2001, pp. 1-22

[5] *Betongprovning - Hårdnad betong - Spräckållfasthet.* SIS - Standardiseringskommisionen i Sverige, SS 13 72 13, Stockholm 1978

[6] W. Noll, A mathematical theory of the mechanical behaviour of continuous media. *Arch. Rational Mech. Anal.* **2**, 1958/1959, pp. 197-226

[7] A.C. Eringen, A unified theory of thermomechanical materials. *International Journal of Engineering Science* 1966, pp. 179-202

[8] Z.P. Bazant and J. Planas *Fracture and size effect in concrete and other quasibrittle materials*. CRC Press, Boca Raton 1997

[9] L.J. Malvar, et al., A plasticity concrete material model for dyna3d. *International Journal of Impact Engineering* **19**, 1997, pp. 847-873

[10] M. Unosson *Modelling of concrete material behaviour with application to reinforced concrete beams subjected to impact*. Swedish Defence Research Agency, FOI-R--0167--SE, Stockholm 2001

[11] M. Unosson, Numerical simulations of the response of reinforced concrete beams subjected to heavy drop tests, *Proceedings of the 4th International Symposium on Impact Engineering (ISIE/4)*. (2001), pp. 613-618

[12] J. Lubliner *Plasticity theory*. Macmillan, New York 1990

[13] R. Hill *The mathematical theory of plasticity*. Oxford university press, Oxford 1950

[14] J. Lemaitre and J.-L. Chaboche *Mechanics of solid materials*. Cambridge university press, Cambridge 1990

Issuing organization FOI – Swedish Defence Research Agency Weapons and Protection SE-147 25 Tumba	**Report number, ISRN** FOI-R--0262--SE	**Report type** Technical report
	Research area code 5. Combat	
	Month year March 2002	**Project no.** I234
	Customers code 5. Contracted Research	
	Sub area code 53 Protection and Fortification Techniques	
Author/s (editor/s) Mattias Unosson Lars Olovsson	**Project manager**	
	Approved by	
	Sponsoring agency	
	Scientifically and technically responsible	

Report title

Finite element analysis of the splitting test.

Abstract (not more than 200 words)

This report presents the behaviour of a concrete material model in a splitting test and a simplified non-local theory applied in a tensile test. The splitting test model exhibits mesh dependency due to a singularity. In the tensile test the non-local theory is shown to give a convergent solution. The report is concluded with thoughts on how to better model concrete material.

Keywords

concrete material, singularity, non-local theory

Further bibliographic information	**Language** English
ISSN 1650-1942	**Pages** 24 p.
	Price acc. to pricelist
	Security classification Unclassified

Utgivare	Rapportnummer, ISRN	Klassificering
Totalförsvarets Forskningsinstitut - FOI Vapen och skydd 147 25 Tumba	FOI-R--0262--SE	Teknisk rapport
	Forskningsområde 5. Bekämpning	
	Månad, år Mars 2002	**Projektnummer** I234
	Verksamhetsgren 5. Uppdragsfinansierad verksamhet	
	Delområde 53 Skydd och anläggningsteknik	
Författare/redaktör Mattias Unosson Lars Olovsson	**Projektledare**	
	Godkänd av	
	Uppdragsgivare/kundbeteckning	
	Tekniskt och/eller vetenskapligt ansvarig	
Rapportens titel (i översättning) Finit elementanalys av spräckprovet.		
Sammanfattning (högst 200 ord)		
Nyckelord betongmaterial, singularitet, icke-lokal teori		
Övriga bibliografiska uppgifter	**Språk** Engelska	
ISSN 1650-1942	**Antal sidor:** 24 s.	
Distribution enligt missiv	**Pris: Enligt prislista** **Sekretess** Öppen	

Institution, Avdelning
Department, Division

Div. of Solid Mechanics
Dept. of Mechanical Engineering
Linköping Institute of Technology
SE-581 83 LINKÖPING

Datum
Date
2002-04-23

Språk
Language

☐ Svenska/Swedish
☒ Engelska/English

☐ _______________

Rapporttyp
Report category

☒ Licentiatavhandling
☐ Examensarbete
☐ AB-uppsats
☐ C-uppsats
☐ D-uppsats
☐ Övrig rapport

☐ _______________

URL för elektronisk version

ISBN **91-7373-301-6**

ISRN

ISSN **0280-7971**

Serietitel och serienummer
Title of series, numbering

LIU-TEK-LIC-2002:09

Titel
Title

Constitutive equations for concrete materials subjected to high rate of loading

Författare
Author

Mattias Unosson

Sammanfattning
Abstract

Continuum mechanics is used to model the mechanical behaviour of concrete structures subjected to high rates of loading in defence applications. Large deformation theory is used and an isotropic elastic-plastic constitutive equation with isotropic hardening, damage and strain rate dependent loading surface. The hydrostatic pressure is governed by an equation of state. Numerical analysis is performed using the finite element method and the central difference method for the time integration.

Projectile penetration is studied and it is concluded that it is not suitable to use material description of the motion of both the target and the projectile together with an erosion criterion. Instead, the material description should be used only for the projectile and the spatial description for the target. In this way the need for an erosion criterion is eliminated. Also, in the constitutive model used it is necessary to introduce a scaling of the softening phase in relation to the finite element size, in order to avoid strain localization.

Drop weight testing of reinforced concrete beams are analysed, where a regularisation is introduced that renders mesh objectivity regarding fracture energy release. The resulting model can accurately reproduce results from material testing but the regularisation is not sufficient to avoid strain localization when applied to an impact loaded structure. It is finally proposed that a non-local measure of deformation could be a solution to attain convergence.

The third study presents the behaviour of a concrete constitutive model in a splitting test and a simplified non-local theory applied in a tensile test. The splitting test model exhibits mesh dependency due to a singularity. In the tensile test the non-local theory is shown to give a convergent solution. The report is concluded with a discussion on how to better model concrete materials.

Nyckelord
Keyword

impact loading, finite element analysis, material model, non-local deformation, concrete